The University Of Sheffield.

Flow Characterisation of Flames in an Acoustically Excited Chamber

A thesis submitted to the University of Sheffield for the degree of Doctor Philosophy in the Faculty of Engineering

July 2012

Li-Wei Chen

Department of Mechanical Engineering

Contents

Declaration

No portion of the work referred to in this dissertation has been submitted in support of an application for another degree or qualification of this or any other university or other institute of learning.

Copyright

Dedication

Dedicated To My Lovely Parents and Wife

Acknowledgements

I would like to express my deepest gratitude to my supervisor, Prof. Yang Zhang for giving me the opportunity to conduct this research in the Combustion and Flow Diagnostics Research Group. I am also thankful for his valuable guidance and support during PhD research and more recently for his advice and patience during the writing up period.

I would like to thank Prof. Artur J. Jaworski and Dr. Robert Woolley for their further advices and comments for the thesis. Also, I would like to thank my colleagues at the Combustion and Flow Diagnostics Lab. My sincere thanks go to Dr. Hua-Wei Huang, Dr. Qian Wang, Miss Chloe McDaid, Mr. Hussain Saeed and Mr. Jason Yang for their support, advice and assistance during my PhD study.

I would like also to give thanks to all the friends in Sheffield and Manchester who made my life enjoyable and delightful: Dr. Hui-Chi Chen, Mr. Chien-Hsing Wu, Dr. Shenghui Lei, Mr. JieYan Ma, Dr. Miss Jizhao Li, Mr. Qingfeng Xia, Mr. Leichao Yang, Miss Shou-Hui Chung, Miss Meng-Ting Chang, Miss Fu-Yi Lin, Mr. Keith Chen, Miss Fen-Ping Chien and Dr. Xiaoan Mao.

I would like to offer the deepest thanks to my family and parents-in-law for their endless support and encouragement throughout the period of my study.

Abstract

Flame-acoustic wave interactions have been studied widely in the combustion community; however the whole physicochemical mechanism is still not clear. The present research aims to further investigate the unfinished areas and focus on the acoustic excitation effect on flow and flame characteristics. An experimental approach has been adopted, and the results have been analysed and discussed. PIV diagnostic system and high speed schlieren visualisation system have been applied and built together with a signal synchronisation system which enables the phase-locked observation. The acoustic field and the interactions between acoustic waves and flames in an acoustically excited tube were studied in detail.

The acoustic wave induced by external excitation and its effect on both cold jet fuel flow and jet flames have been investigated. Results indicate that the flame behaviour is affected mostly by the variation of the excitation frequency. The infrasound (Frequency < 20 Hz) was observed to have less influence on air motion. The natural flame flicker was suppressed by the forcing infrasound because of the excitation effect on the fuel jet. In the case of harmonic frequencies at which a standing wave is formed, the ambient air and flame were less affected by the excitation in the velocity node area. In contrast, the cold fuel jet, flame and ambient air experienced large velocity variations in the anti-node area. At non-resonant frequencies, which are between the 1^{st} and 2^{nd} harmonic frequencies (65 Hz to 220 Hz), the flame pattern and luminosity were very different in each excitation case.

The frequency analysis of flames has shown that flame/acoustic coupling behaviour results in a complex nonlinear coupling effect. The excitation frequency may be coupled with the sub-harmonic frequencies and the flame flickering frequency. These frequencies were then found to couple with each other and create complex nonlinear frequency couplings. It can be seen that the surrounding air, cold jet fuel flow and flames are strongly affected by the excitation frequencies, phase angles and the nozzle location relative to the tube, and the coupling effect creates complex flame dynamics.

List of Figures

List of Tables

Nomenclature

Symbols	Meaning
A	Flame Surface Area
Al_2O_3	Aluminium Oxide
C	Speed of Sound
C_d	Drag Coefficient
C_p	Isobaric Specific Heat
CH_4	Methane
C_3H_8	Propane
CO	Carbon Monoxide
CO_2	Carbon Dioxide
d_p	Diameter of the Particle
d	Size of Droplets
F_D	Drag Force
f	Frequency of Acoustic Wave
f (Chapter 7)	Actual Fuel/Air Mass Ratio
f_e	Acoustic Excitation Frequency
f_f	Dominant Flame Flicker Frequency
f_s (Chapter 7)	Stoichiometric Fuel/Air Mass Ratio
g	Gravitational Acceleration
H	Width of the Tube

H_2	Hydrogen
H_2O	Water
h_f	The Calorific Value of Fuel
i	Index Number
K	Wave Number
K (Chapter 4)	Fluid Thermal Conductivity
k	Arbitrary Parameter
L	Length of Tube
m (Chapter 3)	Molecular Mass
m (Chapter 4)	Moving Mass of Loudspeaker
N	Sample Number of PIV Images
NO_x	Nitrogen
n	Refractive Index
n	Position of the Integer for the nth Harmonic
p	Pressure
p'	Pressure Fluctuations
q	Heat-Release Rate
q'	Heat Release Rate Fluctuations
$\dot{Q}$	Flow Rate
R	Rayleigh Index
R (Chapter 4)	Electrical Resistance
r	Radius of Particle
Re	Reynolds Number

S	Loudspeaker Membrane Cross-Section Area
S_u	Burning Velocity
s	Stiffness of Loudspeaker
T	Temperature
T_p	Particle Response Time
TiO_2	Titanium Dioxide
t	Time
U	Velocity of Cold Gas Flow
u_T	Particle Velocity
u_{max}	Maximum Velocity
V (Chapter 2)	Chamber Volume
V (Chapter 3, 4)	Output Voltage
V_s	Settling Velocity of Particles
v, u	Flow Velocity
X, Y, Z	Refer to X, Y and Z axes
X_e, X_f, Y_f	Arbitrary Amplitudes of Signals
$x_e(t), x_f(t), y_f(\mathrm{t})$	Functions of Signals
Z_{ac}	Acoustic Impedance
Z_{mec}	Mechanical Impedance

Greek Symbols	**Meaning**
τ_c	Convective Delay
τ_v	Vaporization Time-Delay

∅	Fuel Equivalence Ratio
γ	Ratio of Specific Heat
δ	Viscous or Thermal Penetration Depth
θ	Angle
κ	Thermal Conductivity
λ	Wavelength
μ	Dynamic Viscosity of the Fluid
ν	Kinetic Viscosity of Fluid
ρ_0	Ambient Density
ρ_f	Density of the Fluid
ρ_p	Mass Density of the Tracer Particles
τ	Cycle Period
u	Velocity
u'	Velocity Fluctuations
ω	Angular Frequency

Abbreviations	**Meaning**
2D	Two-Dimension
CCD	Charge-Coupled Device
CMOS	Complementary Metal–Oxide–Semiconductor
dB	Decibel
DAQ Card	Data Acquisition Card
D_r	Drive Ratio

FFT	Fast Fourier Transforms
fps	Frame per Second
LDA	Laser Doppler Anemometry
LFCPIV	Local-Field Correlation Particle Image Velocimetry
PIV	Particle Image Velocimetry
PMT	Photomultiplier-Tube
SPL	Sound Pressure Level
WIDIM	Window Displacement Iterative Multi-grid Interrogation Method

Chapter 1

Introduction

1.1 Motivation

The harnessing of fire was one of the greatest achievements of human beings and it played an important role in human evolution. For centuries, fire has been widely used in people's daily lives, for example cooking, lighting, heating and metal forming for basic needs. The methods to use fire progressed from open fires to fire places, stoves, furnaces and boilers. After the industrial revolution of Britain in the 18^{th} and 19^{th} centuries, with the advancement of technology, combustion phenomena have allowed man to develop many kinds of mechanical devices. In the 20^{th} century, fires have been applied to power generation, transportation and even space propulsion. The explosion of population in the past few decades has further led to extensive use of fire, which in turn causes damage to the global environment [1]. According to the statistic data from International Energy Agency [2], the primary source of air pollution are the emissions from all kinds of combustion systems. Harmful carbon dioxide (CO_2) and nitrogen oxides (NO_x) are produced

through the burning of fossil fuels, and are proved to be the causes of global warming and climate change. To reduce such damage to the environment, most developed countries have tightened the regulations on emission, which also enforces the studies on clean use of fuels [2, 3]. Based on these studies, highly efficient turbulent and lean premixed combustion techniques have been invented and widely accepted in the past few decades. These types of combustion exhibit a wide range of dynamics and induce large amplitude pressure pulsations and oscillations called thermoacoustic instabilities. These instabilities may reduce the system operating efficiency, induce structure vibrations and enhance the combustion noise. In extreme cases, oscillations are regarded as the possible cause of combustor structure failure [4] as shown in Fig. 1.1; the buckled and cracked combustor was due to the thermoacoustic instability [5, 6]. In order to avoid the occurrence of this undesirable phenomenon, combustion has to be restricted within certain operating ranges.

Numerous experimental and numerical studies [7-12] relating to the prediction of the thermoacoustic instabilities in the combustor have been investigated, but the whole physicochemical mechanism is still not fully understood. Although many studies have been carried out in the investigation of the interaction between the flame and acoustic wave, there is little PIV investigation of the flow field in Rijke type burners. Particularly, the acoustic flow field and their effects on combustion are rarely touched by the combustion community. The conventional Rijke tube cannot decouple acoustic wave from self sustained combustion instabilities. Our test rig enables the investigation of this particular aspect. In this study, a phase-

locked PIV system combined with a schlieren system is applied to study the behaviour of flame dynamics in an acoustically excited tube in order to gain physical insights into the acoustic streaming effect on flame dynamics.

Figure 1.1: The damaged combustors due to the thermoacoustic instability. [5, 6]

1.2 Research Objectives

The main objectives of this experimental investigation are listed below:

- To briefly review fundamental combustion theory and the thermoacoustic instability phenomenon to enhance the understanding of the effect of acoustic excitation on flame dynamics.

- To design and build a suitable experimental system for the laser based flow velocity diagnostic tool (PIV) and high speed schlieren system; two main instrumentation systems with the other measurement units are applied in

this experimental investigation in order to measure and examine the characteristics of flames in an acoustically excited tube.

- To develop an electronic circuit and LabVIEW vi programs to synchronise all the relative devices such as the loudspeaker, photomultiplier-tube, high speed camera and PIV system. This synchronisation enables the phase-locked measurement in variable conditions of the acoustically excited tube. Flame flow conditions at the specific excitation frequency, phase angle and intensity are also controllable.

- To understand the acoustic wave and air flow dynamics which are induced by the wide ranges of external excitation frequencies in a tube. PIV is adapted to measure the flow velocity and the motion of acoustic wave. The acoustic phase angle and the observed position relative to the tube are considered as parameters.

- To analyse the flow characterisation of flames in an acoustically excited square tube using a phase-locked PIV system, a high speed schlieren visualisation system and a chemiluminescence emission measurement system. The external excitation contains a wide range of frequencies which include infrasound, resonant frequencies and the frequencies between first and second resonant frequency. Also, the fuel type is considered in order to further understand the coupling behaviour between flame dynamics and acoustic excitation.

1.3 Outline of the Thesis

This thesis consists of eight chapters. These are organized as follows:

Chapter 1 is the introduction section which includes the research background, research objectives, the purpose and motivation of this study, and the outline of this thesis.

Chapter 2 is the literature review, which provides the background knowledge and reviews the fundamentals of combustion and the recent researches on flame/acoustic instability phenomena. The principle and the applications of main diagnostic apparatus, which are adopted to observe the flow structure in a tube, are also presented.

Chapter 3 introduces the experimental setup of this study. The main test rig and its fuel supply system are illustrated first. Then the signal control and synchronisation system are presented. Finally the Particle Image Velocimetry (PIV), the Z-type schlieren system and the other diagnostic apparatus are briefly described.

Chapter 4 demonstrates the preparation works for the experimental systems, which include the theoretical analysis of acoustic characterisation of the tube and acoustical system, the selection of seeding particles and the seeding methods, the statistical analysis of the PIV data and the signal synchronisation system. The testing results of seeding particles applied in the co-flow burner are also presented in this section.

Chapter 5 discusses the flow motion of acoustic standing wave and velocity data in the tube and also the flow characterisation of a flame inside a standing wave tube. The PIV system was incorporated with a high speed schlieren technique and chemiluminescence emission measurement apparatus to diagnose the flow velocity field and flame structure. The hydrogen flame was also adopted to investigate the acoustic standing wave effect on the different type of fuel.

Chapter 6 examines the oscillating frequency of a propane-air flame under different intensities of acoustic standing wave, especially on the nonlinear coupling of the flame dynamics and acoustic excitation.

Chapter 7 further discusses excitation frequency effect on the flame behaviour. Frequencies below 20 Hz and non-resonant excitation frequencies which are between the 1^{st} and 2^{nd} resonant frequency of the current test rig are set as the main test conditions to diagnose the flame dynamics.

Chapter 8 focuses on the conclusions and summaries of the present study. The major research contributions and recommendations of potential future work are also contained in this chapter.

Chapter 2

Literature Review

This study aims to use state-of-the-art diagnostics to examine the acoustic flow field, flame dynamics and thermoacoustic instability phenomena in an acoustically excited tube. In order to achieve this objective, the present knowledge and relative researches should first be surveyed and understood. The fundamentals of combustion, acoustic phenomena and the researches on thermoacoustic instability are reviewed in this chapter. The principles and applications of Particle Image Velocimetry (PIV), the high speed schlieren visualisation system and the chemiluminescence emission measurement system, which are applied to observe acoustic wave, flame oscillation frequency, flame structure and flow dynamics in a tube, are also presented.

2.1 Combustion Background

2.1.1 Basic Concepts of Combustion

Combustion, a common phenomenon surrounding people's daily lives, is generally explained as a process of establishing a self-sustained reaction using fuel and oxidiser. It involves the rapid conversion of chemical energy to heat and light energy. From a scientific viewpoint, combustion science is a combination of many disciplines which include chemistry, thermodynamics, heat transfer and fluid mechanics. Such complex phenomena are mainly induced by chemical reaction between oxidiser and fuel. Oxygen in air is typically the most common oxidiser and the most common fuels are hydrocarbons. Fuels are usually classified as gaseous, liquid or solid state. For that reason, chemical reactions can be classified as gas-phase reactions, liquid-phase reactions, solid-phase reactions, and heterogeneous reactions such as a gas-solid interface [3, 13]. Due to their clean combustion and easy storage, gaseous fuels were mainly used in this experimental study.

The underlying process in combustion is the chemical reaction that occurs on the exchange or rearrangement of atoms between colliding molecules [14]. Take a gaseous fuel for example, the global reaction of methane (CH_4) is shown below:

$$CH_4 + 2O_2 \rightarrow CO_2 + 2H_2O \qquad (2\text{-}1)$$

Reactant molecules on the left hand side of Eq. 2-1 are rearranged to become product molecules on the right hand side. To predict the combustion process, study

of the elementary reactions is needed. Yet, when researchers analyse practical combustion systems, it is difficult to analyse all the chemical reacting elements because of the complex components of the reactants. In the virtual reaction, all of the reactants in the air and fuel would be included in the reaction; therefore hundreds of other elements are produced. In complex systems, particularly, it is difficult to present all global reaction schemes. This also limits the accuracy of computational studies in the combustion area. Hence, experimental investigation is of importance in this research field.

2.1.2 Classification of Flames

The following paragraphs briefly introduce some basic idealised types of flames. The first two flame types are classified according to the method of gas mixture before the combustion reaction occurs. Also, identification of the fuel flow condition is a common method used to classify flames.

- **Premixed Flames**

A combustion reaction that starts by burning perfectly mixed fuel and oxidiser is known as a premixed flame. The first laboratory premixed flame burner was invented by Bunsen [15]. Figure 2.1 shows a schematic of the Bunsen burner. The gaseous fuel jet enters the burner from the fuel pipe near bottom. The fuel jet induces the entrainment of air via a primary air port on the control ring. Fuel and air flow up the tube where they mix before they reach the top of the burner. If an ignition source is introduced into the flammable mixture, the chemical reaction will then be started. The complex chemical reaction includes the instantaneous change

of fuel concentration and reaction temperature. Figure 2.2 shows the reaction structure of a premixed methane-air flame [16]. In the preheat zone, chemical reaction is generally negligible. Afterwards, the fuel is consumed to form CO and H_2 in an inner layer and the temperature rises rapidly. In the oxidation layer, CO and H_2 are oxidised to form CO_2 and H_2O.

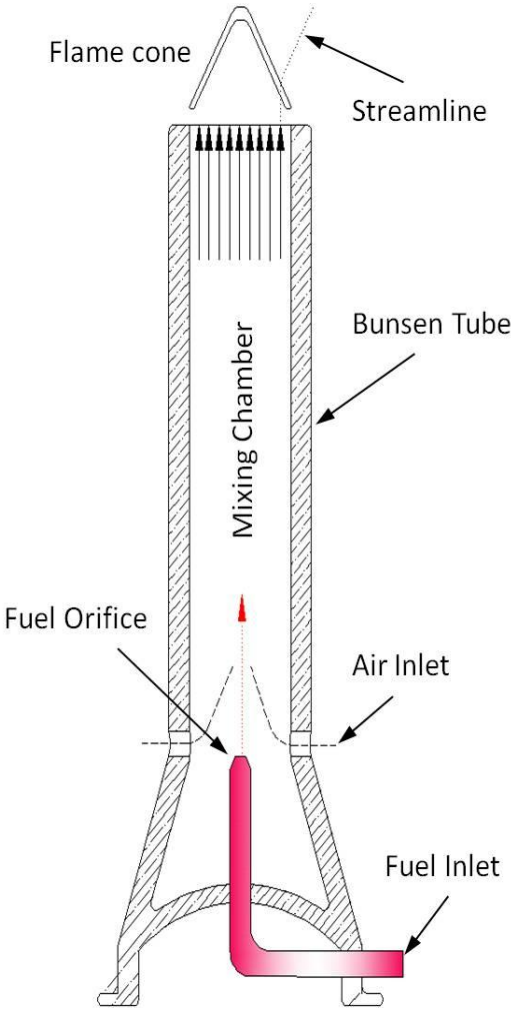

Figure 2.1: Schematic of Bunsen burner.

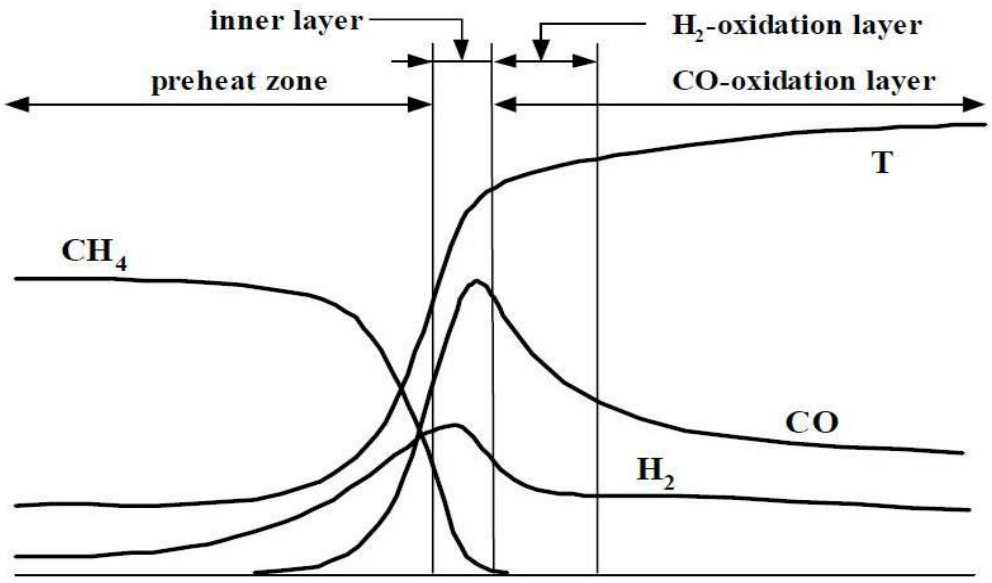

Figure 2.2: Schematic of the overall structure of premixed methane-air flames [16].

For the analysis of premixed flame, the equivalence ratio, which is to express the degree of mixing between the fuel and oxidant, is an important dimensionless parameter. The equivalence ratio (Ø) is defined as the actual fuel/air mass ratio (f) divided by the stoichiometric fuel/air mass ratio (f_s):

$$\emptyset = \frac{f}{f_s} = \frac{{}^{m_f}/_{m_0}}{\left({}^{m_f}/_{m_o}\right)_s} \tag{2-2}$$

where m is the molecular mass, and suffix $f, o\ and\ s$ stands for fuel, oxygen and stoichiometric condition respectively.

Burning premixed flames into the unburnt mixture can be characterised by the burning velocity, which is defined as the velocity of a flat flame front moves normal to its surface through the adjacent unburnt gas. If the burning velocity of a flat

flame is less than the velocity of the unburnt gases, the flame blows off. Figure 2.3 shows an example for the theoretical premixed flame front propagating at the burning velocity S_u into cold gas flow. For the ideal case, a thin plane flame front propagates into flowing gas. An important relationship to present burning velocity is observed as Eq. 2-3:

$$S_u = U \sin \theta \tag{2-3}$$

where θ is the angle between flame surface and the initial gas flow direction and U is the velocity of unburnt gas flow.

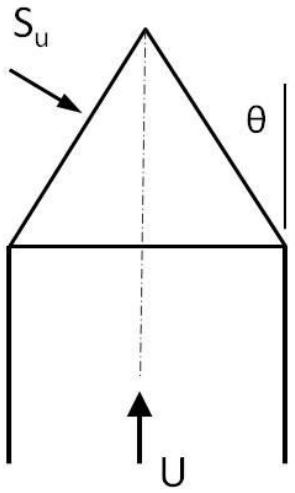

Figure 2.3: Schematic of the theoretical premixed flame front propagating at the burning velocity S_u.

- **Non-Premixed (Diffusion) Flames**

If the fuel source and oxidiser are initially separate before the combustion reaction starts, then the flame is known as a diffusion type flame. In diffusion combustion,

the chemical reaction occurs at the flame surface. The equivalence ratio can cover the range from the lowest flammability limit in the air side to the highest flammability limit in the fuel side. The combustion speed depends on the rate of diffusion. It is difficult for the chemical reaction to achieve completion due to insufficient oxidiser, hence lower combustion efficiency and higher pollutant levels occur. Figure 2.4 shows the structure of the diffusion flame. In the cross-section of the diffusion flame, Hottel and Hawthorn [17] found that the fuel concentration has a maximum on the axis and falls rapidly at the flame boundary. The oxygen concentration decreases and falls to almost zero at the flame boundary. On the contrary, the concentration of products increases near to the flame and reaches the maximum at the boundary (dotted line in Fig. 2.4).

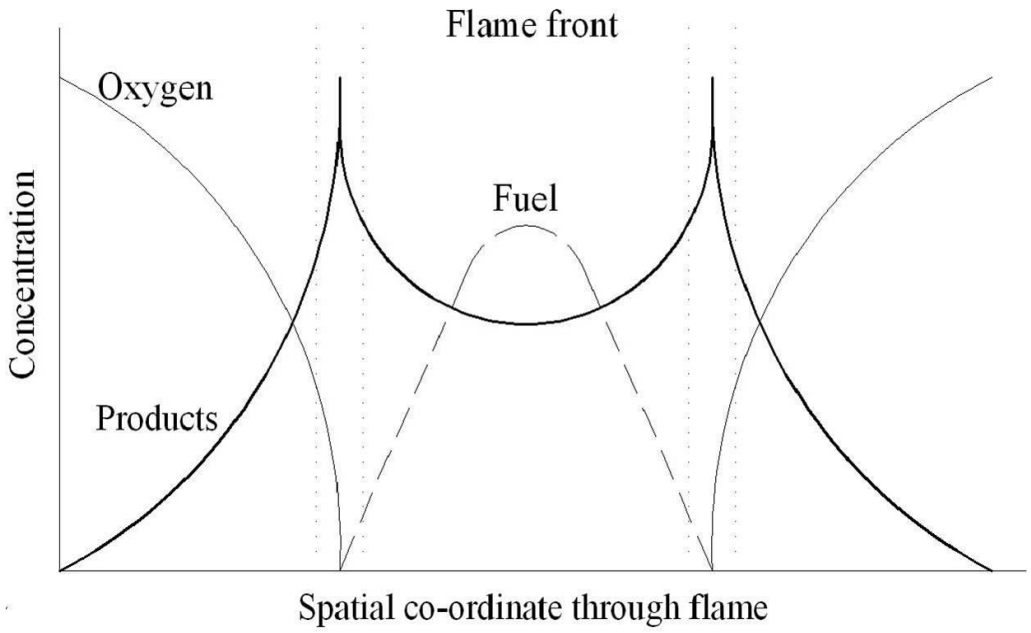

Figure 2.4: Simplified diagram of concentration profiles in a laminar diffusion flame [17].

- **Laminar and Turbulent Flames**

Flames are also classified according to their flow properties. If the fuel or mixture flow is laminar, the flame is generally laminar; on the contrary, with increasing flow velocity, the flame becomes turbulent. The gas flow of a laminar flame is uniform and the flame front is flat. A laminar flame can remain in a fixed position in space and its reaction is stable and quiet. However, in order to increase the intensity and efficiency of the combustion reaction, turbulent flames are frequently utilized. Turbulent flows enhance the mixing rate; therefore the heat release rates are much quicker than in laminar flows. The character of the flame is usually indicated by the Reynolds number ($Re = {\rho VD}/{\mu}$) of flow. As the Reynolds number is increased, laminar flows become unstable and then break down into turbulent flows.

Scholefield and Garside's [18] research demonstrated the effect of varying jet nozzle diameter and fuel flow velocity on the flame types. Figure 2.5 shows the stable flame, lifted flame and blowout regions for an ethylene (C_2H_4)-air flame. The flame propagates smoothly and steadily at lower flow velocities. At increasing of Reynolds number, the flame lifts and is then extinguished. Moreover, the soot formation also decreases due to the more complete combustion reactions. However, the turbulent flame is usually unstable and emits more noise than a laminar flame.

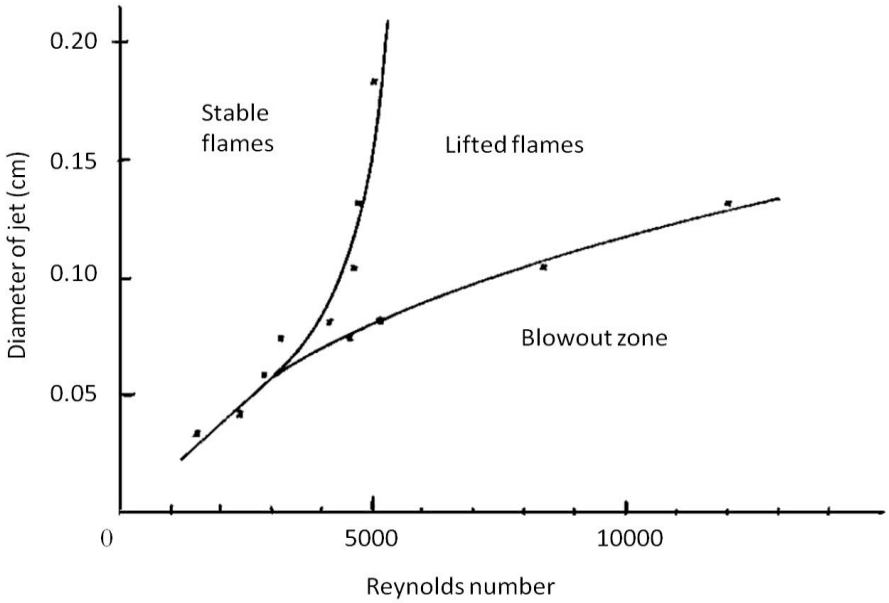

Figure 2.5: Stability ranges of diffusion flames of ethylene-air mixture [18].

2.2 Combustion Instability

Combustion instabilities are commonly observed in practical combustion systems. They have many undesirable features such as noise and vibrations. The physical and chemical mechanisms driving the instabilities are based on complex interactions. The mechanisms leading to instability are numerous and many of them are still unknown, hence there is no reliable method of predicting the occurrence and characteristics of combustion instabilities without first firing the combustor. In order to find a rational method to predict the stability characteristics for combustion system design, studies have been performed by several researchers [19-23]. However, these investigations are usually for some particular combustion design or only focus on control systems. In this study, the researcher attempts to use a simple acoustically excited tube to explore the fundamental physicochemical mechanisms of combustion instability.

2.2.1 Combustion Noise and Oscillations

Flames can be silent, but when a flame is turbulent with associated premier pulses in the flame front, the constantly changing combustion speed makes it audible. In order to obtain higher rates of combustion energy release per unit fuel volume and increase combustion efficiency, most practical combustion reactions are turbulent. However, it brings combustion noise and oscillations. Combustion noise is a random output of sound, including all frequencies with random amplitude. If the feedback loop between the reflected waves and the emitting source are phase-coherent, strong oscillations may occur. They are undesirable and may be dangerous for combustion chambers and may even cause a breakdown of the combustor. Many scientists purposefully focus on this issue in order to develop highly efficient but safe combustion systems. In earlier investigations, two types of combustion noise were defined by Strahle [24]. The first one was caused by a temporal fluctuation in the heat release of the reacting region. The second type of noise was generated by the non-uniformity of fluid regions. It mentioned that each parcel of fluid does not burn at the same mixture ratio and all streamlines were not equally heated by the combustion process. When they interact with downstream components of the device, noise will be created.

Several different physical and chemical factors can generate combustion noise and oscillations. For example, heat release rate, acoustic wave propagation, flame area, fuel/air ratio, mixing rate and natural or forced hydrodynamic instability. Time factors also affect these variations in a combustion process, including chemical

reaction time, the time taken for the flame to propagate into a new region, the time for droplet evaporation and ignition, and the time for establishment of vortices or turbulence. The most useful method to reduce these potential harmful factors is to control and suppress the magnitude of vibrations. Researches [9, 19, 20, 25, 26] show that many methods can decrease this instability in combustion chambers. Examples include modifying the geometry of combustor, improving the fuel delivery system such as supply pumps and fuel injector, or interfering with the resonant-couple to reduce its amplitude of the instability or even eliminate it. However, due to the limited understanding of the exact mechanism of the instability phenomenon, these methods can only been applied to certain types of combustor.

2.2.2 Mechanisms of Combustion Instability

The formation of combustion instability is variable and complex. The main mechanisms are briefly introduced below:

- **Rayleigh Instability**

Lord Rayleigh's criterion has frequently been used in the analysis of combustion instabilities to quantify the coupling between acoustic pressure field and unsteady heat release. This criterion states that if the local unsteady heat release is coupled with the local pressure fluctuation, then the pressure wave associated with the fluctuation will be locally amplified. The most common form of Rayleigh's criterion is the integral form shown below:

$$R = \int_0^{\tau}\int_0^{V} P'(x,t)q'(x,t)dvdt \ , \qquad (2\text{-}4)$$

where R is the Rayleigh index,

P' is the pressure fluctuation,

q' is the heat release rate fluctuation,

τ is the cycle period and

V is the chamber volume.

If the Rayleigh index (R) is positive, energy is added during a cycle and the vibration will be encouraged; otherwise, the oscillation will be suppressed. Following Rayleigh, the mechanism of combustion instability is mainly triggered by heat release oscillations, acoustic oscillations and equivalence ratio fluctuations. Furthermore, these three factors interact with one another [9, 27].

- **Hydrodynamic Instability**

Toong et al. [28] indicate that the combustion instability is not initiated through the coupling between heat and mass transfer. Vortex shedding is another possible mechanism for the self-sustained instability. The shedding of coherent vortex structures at resonant acoustic frequencies due to acoustic/combustion coupling phenomena has been observed in ducted reacting shear flow experiments and often leads to combustion instability [9]. These structures may form as a result of natural fluid mechanical instabilities such as Kelvin-Helmholtz instability or Rayleigh-Taylor instability [29].

- Kelvin-Helmholtz instability occurs when velocity shear is presented within a continuous fluid or when there is sufficient velocity difference across the interface between two fluids.
- Rayleigh-Taylor instability happens in an interface between two fluids of different densities, which occurs when the lighter fluid is pushing the heavier fluid**.**

- **Thermo-Diffusive Instability**

Thermo-diffusive instability arises when a fluid is heated. If the temperature difference across the layer is great enough, the stabilising effects of viscosity and thermal conductivity turn into instabilities. These instabilities usually depend on the properties of the reactants in the system. For example, in a liquid-fuel system, the heat transfer responsible for droplet evaporation may strongly influence this type of instability, whereas, in a gaseous system the effects of hydrodynamic strain may play a dominant role [29].

- **Buoyancy-Driven Instability**

In the practical combustion systems, the combustion burning rate, product emissions and flame stabilisation are substantial affected by the buoyancy instability. Buoyant diffusion flame instabilities are a periodic shedding of vortical flame structures. These flames exhibit natural flickering as a result of a buoyancy induced flame flow instability attributed to the interaction of strong vortical motions within the combusting regions of the flame. In diffusion flames, two different vortices have been identified: firstly, the small roll-up vortices inside the

luminous flame, and secondly, the large toroidal vortices outside the luminous flame. The small vortices are due to the Kelvin-Helmholtz instability of the jet and the toroidal vortices outside the luminous flame are due to the buoyancy-driven type of instability. This kind of flame instability induces a regular low frequency oscillation which is usually in the range of 10-20 Hz and depends on the type of fuel, the fuel nozzle size, and the exit velocities of the fuel jet. [30-32]

2.2.3 Thermoacoustic Instability

Thermoacoustic phenomena describe the coupling between heat release rate and acoustic waves. This research area includes thermoacoustic refrigeration, thermoacoustic hot air engines and thermoacoustic instabilities [33]. In this study, the researcher concentrates on thermoacoustic instabilities in a Rijke type combustion chamber.

Flame-acoustic interaction is an important phenomenon of combustion in an enclosed system. “Thermoacoustic” describes how pressure waves can be generated by a fluctuating heat released in an acoustic medium. When a pressure disturbance impinges on a flame, it generates a series of reflected and transmitted components. After the boundaries of apparatus reflect these pressure waves, the waves may collide with the flame again. These repeated interactions can substantially modify the speed of the flame. In certain situations, the flame may be extinguished; while in others sustained oscillations of considerable amplitude may be produced.

The mechanisms of thermoacoustic instability are complex due to the fact that they involve several different kinds of components such as acoustics, fluid dynamics, transport processes, chemical kinetics, flame kinematics, heat transfer, feed line dynamics of the reactants, and atomisation and vaporisation dynamics. These components can couple with each other in many different ways, as illustrated in Fig. 2.6 [11]. To accurately model such complex interaction systems with all of their couplings is nearly impossible. Experimental investigation provides another useful method to understand the physical reason of thermoacoustic instability phenomena. The following sections introduce the experimental research area in heat driven acoustic oscillations and the effects of acoustic excitation on flames.

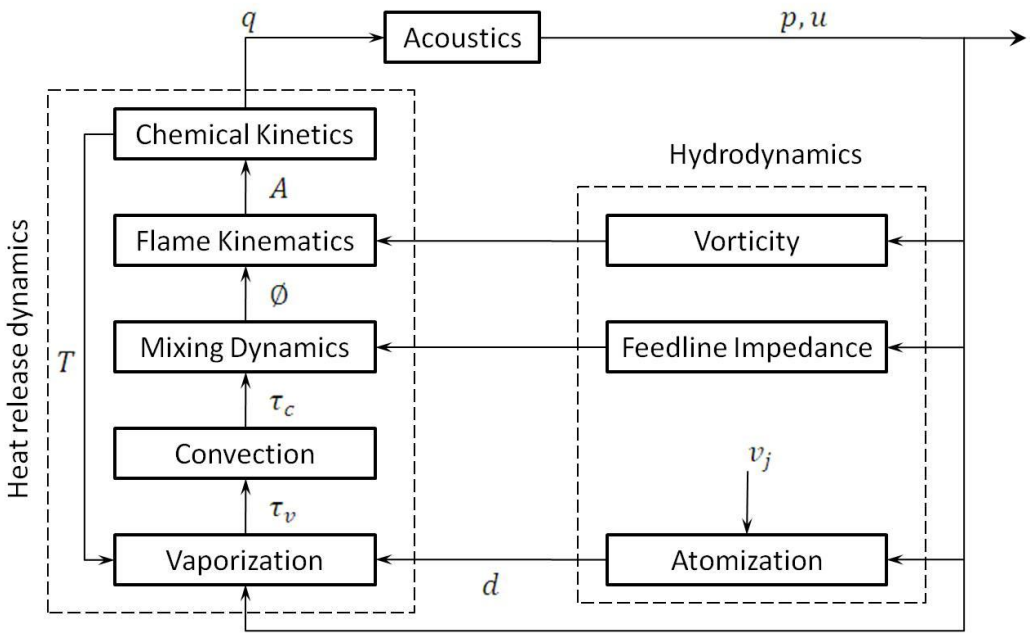

Figure 2.6: Interacting mechanisms of thermoacoustic instability [11] (p: pressure, u: velocity, q: heat-release rate, T: temperature, A: flame surface area, $\emptyset$: equivalence ratio, v_j: jet velocity, τ_v: vaporization time-delay, τ_c: convective delay, d: size of droplets).

- **Heat Driven Acoustic Oscillation**

Acoustical oscillations are frequently generated when a heat source is placed in an enclosed combustion chamber. This phenomenon was first observed by Higgins in early nineteenth century [34]. Higgins (1802) discovered singing flames when a diffusion flame jet was inserted into the tube which opens at both ends. The frequency of singing resonated with the natural frequency of the tube. Sound was produced only at certain ranges of system parameters. Afterwards, Rijke (1859) found that the strongest sound was produced by hot metal gauze located in the lower half of open-ended vertical tube. According to the observation of Rijke, in 1878, Lord Rayleigh was the first to give a completely qualitative description of the heat-driven acoustic oscillation, see Eq. 2-4. He described the balance between acoustic dissipation and acoustic excitation, and then attempted to develop analytical models for predicting thermoacoustic instabilities with their amplitudes and frequencies [27].

The Rijke type burner is a simple and useful system for investigating the combustion-driven oscillation phenomena. The oscillation in the Rijke cylindrical tube occurs when heat is added to the gauze located in the bottom quarter of an open-open vertical pipe. The hot gauze transfers heat to the surrounding air in the tube. Afterwards, the air expands, becomes less dense and starts to rise up the tube. Finally, it sets up a mean upward flow of air in the tube. When the air rises to the upper half of the tube, it becomes denser because of the contact with the cooler wall. During each cycle, the fluid elements in the lower half of the tube constantly

experience expansion, while the fluid elements in the upper part continuously undergo compression. According to the Rayleigh's criterion (Eq. 2-4), the pressure and velocity are in phase, making the Rayleigh index positive, and the oscillation grows to a self-excited state [7, 34]. However, if the upper half of tube is heated, the pressure and velocity are out of phase. This results in a negative Rayleigh index and the acoustic oscillation is dampened by the heat source. The simple schematic of the fundamental mode of the Rijke tube is shown in Fig. 2.7.

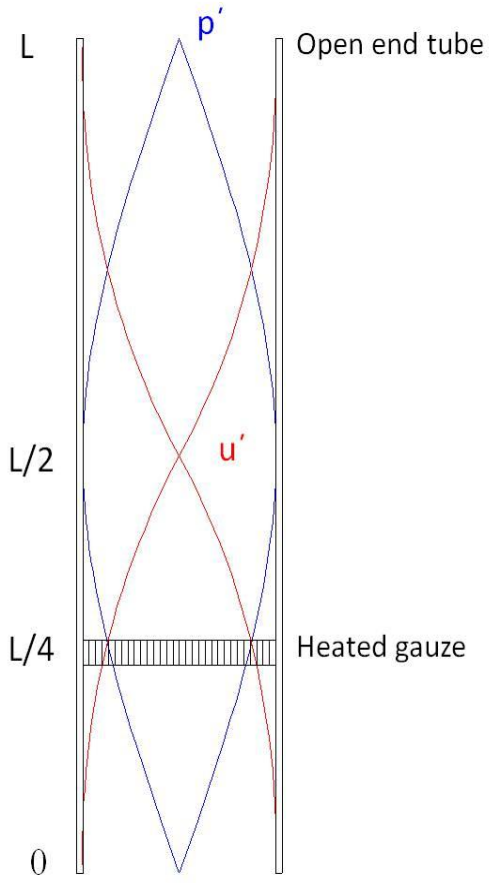

Figure 2.7: Schematic of fundamental mode of the Rijke tube

As abovementioned, Rijke tube, which is shown in Fig. 2.8(a), is frequently used in the analysis of thermoacoustic instability phenomena both experimentally and computationally [34-36]. However, most of these studies focus mainly on the self-driven oscillations rather than the use of external excitation. In this way, researchers can only measure the acoustical oscillation data which is created by the flame itself. The reflected acoustic wave, which is developed by the flame dynamics, is difficult to be observed. Also, this reflected wave effect on the flame dynamics is impossible to observe. Moreover, not much work has been reported on the acoustic wave effect a flame at different position of a combustion chamber. Papadopoulos et al. [37], Farhat et al. [38, 39] and Ehi-Uujamhan [40] have studied the external excitation effect on a flame in a cylindrical tube and interesting flame patterns were observed. The results indicated that flame patterns and properties are sensitive to the frequencies and amplitudes of acoustic excitation. The nozzle position relative to the tube also significantly affects the flame behaviour. However, the study was not able to provide full field velocity characteristics and detailed flame structure in the tube. In the present study, the PIV technique was used to measure and analyse the flow structure to understand the mechanism of thermoacoustic instability. The fuel nozzle position relative to the cylindrical tube can also be adjusted by a computer controlled traverse system, and therefore the flame flow properties at the various positions of tube under external excitation waves can be observed.

- **Effects of Acoustic Excitation on Diffusion Flame**

The characteristics of diffusion flames under acoustic excitation have been studied widely in the combustion community [41-47]. It is known that the range of acoustic frequencies, amplitudes and phase angles can affect the flame dynamics. Some acoustic forcing frequencies may induce unstable flame behaviour. In an enclosed combustion chamber, this instability can be enhanced because of the coupling between unsteady heat release rate and acoustic pressure. In certain conditions, such coupling may result in the growth of thermoacoustic instability [28]. However, in some excitation frequencies, the acoustic forcing could be utilised to control the combustion and improve the efficiency and reduce the noise and pollutants. Demare and Baillot [43] discussed the effects of acoustically forcing lifted diffusion flames at a frequency of 200 Hz. They found that the acoustic excitation produced quasi-homogeneous turbulence which provides efficient mixing and resulted in a better combustion regime. Kim et al. [44] examined the mixing behaviour of diffusion flames under an excitation frequency of 514 Hz. The result shows that a 15 % reduction of flame length and 25 % reduction in NO_x have been achieved compared to the flame without excitation. Chao et al. [48] also examined that the flame lifting and acoustic excitation at frequencies higher than the natural frequency are effective in reducing the emission index of NO_x in partially premixed flame. Saito et al. [49] observed the characterisation of diffusion flames at excitation frequencies from 30 Hz to 150 Hz. The results show that the soot emission was reduced by increasing the amplitude and decreasing the excitation frequency; in some cases, 90% soot suppression was observed. Moreover, the flame temperature in the case with acoustic excitation was higher than that without excitation. Lovett and Turn[50] studied the diffusion flame jet at the

frequency range of 2 to 1,340 Hz with varied pulse amplitudes. The results indicated that the flame was only slightly affected by high-frequency and low-amplitude external forcing. At high-amplitude, the flame is significantly affected by external excitation due to the enhanced fuel mixing rate.

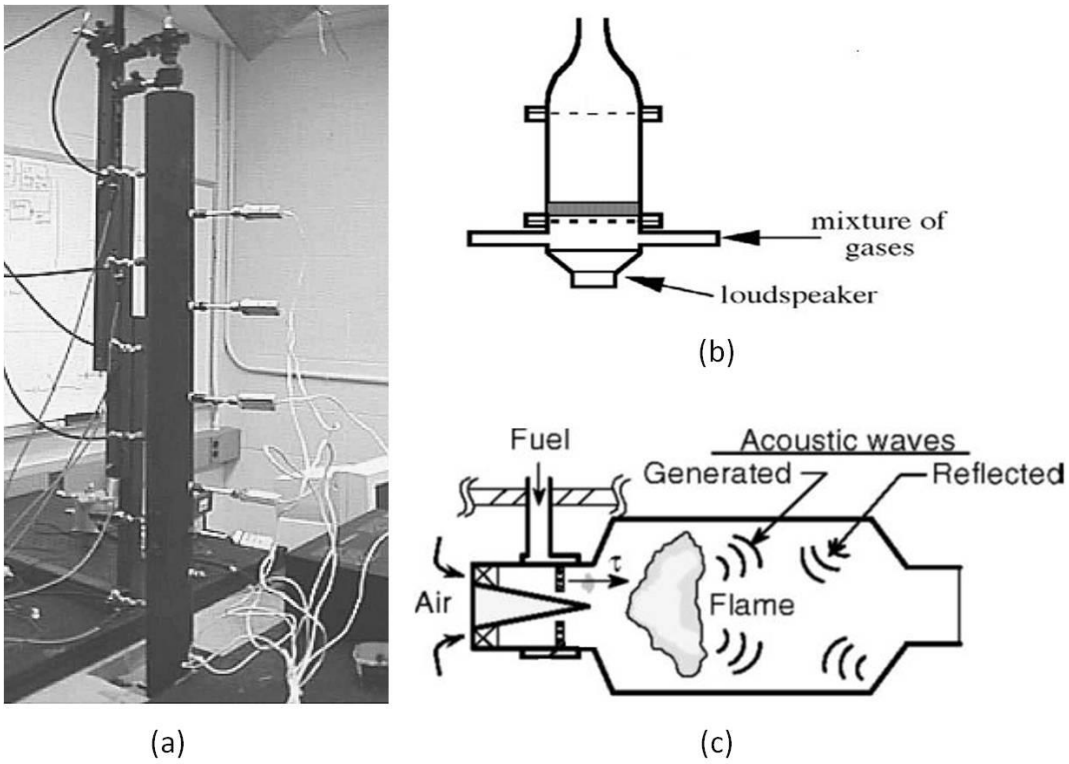

Figure 2.8: (a) Conventional Rijke tube [51], (b) general configuration for the research of flame/acoustic interaction [52] and (c) the sketch of a practical combustor [53].

As documented above, the different acoustic excitation conditions can result in various effects on flame dynamics. However, for most of the experimental configurations, the acoustic excitation is set on the location before the burner nozzle exit and the flame is usually burning in the open air. (For example, the experimental set up in Fig. 2.8(b).) In a practical combustion chamber, which is

shown in Fig. 2.8(c), is enclosed and at high pressure. Large acoustic pressure oscillations exist is because of the coupling of flame induced acoustics and the acoustic reflections on the enclosed chamber wall. Therefore, building an experimental system to observe the reflected acoustic wave effects on a flame at an enclosed combustion chamber could enhance the understanding of the flame dynamics in a practical combustor. The test rig, which is designed in the present study (see chapter 3), enables the observation of acoustic wave and reflected acoustic wave effect on the flame. Moreover, the wide range of external excitation frequencies is included to detect the influence on flame behaviour in different position of the tube.

2.2.4 Control of Thermoacoustic Instability

As mentioned in previous sections, the existence of thermoacoustic instabilities have their own mechanisms and feedback loop, coupling heat release rate and acoustic waves. The aim of the technique to control the thermoacoustic instability is to break up this feedback loop and optimise the combustor operation. Passive or active instability control systems are often designed to suppress the combustion instability and improve combustor performance. The detailed principle and control methods are introduced in the following paragraphs.

- **Passive Instability Control**

The passive instability control method has been widely used in practical combustion chambers to solve the combustion instability problem [53]. This method usually

begins by modelling and analysing a new combustion system. Then, according to the analysed data, redesigning or modifying the combustion system to avoid the potential factors that may induce combustion instability. These modifications usually include fuel supply system, flame holder and the overall dimensions of the combustion chamber. Although this procedure is useful and reliable to avoid the phenomenon of combustion instability, development of passive control combustion systems is costly and time consuming, and is specific to a particular combustor design. Moreover, the limited ranges of operating conditions may result in lower combustion efficiency and higher emissions.

- **Active Instability Control**

Active instability control techniques usually involve a complex control system which includes the detectors, the actuators and a reliable control system. The typical detectors that are commonly in use include pressure sensors (microphone), gas sensors, optical diagnostics and hot wire anemometry [20]. The control actuators include acoustic drivers, system shaking devices, secondary fuel injectors and valve controllers. The action of the actuator system depends on the response of the detectors. For example, when the pressure sensor detects a high impact of combustion instability, the acoustic driver can send an “out of phase” acoustic signal to the combustor to suppress the instability or adjust the fuel flow rate, decreasing the heat release oscillation [9, 11]. According to the type of controller, the active control system can be classified into a closed-loop, open-loop, fixed-parameter or adaptive control system. A table with block diagrams describing these

control systems is shown in Fig. 2.9. The active instability control techniques offer useful and active methods to modify the ambient conditions or operation conditions of the combustion system to suppress the instability. However, due to the difficulty in detecting the initial instability factors and the instantaneous response time, to design a reliable and accurate control system in a practical combustion system is nearly impossible, at least for the time being. Due to the abovementioned, although the instability control techniques have been studied for years to avoid the combustion instability, suppressing the instability completely is still impossible. Therefore, to understand the uncertain factors of combustion instability and its mechanisms becomes a vital issue in this research field.

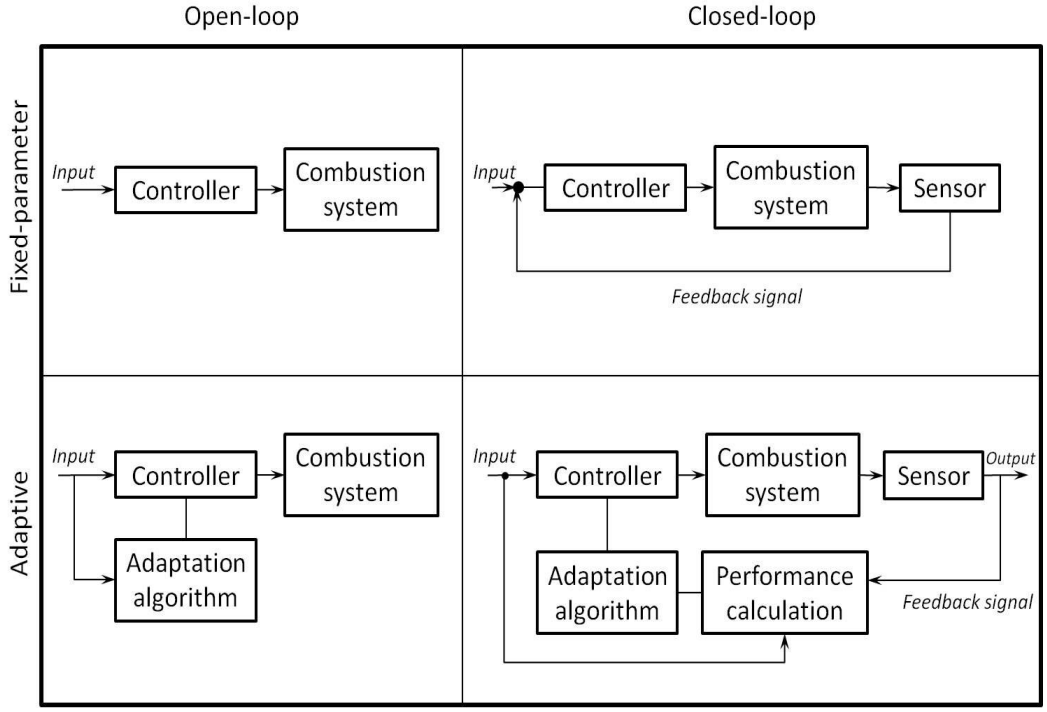

Figure 2.9: Classification of active combustion instability controller with block diagrams [9].

2.3 Acoustics

The thermoacoustic phenomenon is the coupling behaviour between heat release rate and acoustic waves; therefore, it is very important to know the motion of acoustic flow field in the tube before further analysis of the coupling behaviour with flame dynamics. The acoustic field is well known in theoretical and numerical simulation areas [54-57]. The main phenomenon of acoustics is wave propagation. Since the acoustic waves are mechanical, they need to travel via media and the waves transport energy throughout the propagating media. Acoustic waves are transmitted through gases as longitudinal waves, which are waves of alternating pressure causing local regions of compression and rarefaction. Frequency, wavelength, amplitude, intensity, velocity and wave vectors are usually used to characterise the acoustic wave. Frequency (f) is the number of repeating wave cycles per unit time and wavelength (λ) is a measure of the distance between repetitions of a wave shape feature. At a fixed wave speed, the wavelength is inversely proportional to the frequency. For instance, waves with higher frequencies have shorter wavelengths and those with lower frequencies have longer wavelengths. Amplitude is the magnitude of change with the signal oscillating variable. For example, if the acoustic waves are oscillations in atmospheric pressure, their amplitudes are proportional to the change in pressure during one oscillation. The acoustic energy reaching a particular place is defined as intensity, which can be represented as the energy per second per m^2 (W/m^2) [58].

The property of acoustics can be measured using many techniques. The decibel meter is the most common device to measure acoustic pressure level. However, the reading given by this device can only roughly estimate the level of loudness. Hot-wire anemometry can be used to measure the flow velocity of acoustic waves, but this intrusive technique can easily disturb the velocity field of acoustic waves [59]. Laser Doppler anemometry (LDA) provides another method to measure the flow velocity of acoustic waves [60, 61]. However, LDA can only provide velocity measurements at a point in the flow; it is difficult to obtain two-dimensional flow structure from this technique. Synchronised PIV techniques can be used to measure two-dimensional acoustic velocity fields with high spatial resolution. Campbell et al. [62] presented a review of PIV with its application to the measurement of sound motion. Results indicate that some experimental studies have been successfully carried out to obtain the characteristics of sound waves by using laser based diagnostics. Nabavi et al. and Siddiqui et al. [63-65] have also been successful in obtaining the two-dimensional velocity fields of standing waves using PIV. The measured velocity is found to be in excellent agreement with the theoretical values. In this study, the PIV technique will be used to measure the velocity field of acoustic waves in a tube to observe the interaction between heat release and acoustic flow fields.

2.3.1 Standing Wave in Air Columns

A standing wave remains in a constant position and it arises from two propagating waves travelling in opposite directions that eventually interfere with each other. It behaves like a wave on a string in an air column inside a tube. The periodic waves

are reflected at a boundary and the reflected waves are combined together. If the phase relationship is correct, standing waves can be formed, as shown in Fig. 2.10. The velocity node and anti-node regions remain at the same position in the tube. The standing wave frequencies and wavelengths are related to the length of the tube. The longest wavelength, which shows in the most left hand side of Fig. 2.10, is the fundamental frequency. Standing waves can also be formed in shorter wavelengths as long as multiples of half the wavelength fit the tube length (for example, the 2nd, 3rd and 4th harmonics in Fig. 2.10). The frequencies of these waves, which are multiples of the fundamental frequency, are called harmonic frequencies. These harmonic frequencies can be represented by a mathematical equation. In the case of a simple constant cross-section tube with one-end open and one-end closed, this equation can be given by Eq. 2-5.

$$f_n = \frac{c}{\lambda_n} = \frac{(2n-1)c}{4L}, \ldots \text{ where } n = 1, 2, 3, \ldots \quad (2\text{-}5)$$

where λ_n is the wavelength,

f_n is the wave frequency,

L is the length of tube,

C is the speed of sound in air and

n is the position of the integer for the nth harmonic.

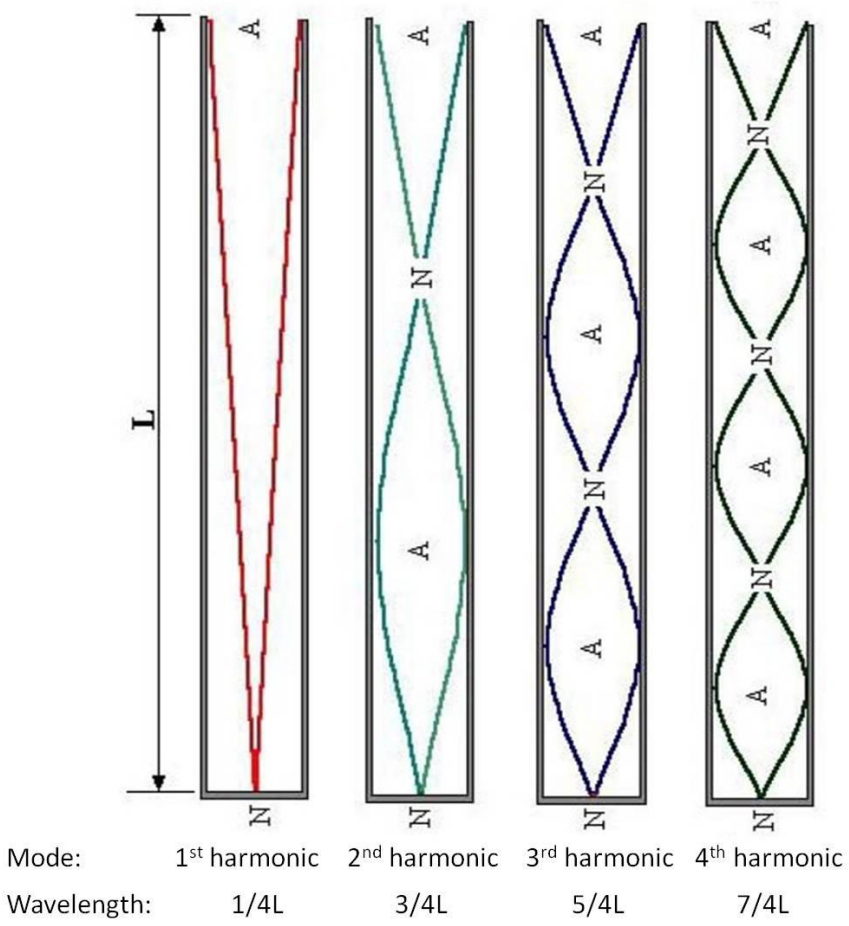

Figure 2.10: Standing wave for one-end open and one-end closed tube (N: velocity node region, A: velocity anti-node region).

In the present study, the cross-section of the tube is square and non-constant. A pyramidal structure is designed in the lower half of the tube to fit the size of loudspeaker. This acoustical system is more complex than that presented in Eq. 2-5 and Fig. 2.10. In order to fully understand the response of the acoustical system and the acoustic coupling between the loudspeaker and the tube, the detailed theoretical acoustic model and experimental measurements for the present test rig is future discussed in chapter 4.

2.4 Particle Image Velocimetry (PIV)

In earlier studies, researchers usually used hot wire anemometry or pressure probes to measure the flow velocity and direction. However, these technologies can only measure a local area of flow velocity and low intensity turbulent flows. Moreover, this intrusive technique easily disturbs the flow velocity fields. Furthermore, hot-wire anemometry contains some disadvantages such as breakable, sensitivity to temperature changes, low sensitivity to flow direction, high signal noise and inability to measure near a boundary, which limits its functions [66]. LDA, which can solve most of the disadvantages in the application of hot wire or pressure probes, is another device to diagnose the velocity field. However, LDA can only provide the velocity information at one single point in space. In order to solve these drawbacks, researchers have discovered and proved that PIV is a useful diagnostic tool to observe the flow field. In the early 20 century, Ludwig Prandtl developed the earliest PIV concept when he observed the distribution of mica particles on the surface of water in a water tunnel [67]. Unfortunately, due to the lack of advanced technologies, Prandtl could only acquire limited information of the flow properties. Later in the 20^{th} century, with the rapid development of computer and laser technologies, PIV has become a powerful technique in flow field studies. This diagnostic technique provides instantaneous information on the entire flow field from any acoustic phase angle and in three dimensions. Figure 2.11 illustrates (a) PIV raw data, (b) vector maps and streamlines and (c) velocity contours of a flickering diffusion flame.

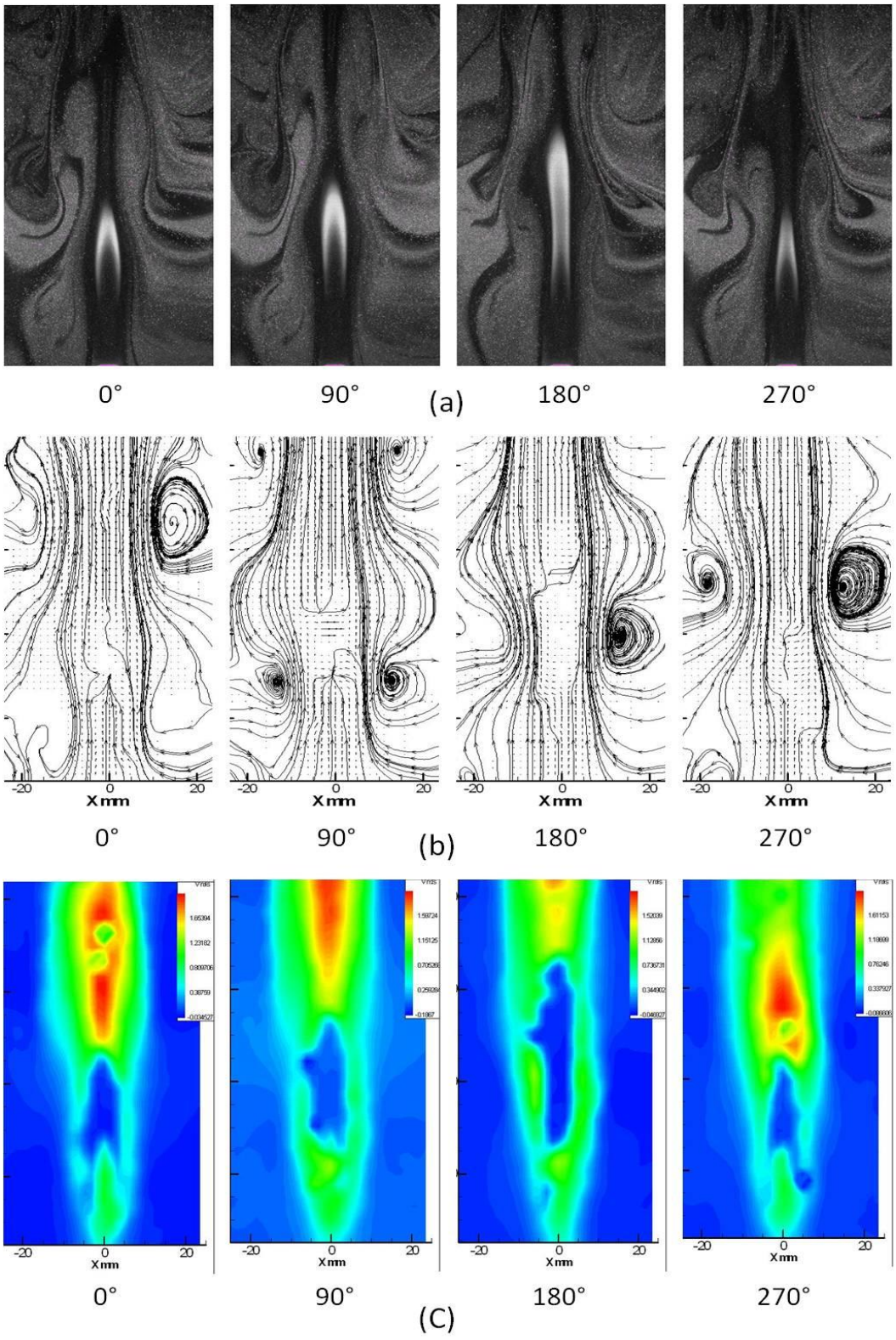

Figure 2.11: (a) PIV raw data, (b) Vector maps and streamlines, (c) Velocity contours of a flickering flame. (The central blank (blue) area near the x-axis is the region of the flame, where the seeding particles could not be traced effectively because only the surrounding air is seeded.)

In 1977, three different independent research groups (Barker and Fourney, Dudderar and Simpkins, and Grousson and Mallick [68]) demonstrated the laser speckle phenomenon to fluid flow by measuring the parabolic profile in a laminar tube flow. They were the first investigators to achieve reliable PIV measurements. Since then, PIV has been applied in numerous fluid experiments, such as aerodynamic research, jets in water, multiphase flows and in the combustion area. In addition, the commercialisation of high-resolution charge-coupled device (CCD) cameras has superseded the film in the 21st century, and also highly reliable image-processing packages have improved. The combination of these advanced techniques have evolved PIV techniques into a commercial laboratory tool [68]. Hundreds of studies and publications about PIV have been reported and reviewed by Buchhave, Dabiri and Grant [69-71].

2.4.1 Principles of Particle Image Velocimetry

Imagine that two photographs of a moving object are taken and the time between the 1st photo and the 2nd photo is measured, then the speed and moving direction of the object can be calculated. The typical layout and general idea of a PIV system are shown in Fig. 2.12 and Fig. 2.13 respectively. In practical applications, thousands of tiny particles (instead of the object) are applied. These tiny particles are assumed to follow the motions of the fluid accurately. Photos of these particles within a short time interval are taken. In order to get clear and high contrast of particle images in very short exposure time of the camera, a synchronised laser pulse is used. After the tracer particles are recorded on two separate frames, the properties of the flow field can be calculated and analysed by a data process system [67, 72].

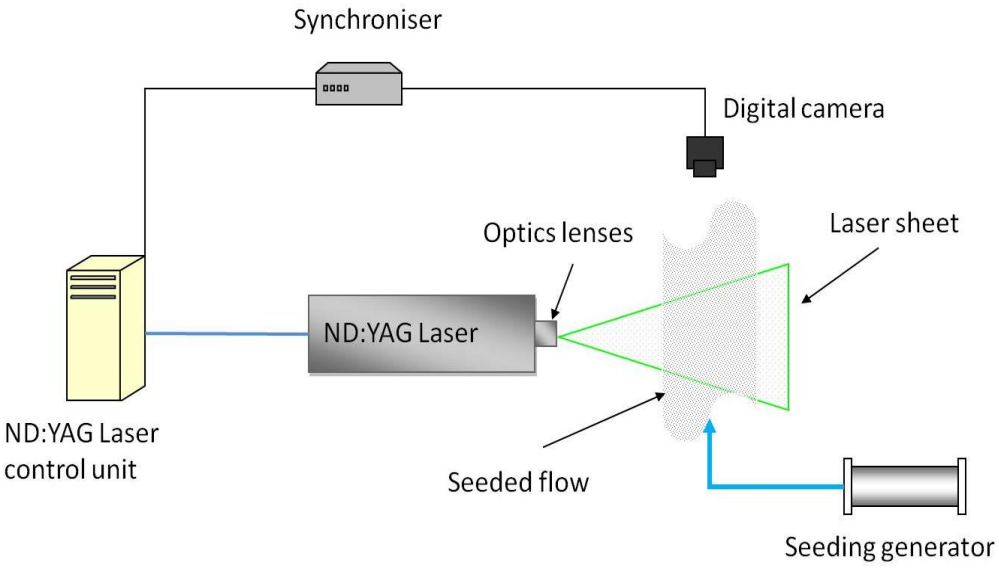

Figure 2.12: The layout of a typical PIV system.

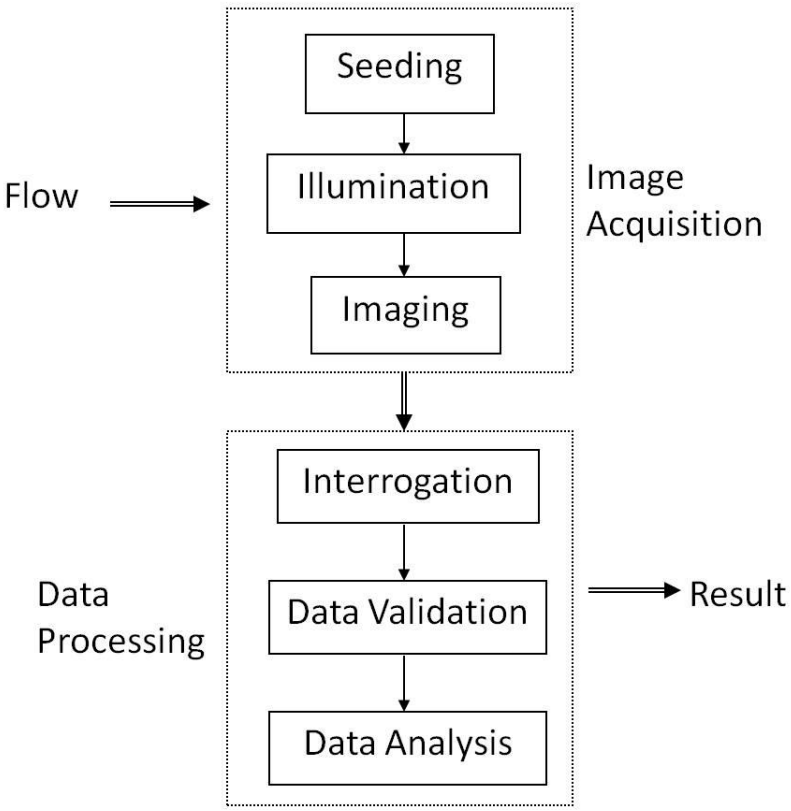

Figure 2.13: The general idea of PIV.

2.4.2 Tracer Particles

The objective of PIV is to calculate the cross-correlation between two sequence PIV raw images. The ideal imaging of a PIV system is determined by the perfect tracer particles. The perfect tracer particles should not only follow the motion of the fluid exactly, but also exhibit their light scattering behaviour. Moreover, the density and diameter of tracer particles also significantly affect the quality of the images, due to the influence of gravitational effect and drag force. Furthermore, another point to be considered is that the seeding particles cannot have any chemical reaction with the working fluid is.

If the densities of the working fluid and the seeding particles do not match, the influence of gravitational force will affect the accuracy of the PIV results. The drag force of particles is another factor that will affect the motion of seeding particles. The equations below could calculate the potential error caused by gravity and drag force. Firstly, the drag force (F_D) of the seeding particles could be calculated by the drag equation Eq. 2-6 [67, 73]:

$$F_D = {}^1\!/_2 \ \rho_p V_s^2 C_d A \tag{2-6}$$

If F_D = Fg, then the seeding particles can resist the gravitational force.

Therefore:

$$\left(\rho_p - \rho_f\right) {}^4\!/_3 \pi r^3 g = {}^1\!/_2 \rho_p V_s^2 C_d \pi r^2 \tag{2-7}$$

$$V_s = \sqrt{\frac{8rg(\rho_p - \rho_f)}{3\rho_p C_d}} \quad (2\text{-}8)$$

where F_D is the force of drag (N),

C_d is the drag coefficient (assumed as sphere shape, C_d=0.47),

V_s is the particles' settling velocity (m/s),

g is the gravitational acceleration (m/s^2),

r is the radius of particle (m),

μ is the fluid's viscosity (kg/ms),

ρ_p is the mass density of the particles (kg/m^3) and

ρ_f is the density of the fluid (kg/m^3).

Eq. 2-8 shows the minimal flow velocity required to make the seeding particles buoyant. In order to reduce the experiment error, the seeding particles should be as tiny as possible to follow the fluid motion being measured, but large enough to generate a strong scattering signal. Light scattering behaviour is another vital characteristic of seeding particles. In general, studies of light scattering from spherical particles, the intensity ratio of scattered light is a strong function both of the size parameter and the refractive index [67, 74].

The response time of the trace particles to the change in flow behaviour is another important issue in PIV study. It is difficult to find trace particles that have the same density as the working fluid, and hence knowledge of the response time of the particles is essential. The characteristic response time of trace particles can be computed by the equation below: [67, 75, 76]

$$T_p = {}^{u_T}/_{g} \tag{2-9}$$

where T_p is the particle response time,

u_T is the particle velocity and

g is the acceleration due to gravity.

If we assume that the trace particles are in a viscous fluid at a very low Reynolds number, then the particle terminal velocity (u_T) can be calculated by:

$$u_T = \frac{(\rho_p - \rho) d_p^2 g}{18\mu} \tag{2-10}$$

where g is the acceleration due to gravity,

μ is the dynamic viscosity of the fluid,

d_p is the diameter of the particle,

ρ is the density of the fluid and

ρ_p is the density of the tracer particles.

For different working fluids, the types of seeding particle will be very different. Table 2.1 shows the different particles that can be used for gas flow visualisation in PIV [67]. Gas flows can be seeded with either liquid droplets or solid particles. For liquid droplets, the atomiser should ideally produce particles with a uniform size distribution and at a high enough rate to achieve sufficient spatial resolution of the PIV in the flow field.

Solid particles, compared to liquid droplets, are more suitable for high particle concentrations. The choice of correct seeding particle and how to practically generate the particles into the flow fields are key points of PIV research. Related PIV seeding particle studies have been discussed by many scientists [74, 77-79]. In combustion research, the seeding particles have to resist the chemical reaction and the high temperature of the flames. Moreover, seeding powder cannot form agglomerates or condense in the narrow pipes of the burners. Ceramic materials such as Al_2O_3 and TiO_2 are favoured for the application of flame flow and other high-temperature flows; meanwhile, ceramic materials also offer a high refractive index, and hence high quality images can be achieved.

Table 2.1: Seeding materials for gas flows [67].

Type	**Material**	**Mean diameter in µm**
Solid	Polystyrene	0.5 - 10
	Alumina Al_2O_3	0.2 - 5
	Titania TiO_2	0.1 - 5
	Glass micro-spheres	0.2 - 3
	Glass micro-balloons	30 - 100
	Dioctylphathalate	1 – 10
	Smoke	< 1
Liquid	Different oils	0.5 - 10
	Di-ethyl-hexyl-sebacate (DEHS)	0.5 - 1.5
	Helium-filled soap bubbles	1000-3000

2.4.3 Theories of PIV Processing

Although the principles and concepts of PIV are mentioned, to trace numerous seeding particles between two images is unrealistic. Mathematical correlation processing can be used to solve this problem. Firstly, these images are divided into small subareas called “interrogation regions". Then the statistical method is applied to a group of particles to calculate the correlation between two interrogation regions. The two sequential images indicate a field of linear vectors where each vector is formed by analysing the movement of the two interrogation regions.

The concept of PIV calculation steps for image processing, analysing and post processing are shown in Fig. 2.14. Mathematically, cross-correlation methods are usually applied for analysing recorded PIV images, and then the displacements of the interrogation windows can be calculated and measured. It is an algorithm that sums the particle image that matches at all pixel displacements within the displacement range. The Fast Fourier Transforms (FFT’s) are used to calculate the cross-correlation processes. The size of the interrogation windows is determined by the accuracy, the quality and the resolution of the recorded raw images. Figure 2.14(A) shows the result of a cross-correlation map. The smaller peaks are the results of individual particle images correlating with other particle images. The highest correlation peak indicates the best match of particle images between the two interrogation regions. The mean velocity vectors are then calculated by the movement of the particles in the interrogation windows. Finally, repeating the procedure mentioned above, a 2D velocity vector map for the flow field will be generated [67, 80, 81].

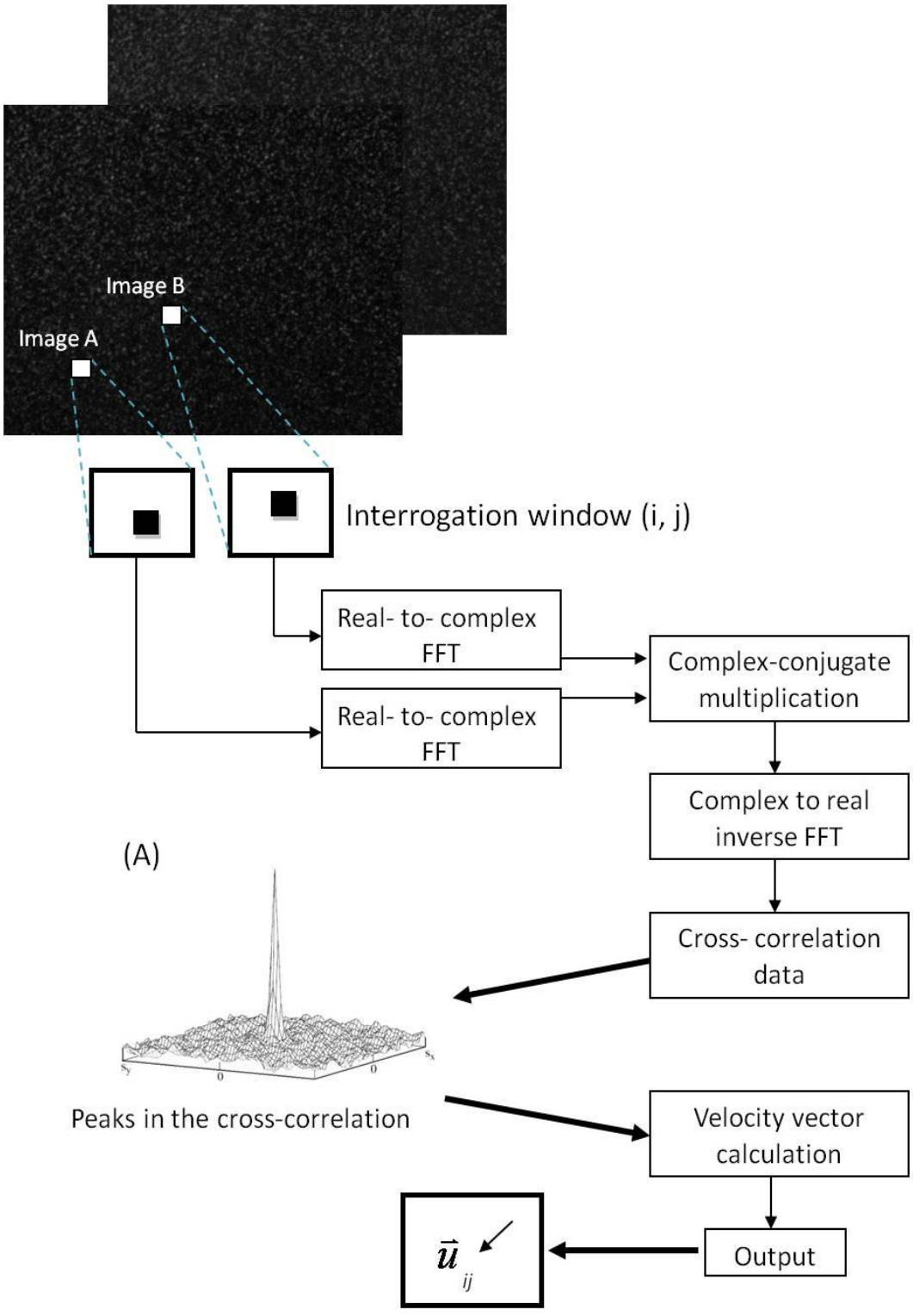

Figure 2.14: The diagram of PIV calculation steps for image processing, analysing and post processing [67, 80].

PIV algorithms, based on the tracking of an individual particle image, obtain the vector for each particle. However, several factors affect the results of the cross-correlation calculation. For example, the size of the interrogation window, the separation time between the exposures, local velocity gradients, device performance characteristics and computational errors. These factors also lead to loss of measurement precision, particularly, in non-optimal experimental conditions. Many researchers have made efforts to improve the resolution for PIV in order to avoid the resolving errors and achieve higher spatial resolution. The window displacement iterative multi-grid interrogation method (WIDIM) [82] is used to refine the window size and deformation during the iterative interrogation. This increases the accuracy and spatial resolution of the PIV, especially in poorly seeded regions. Local-field correlation Particle Image Velocimetry (LFCPIV) is another method to enhance PIV quality [83, 84]. The interrogation windows for LFCPIV are fixed in size and location. After each iteration step, the image is redefined through compensation of the particle pattern deformation caused by the velocity gradients in the flow field. It is performed using the displacement field from the previous evaluation. This method achieves a better response in large velocity gradients and poor quality of raw images.

2.4.4 PIV Application in Combustion

The flame flow structure was previously difficult to understand, because of the high radiation and temperature of the combustion reactions. PIV technology provides a useful method to tackle these problems. Many researches [31, 85-87] have applied

PIV to measure the detailed flame flow behaviour in various conditions. Otsuka and Wolanski [86] successfully used PIV to observe the detailed flow structure, flame propagation velocity and velocity distribution in the flame for different air excess factors. Yilmaz et al. [87] studied the flow field of the flickering diffusion flame. The slot burner in an enclosed box filled with Al_2O_3 or TiO_2 tracer particles was adopted in their study. Velocity vector maps and the flow stream trace of the oscillating flame were obtained using the PIV method. Unfortunately, the synchronisation between the flame flickering and the PIV laser pulses was not applied. Therefore, the flame structure is not phase resolved. Papadopoulos et al. [31] used PIV to observe the phase-locked velocity field in the center plane of an acoustically forced methane–air diffusion flame. The co-flow burner was seeded both in the methane fuel jet and co-flow air. A loudspeaker was positioned at the bottom of the burner to control the flame behavior. Averaged velocity magnitudes and vector maps near the burner were obtained. The results provided a better understanding of acoustic forcing on initial jet flow velocity. However, the external acoustic excitation was only used to control the initial fuel flow and the flame behaviour. The effect of air motion induced by the acoustic wave and its reflections on the enclosed chamber wall were not investigated in detail.

With the rapid commercialisation of PIV system in recent years, many studies have been carried out in the investigation of combustion phenomena. No matter whether the flow characterisation is in diffusion flame jet oscillations or turbulent premixed flames, the PIV technique is widely used [45, 87-89]. However, there is no report that shows the PIV used in the investigation of the flow field in the Rijke type

burners. The acoustic flow field and particular its effect on combustion behaviour is rarely touched by the combustion community. In this study, a phase-locked PIV system is applied to study the behaviour of acoustic flow field and flame dynamics in a tube.

2.5 Schlieren

The schlieren technique, which can visualise the gradient of flow density, is another useful flow visualisation method. This technique has been used for centuries to study the distribution of density gradients within a transparent media. Robert Hooke is a pioneer of the schlieren techniques [90]. In 1665, he used a convex lens and two candles to build a conventional schlieren system. After that, the schlieren technique was developed as a visualisation system by Toepler in 1864 [91]. Since then, many kinds of schlieren arrangements were developed, such as single-lens, dual-lens and Z-type 2-mirror schlieren.

The most popular schlieren arrangement, which uses two parabolic mirrors, is the Z-type schlieren system. The light source is placed on the focal point of one side of the parabolic mirror, while the knife-edge is set on the focal point of another parabolic mirror to adjust the brightness and contrast. The arrangement of a Z-type schlieren system is shown in Fig. 2.15. In the present study, the Z-type 2-mirror schlieren system was adopted to observe the flame flow field. Due to the variation of flow density gradient in the combustion reaction, the reacting region and the mixing zones of the hot gases can be observed by the schlieren photography

technique. As shown in Fig. 2.16, an example of the typical schlieren image of a diffusion flame.

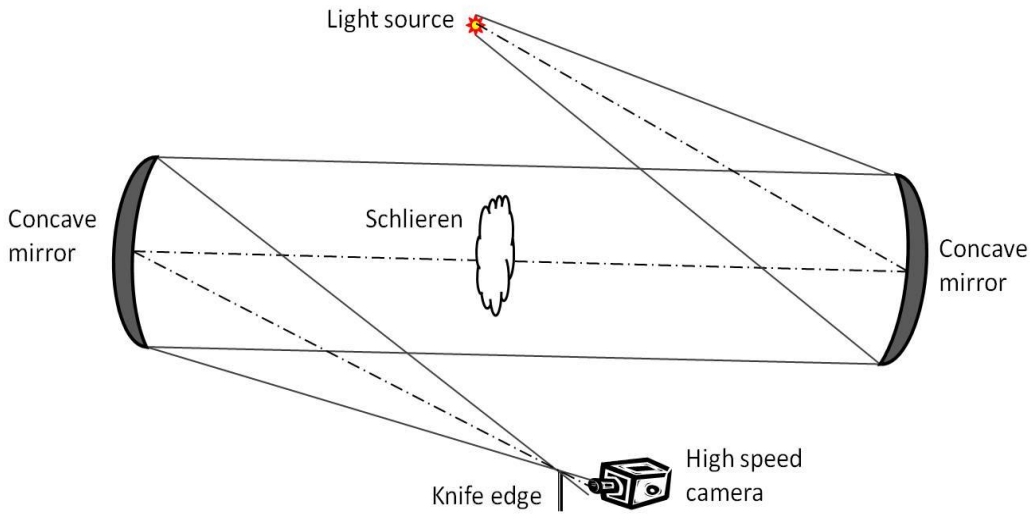

Figure 2.15: The arrangement of a Z-type schlieren system [92].

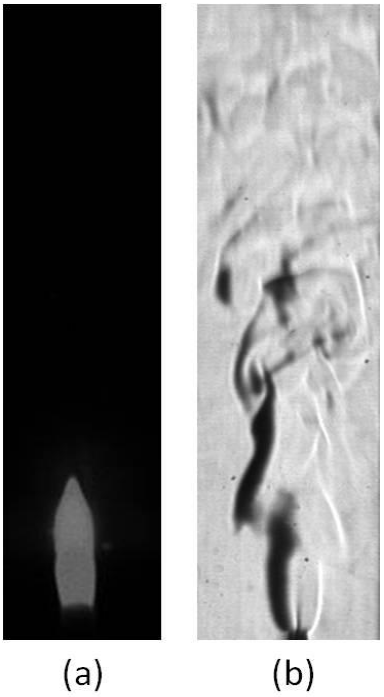

Figure 2.16: Typical schlieren image of diffusion flame, (a): Direct flame image, (b): Schlieren image.

The principle of the schlieren technique is based on the refraction of light. If the light goes through inhomogeneous media, the light beam will be distorted by the variations of refractive index caused by density gradients in the media. This distortion creates a spatial variation in the intensity of the light, which can be visualised directly on a viewing screen [91]. As shown in Fig. 2.17, the light goes through from medium 1 to medium 2. If the refractive indexes between two media are different, the original direction of the light will be changed. Snell's law [58] indicate that the angle changed depends on the refractive index difference:

$$n_1 \sin\theta_1 = n_2 \sin\theta_2 \tag{2-11}$$

According to the Gladstone-Dale Law [91], for specific species the refractive index n has linear relationship with density ρ :

$$n - 1 = k\rho \tag{2-12}$$

The angle changed by refraction is proportional to the density differences of the media. The refractivity $(n-1)$ of a gas shown in Eq. 2-12 depends on gas thermodynamics parameters, such as temperature, pressure and composition. The simple perfect-gas state equation shown in Eq. 2-13 can be applied in most cases. Table 2.2 shows the estimated refractive index of some species and the refractive index ratios [93].

$$p/\rho = RT \tag{2-13}$$

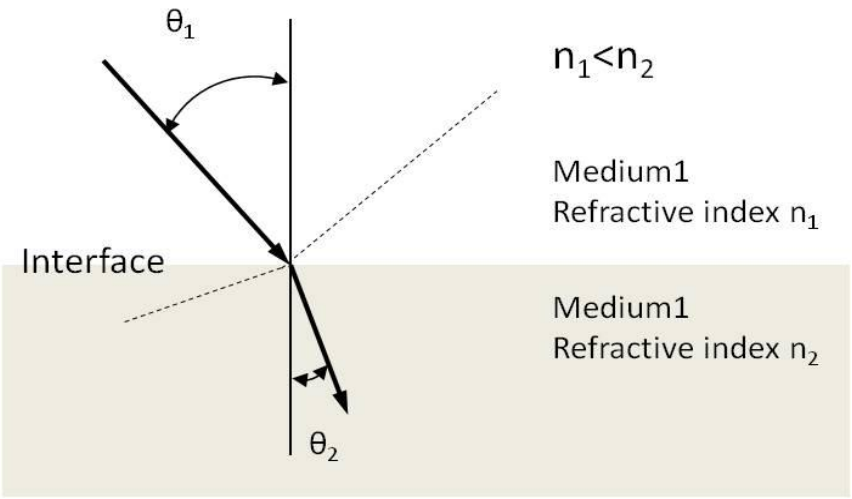

Figure 2.17: Schematic of the principle of the light refraction.

Table 2.2: Refractive index ratio between different species and air [93].

Category	**Refractive index**	**Refractive index ratio (n_1/n_2)**
Air	1.000292	1
Hydrogen	1.000132	0.99984
Helium	1.000035	0.99975
Nitrogen	1.000298	1.00001
Carbon dioxide	1.000449	1.00016
Methane	1.000444	1.00015
Carbon tetrachloride vapour	1.001768	1.00148
Shockwave front	1.0003~1.0015	1.00001~1.00121
Flame	1.0015~1.0021	1.00121~1.00181
Water	1.3	≈1.29962
Glass	> 1.3	> 1.29962

2.6 Emission Spectra of Flames

During the combustion reaction, many unstable radicals may be formed and can be recognised in the flame visible regions and near ultraviolet regions due to changes of electronic energy. These changes in the vibration energy of the atoms of the molecule determine the position of individual bands within the band system. The visible spectrum contains mostly CH, CO, and C_2, and a disperse cloud of such emitters does not reabsorb appreciably. Although the distribution of emitters varies through the reaction zone, the luminous sheet of the flame appears homogeneous at a distance, especially in the case of non-focused radiant flux measurement. Unfocused radiation measured at a distance from a flame is so weak that the photomultiplier tubes must be used to enhance the radiation signals. Photomultipliers tubes (PMTs), which convert incident light flux to a linearly proportional current, are extremely sensitive detectors of light in the ultraviolet, visible and near infrared region. They are constructed from a glass vacuum tube, which houses a photocathode, several dynodes, and an anode as shown in Fig. 2.18 [94]. The PMT's photocathode collects incoming photons and emits electrons in direct proportion to the incoming light flux. The emitted electrons impact the first dynode stage, with the dynode acting as an electron multiplier to emit multiple electrons for each incident electron. After several dynode stages, the electron flux can then amplified to the extent that a current can be measured. These detectors multiply the signal produced by incident light by as much as 10^8, from which single photons can be resolved.

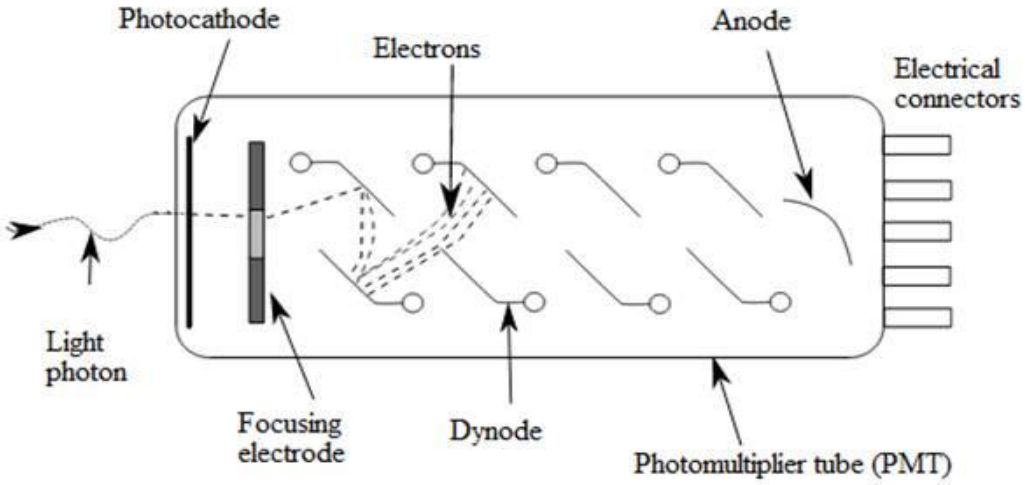

Figure 2.18: Schematic of a photomultiplier tube [94].

Spectral analysis consisting of sorting radiation arising from transition between energy states, in function of its wavelength, involves a distribution being called an emission spectrum. The radiation can fall into the visible domain or it can be comprised in the infrared and ultraviolet domains. This phenomenon is usually referred to as chemiluminescence which can potentially provide information about flame reaction zone conditions. OH*, CH* and C2* are common chemiluminescence species in hydrocarbon-air flames. The general examples for combustion reaction mechanism are shown in below: [40, 95, 96]

- **Formation of excited OH [40]:**

Excited OH radical, OH*, can be formed in the primary combustion zone by the following chemiluminescent reaction:

$CH + O_2 \rightarrow CO + OH^*$

Other possible reactions, importance for hydrogen flames, are:

$O + H \rightarrow OH^*$

$H + O_2 \rightarrow OH^* + O$

Here also intermediate excited states or complexes can occur. Furthermore, an OH radical can be raised from the ground state into the excited state when it is involved as a third partner in a recombination reaction between two other particles such as:

$OH + OH + H \rightarrow OH^* + H_2O$

This reaction explains why the presence of H and OH radical in hydrogen and acetylene flames in excess of their equilibrium concentration also leads to a superthermal excitation of the OH band above the primary combustion zone.

- **Formation of excited CH and C_2 [40]:**

The formation of excited CH and C2, CH* and C_2*, in flames has been debated for long time. Comparison of CH* emission from various flames leads to the conclusion that CH* is not formed by direct breakdown of acetylene but by a side reaction. The observation that CH* usually occurs higher in the reaction zone than C_2 suggests that it might be formed from C_2 by the reactions:

$C_2 + OH \rightarrow CO + CH^*$

$C_2H + O \rightarrow CO + CH^*$

which are exothermic. Concerning the formation of C_2* most of the studies favour the reactions:

$CH_2 + C \rightarrow H_2 + C_2$*

$CH + C \rightarrow H + C_2$*

2.7 Summary

The fundamental knowledge of combustion and the researches on Rijke type tube and thermoacoustic instability phenomena have been briefly surveyed. The literature has shown that this research field is very large. It is known that most of the researches in thermoacoustic instability focus on the self-driven oscillations or external excitation in the fuel pipe, and usually only analyse the flame dynamic itself. Relatively few studies applied an external excitation to affect the flame in a tube in order to examine the coupling of acoustic wave and reflected acoustic wave effect on flame flow field. Moreover, the observation of pure acoustic wave motion in this research area was rarely reported. Furthermore, reviews of the principles of present diagnostic apparatus and their relative applications to the observations of flames indicate that the PIV and schlieren systems are suitable for a better understanding of flame structure and flow velocity. The chemiluminescence emission measurement system can also be used to detect the frequency compound of flame oscillation under external forcing. These observations motivated the present study to apply the PIV and schlieren systems to examine the flow characterisation of diffusion flames in an acoustically excited tube.

Chapter 3

Experimental Setup and Methodology

The experimental method was adopted in this study to diagnose the behaviour of flame dynamics in an acoustically excited tube in order to examine the interaction phenomena between flames and acoustics. A square tube with a loudspeaker in the bottom of the tube was chosen as the main test rig. The Particle Image Velocimetry (PIV) and the Z-type high speed schlieren system were used to observe the flame dynamics and measure the flow field in the tube. The acoustic generating and control system and the other measurement devices, such as the high speed cameras, a chemiluminescence emission measurement system (PMT) and a microphone system are also introduced in this chapter.

3.1 Introduction

Figure 3.1 shows the main experimental arrangement, which consists of a burner system, a computer controlled 3D traverse, an acoustic signal generation and

synchronisation system and a PIV system. The detailed experimental arrangement and methodology are given in this section.

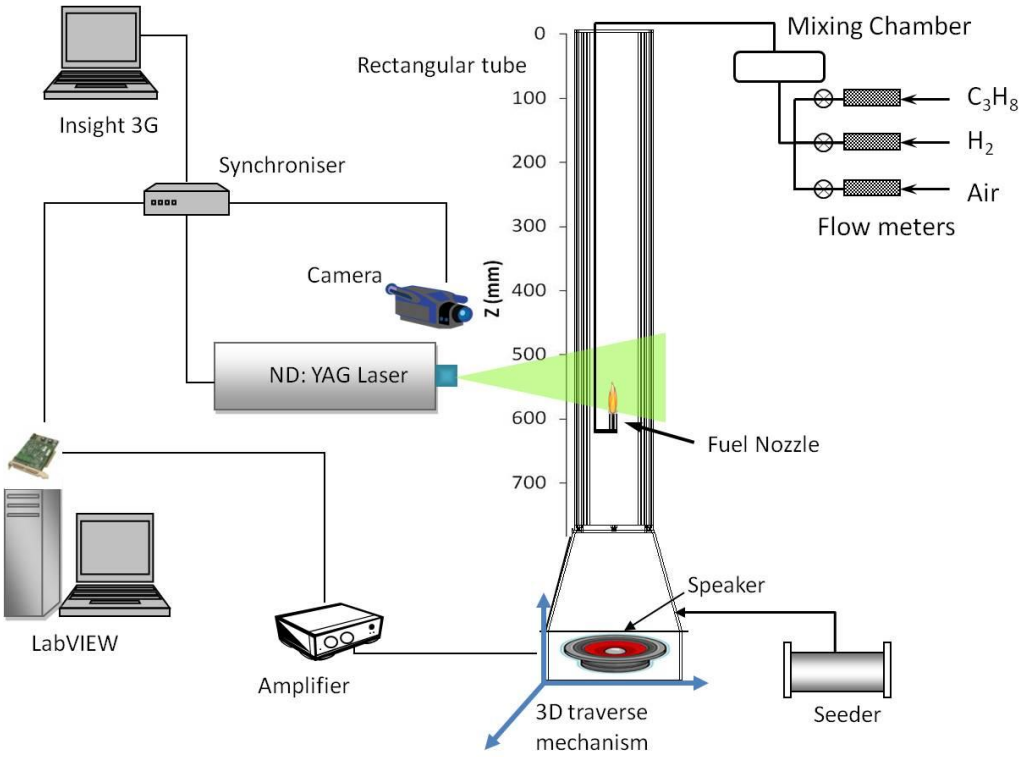

Figure 3.1: The experimental setup for the PIV measurement.

3.2 Burner System

The burner system includes a fuel supply system and a square tube (combustion chamber) in which a fuel nozzle is able to move up and down in the tube. The detailed burner system is introduced below.

3.2.1 Combustion Chamber

Since Rijke [97] reported the thermal generation of sound from a simple vertical tube and Rayleigh explained this phenomenon, the Rijke type tube has been widely

used in the investigation of thermoacoustic phenomena. The typical Rijke tube consists of a vertical cylindrical tube with gauze located in the lower half of the tube and heated by a flame. In this study, an external excitation system instead of self-exciting Rijke tube system was applied to observe the acoustic flow motion and also a square tube rather than a cylindrical tube was used in order to facilitate the PIV measurement. The wall of the tube consists of four glass panels which are supported by four steel beams and the tube is open to the atmosphere at the top end. The dimensions are 1,250 mm in total length (the box for loudspeaker is included) and 120 mm in width on each side. The loudspeaker is placed at the bottom of tube. Due to the diameter of the loudspeaker, and to compare better with previous research in the same group [40], there is a 300 mm height of pyramidal structure placed between the square tube and the loudspeaker. The width of the loudspeaker box is 210 mm and the observable area is approximately 800 mm. (The detail dimensions of test rig and the theoretical acoustic model of tube are discussed in section 4-1.) In order to get the uniform acoustic wave and seeded flow, a porous honeycomb was put at the bottom end of the square tube. The schematic of the square tube is shown in Fig. 3.2(a). The experimental setup for the Rijke type combustor is also shown in Fig. 3.1.

Due to the length of the rectangular tube, the view field of PIV CCD camera was set at a height of 100 mm in the vertical direction for each image. The entire velocity vector map was measured and synthesised from six different vertical locations, which were set from Z = 100 mm to Z = 700 mm (from the top end of the tube). The image timing could be triggered at any controlled acoustic phase angles. A sketch of

the view fields (view field 1 to view field 6) of the camera and the nozzle positions A, B and C are shown in Fig. 3.2(b).

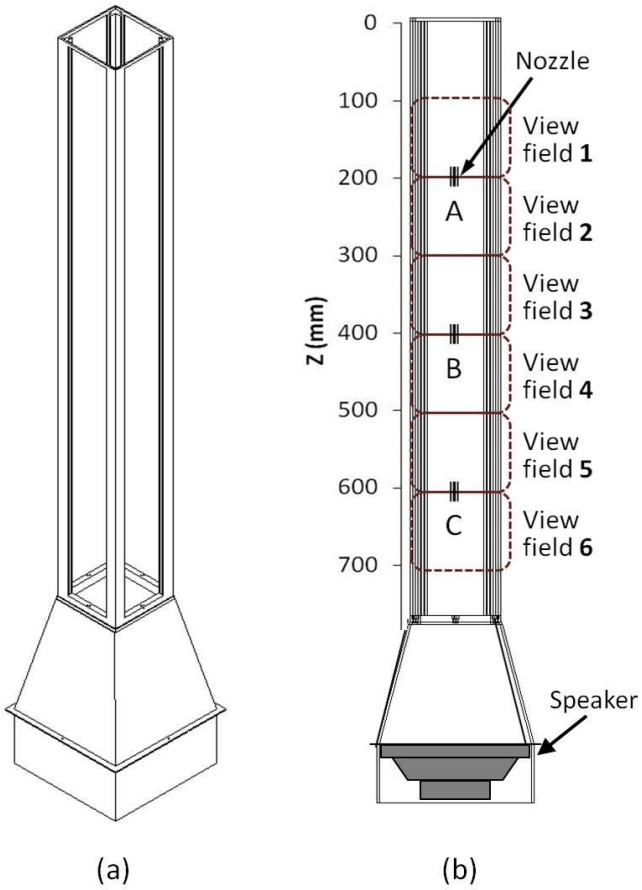

Figure 3.2: (a) Schematic of a square tube. (b) View field of camera and nozzle position.

3.2.2 The Fuel Flow System and 3D Traverse System

Fuel gas was supplied from the compressed gas bottle and the air was supplied from an air compressor. The flow rates were measured and controlled by the digital mass flow controllers (AALBORG GFC series) which were regulated by the LabVIEW system. For the diffusion flame, a flexible stainless fuel pipe was connected from the mass flow controller to the nozzle, which was an orifice at the end of the fuel

pipe with an inner diameter of 1.8 mm. The jet was ejected vertically upward into the air and was burned under the condition of natural convection. In the case of the propane/air premixed flame, the fuel flow system consisted of a piping system leading C_3H_8 and air along separate pipes into a mixing chamber first, and then to the burner nozzle. The burner nozzle had an inner diameter of 4 mm and the fuel was ignited with an electrical spark placed near the nozzle exit. The fuel nozzle position relative to the tube could be adjusted automatically by using a computer controlled 3D traverse system. The set up was arranged in such a way that the fuel nozzle position and PIV measurement area were fixed and the square tube and loudspeaker unit were moved relative to the fuel nozzle.

3.3 Signal Generating and Control System

3.3.1 Acoustic Generating System

The acoustic wave generating system produced the external acoustic excitation. It included a signal generator (NI DAQ), an audio amplifier and a loudspeaker. Table 3.1 shows the specifications of the loudspeaker (BUMPER model 0848 RF), which was an electromagnetic transducer used for converting electrical signals into sound. The loudspeaker is driven by a sine wave input generator and controlled by the PC base LabVIEW system. An acoustic wave signal was amplified by an audio amplifier before being sent into the loudspeaker. The forcing amplitude is defined by the peak-to-peak of the output voltage (V) of the amplifier. In order to prevent the combination of the out-of-phase acoustic waves from the back of the speaker and the in-phase acoustic waves from the front of the speaker, the loudspeaker drive

unit was enclosed as shown in Fig. 3.3. Moreover, increasing the sound transmits efficiency, and so a sound absorption sponge was placed at the back of the loudspeaker to absorb the out-of-phase acoustic waves and reduce the vibration from the loudspeaker.

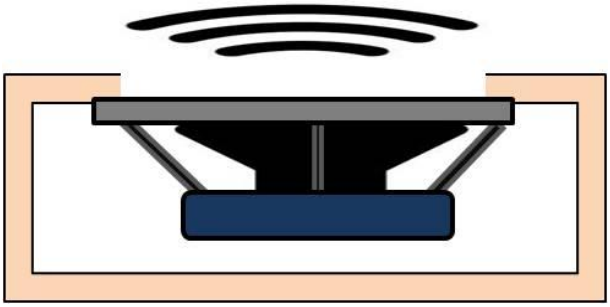

Figure 3.3: Schematic of loudspeaker closed enclosure type.

Table 3.1: Specifications of Loudspeaker.

Item	Specification
Advertised diameter	203.2 mm
Membrane cross-section area, S	0.0218 m^2
Loudspeaker resistance, R_E	4 Ω
Moving mass, m	0.0367 Kg
Force factor, Bl	10.61 Tm
Stiffness, s	5660 N/m
Damping, h	6 N s/m
Effective diaphragm radius	0.0875 m
Effective diaphragm area	0.02405 m^2
Voice coil length	3.4 m

A LabVIEW system was applied to control and synchronise the signal. A microphone and the chemiluminescence emission measurement were used to confirm that the acoustic frequency from loudspeaker was the same as the sending signals. Figure 3.4 illustrates the chemiluminescence emission signal of laminar diffusion flame at an external excitation frequency of 100 Hz, 150 Hz and 385 Hz. The results show that the peak signal in each case is exactly the same as the sending acoustic signal.

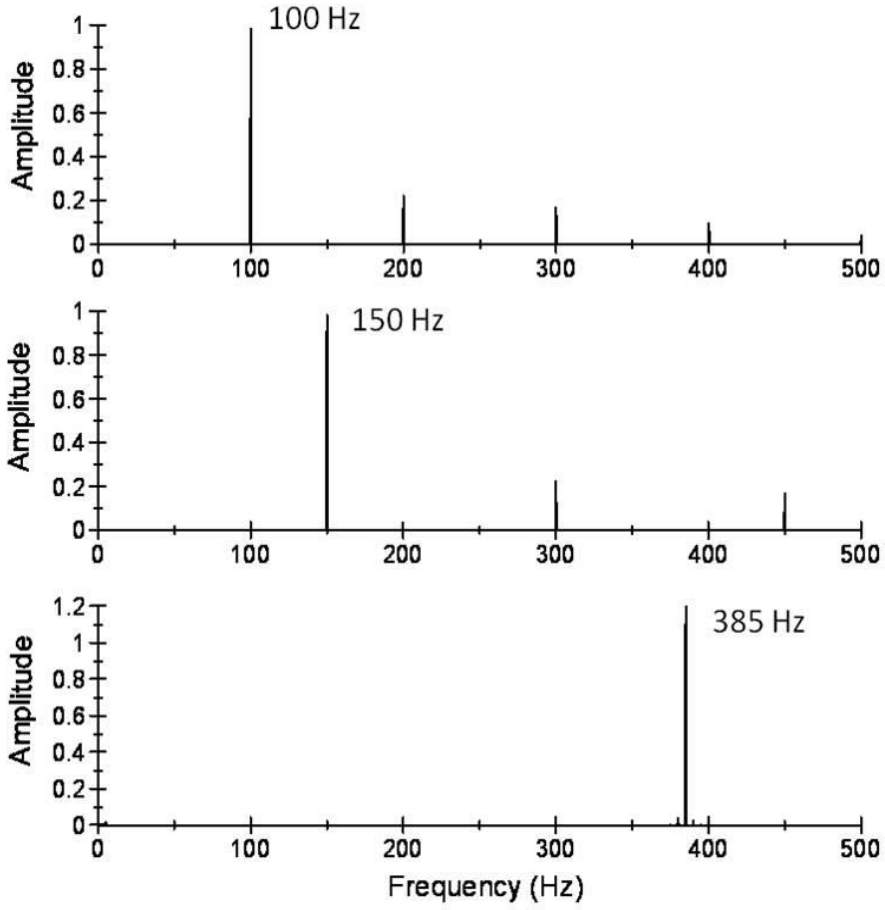

Figure 3.4: Power spectrum of CH^* chemiluminescence signals with excitation frequency of 100 Hz, 150 Hz and 385 Hz.

3.3.2 Data Acquisition System

The experimental devices need to be connected to a computer via the data acquisition system. The data acquisition card was an eight-slot NI cDAQ-9178 compact DAQ chassis with NI 9205 32 channel analogy input module and NI 9264 16 channel analogy output module. The general specifications for the DAQ card are shown in Table 3.2. In this study, the data acquisition card was used to acquire the chemiluminescence signal and acoustic data and send the synchronised signal to loudspeaker, high speed camera and PIV system. The signals of the mass flow meters were also acquire and send via this DAQ card. The software utilized was the LabVIEW version 8.2 by National Instruments.

Table 3.2: Data Acquisition Card Specifications.

Item	Specification
A/D channels input	32 Single-Ended / 16 Differential
A/D resolution input	16 bits
Maximum sampling rate	250 KHz
Bipolar input ranges	± 10 V
D/A channels output	16
D/A resolution output	16 bits
Application software support	NI LabVIEW

3.4 Schlieren System

A Z-type high speed schlieren imaging system was applied to visualise the flow dynamics and structures and to take advantage of its capability in differentiating fuel, burnt gas and ambient air. The schlieren system consisted of a 500 W xenon lamp and two λ/10 parabolic mirrors with diameters of 0.3048 m (12 inches) and focal lengths of 3.048 m (10 feet). A knife edge was placed at the focal point of the second parabolic mirror, where is just in front of camera, to adjust the brightness and contrast. All the schlieren images were recorded by a SA3 monochrome high speed camera at the full frame of 1024×1024 pixels. The experimental setup for schlieren system is shown in Fig. 3.5.

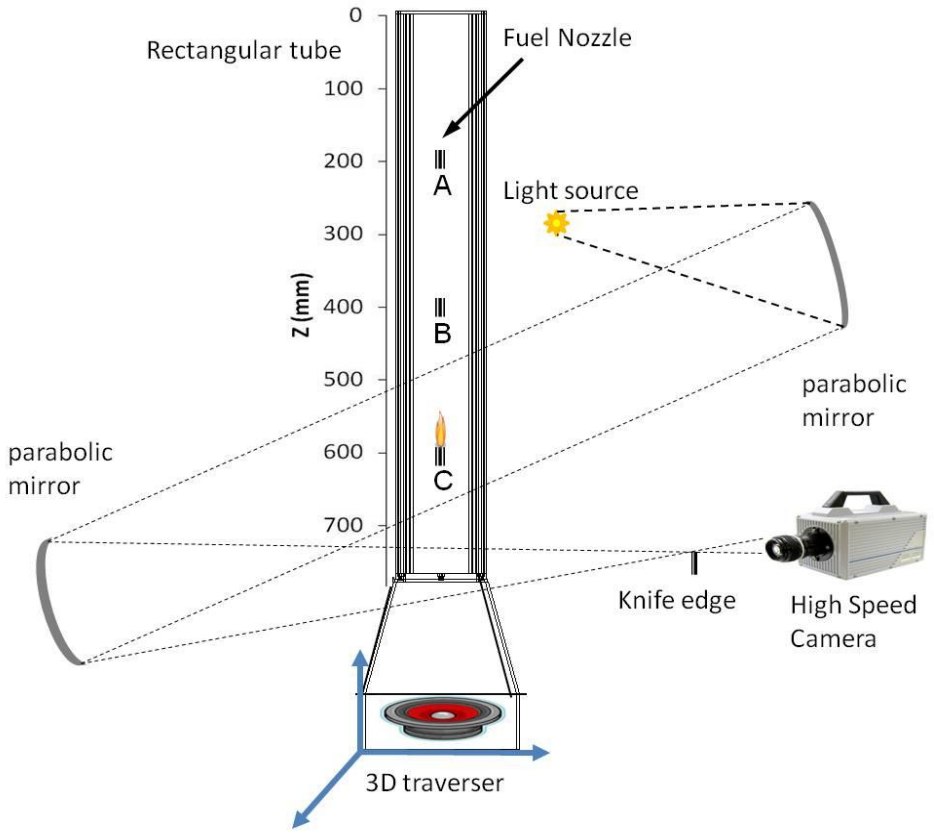

Figure 3.5: The experimental setup of schlieren system.

3.5 Particle Image Velocimetry

Acoustic flow field and flame flow field were measured by the PIV system. A commercial PIV system from TSI Inc. was used in this experiment, which consists of an illumination source (Laser), laser pulse synchroniser, seeding generator, data acquisition system and data analysis software. The experimental setup for the PIV measurement is shown in Fig. 3.1. The subsystems of the PIV system are briefly introduced in the following sections.

3.5.1 Laser System

PIV measurements were performed with a double-pulse ND: YAG laser, operating at a wavelength of 532 nm, a pulse rate of 15 Hz, and an energy per pulse of a maximum of 190 mJ/pulse with 2 μs between each pulse. It is synchronised with a CCD digital camera. The optic lens system controls the laser light sheet divergence angle and the beam waist location to satisfy the measurement requirements of the PIV system.

3.5.2 Recording and Control System

A TSI POWERVIEW™ Plus 4MP Camera was used in the PIV system to capture the particles images. This digital CCD camera offers a 2048 x 2048 pixel resolution with a pixel size of 7.4 μm × 7.4 μm, operating at 16 frames per second and providing a 12-bit output. In order to reduce the flame luminosity effects on the acquired images, a band-pass filter centered at 532 nm was placed in front of the camera lens.

The LASERPULSE Synchroniser Model 610035 from TSI is a timing control unit for the PIV applications. It automates control of the timing between laser pulses, camera, camera interfaces, and image acquisition with a 1 ns resolution. This synchroniser enables the system to be completely computer-controlled via a serial interface. For PIV measurements, these signals are controlled by the synchroniser via INSIGHT 3G Data Acquisition, Analysis and Display Software. In the current study, the PIV laser pulses and camera trigger timing have to be further synchronised with the acoustic signal. Therefore, the main trigger signal was sent from the NI LabVIEW system.

3.5.3 Seeding Generator

A solid particle generator (Dantec Dynamics, model 10F01) and 3 μm Titanium dioxide (TiO_2) seeding particles were used in this experiment. Figure 3.6 shows the photograph of the solid particle generator which includes a control unit, a stainless steel pressure vessel and a second powder container drum. It employs sonic jets, which create high shear flow fields that break up the powder while it is being dispensed in the outlet chamber. The powder density and the powder flow velocity and pressure can be controlled and adjusted by the control unit. In the practical application, in order to avoid the particles agglomerating and to provide the uniform size of particles, the particles have to be stored in a dry place and be further dried before the start of the experiment.

Figure 3.6: The photograph of solid particle generator (Dantec Dynamics model 10F01).

3.5.4 Operating Procedure

Setting up the PIV system was the first step of the experiment. The ND: YAG laser beam was sent through a series of optical lenses to convert the laser beam into a thin laser sheet (t ≈ 2 mm) in order to illuminate the seeding particles in the tube. A CCD camera was positioned normal to the laser sheet and the synchronised trigger signal was controlled by a computer system. Then it is essential that the seeding generator generates uniform and reliable seeding particles into the working fluid. The seeding particles were injected into the square tube from the bottom before the measurement. After the tube was filled with the seeding particles, the seeding generator was switched off. Then the laser system could start to capture the PIV data after a few seconds of settling time for the particles. The density of TiO_2 particle is higher than that of the air, and it was found that although the particles would fall down naturally due to the effect of the gravity, the averaged falling

velocity of the TiO_2 particles was observed to be in the range of 0.0017 m/s to 0.0043 m/s, which is significantly lower than the typical velocity range in the present experiment. Therefore, the gravity effect is considered to be negligible. The response time of particles is also considered in this study. According to Eq. 2-9 and Eq. 2-10, the TiO_2 particle's response time in the air is calculated as T_p = 11.7 μs. In the case of excitation frequency of 385 Hz, the response time is only 1/222 (0.45%) of the time period of the acoustic wave (the average diameter of TiO_2 seeding particles is assumed to be at 3 μm). Therefore the particles should be able to follow the air flow. The detail particle response time divided by the time period of different frequency of acoustic wave is shown in Table 3.3.

Table 3.3: Laser pulse separation timing and the error of response time in each experimental condition.

Excitation Frequency of Loudspeaker	Laser Pulse Separation (dT)	Error of Response Time
< 200 Hz	350 μs	< 0.23%
220 Hz	200 μs	0.26%
385 Hz	200 μs	0.45%
550 Hz	100 μs	0.64%

After the seeding generator was set, selecting an optimum laser trigger timing and camera shutter speed is another vital step. According to the suggestion from TSI, the maximum allowed particle displacement between frame A and frame B is 25% of the size of interrogation region. The laser pulses and the camera shutters can significantly effect this displacement distance and further effect the measurement accuracy.

In this study, a laser and a camera trigger timing diagram is shown in figure 3.7. The camera shutter speed of frame B was fixed at 60 ms. The camera shutter speed of frame A can be adjusted to fit the laser pulse. Both the laser pulse timing and the camera shutter speed of frame A are based on the frequency of acoustic signal and the rough mean flow velocity. In this experiment, according to the frequency and flow characterisation, the laser pulse between two frames was set from 100 μs to 350 μs. Detail laser pulse timing in each experimental condition is shown in Table 3.3. Figure 3.8 shows an example of the laser pulse timing of acoustic velocity and the acoustic streaming velocity. The main point of the present study is to know the acoustic flow velocity. In order to avoid the misreading to the velocity of acoustic streaming and to consider the accuracy of PIV measurements, the timing of laser pulse between two frames was set at least less than 1/10 of one excitation cycle. Moreover, the delay timing of first laser pulse was 495 ns which was 5 ns before frame B was triggered. Regarding the shutter speed of the camera, it was set at 500 ns in frame A, and in frame B, it was fixed at 60 ms.

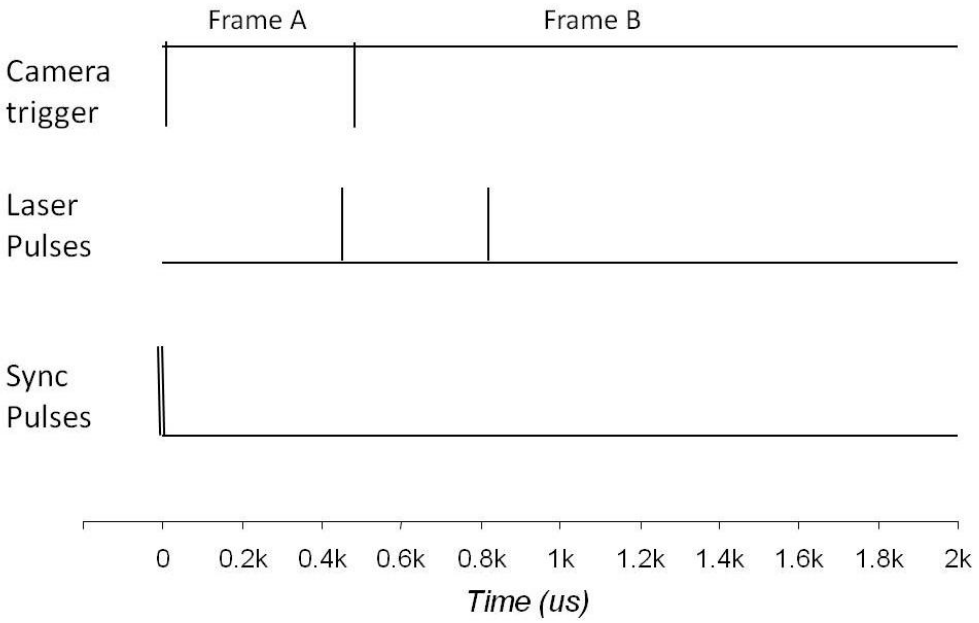

Figure 3.7: Laser pulse and camera trigger timing diagram.

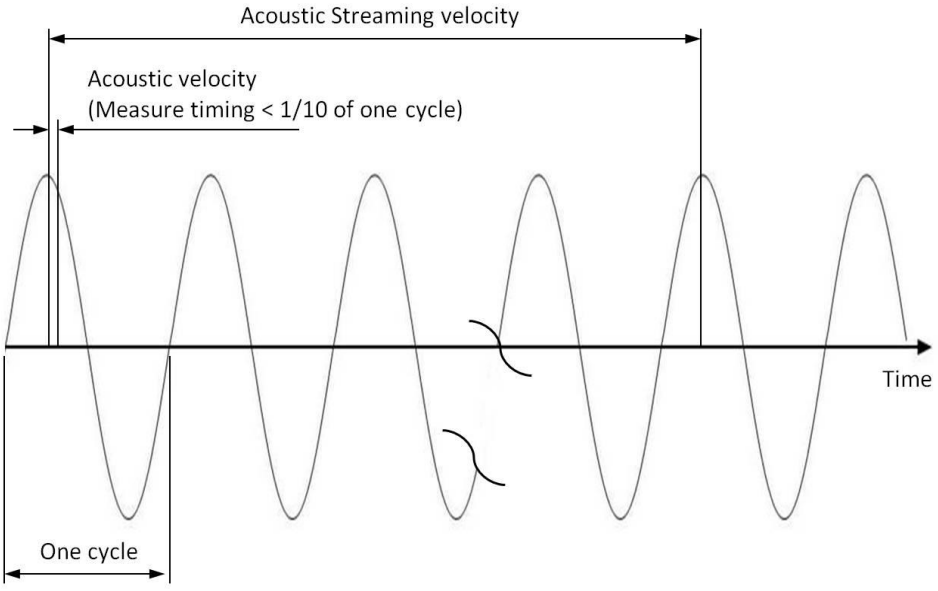

Figure 3.8 An example of the laser pulse timing of acoustic velocity and the acoustic streaming velocity.

3.5.5 Data Processing System

After the particle images were captured, processing and analysis of these images to get the velocity and vector information of flow field was necessary. The TSI “Insight 3G Image Capture, Analysis, and Display Software Platform” was the main software used to process the PIV images.

Firstly, the spatial calibration for the images needed to be setup. A saved pre-captured ruler image with a calibration function file was opened and a known distance measured. The pixel unit of the image could then be converted to millimetres. Then the calibrated data was saved in the system to provide the reference data to other PIV images. The next step was to pre-process the selected images to improve the raw image quality before PIV processing. In the present study, uniform seeding particles into experimental environment was achieved and masking image was the only function applied to define a processing area.

Figure 3.9 illustrates the PIV image processing steps from raw image to the velocity contour and vector map. The zoomed-in interrogation area and its correlation map were also shown. After the PIV raw image was selected, the processing parameters need to be selected. Settings depended on the flow, velocity gradients, acoustic signal and image quality. In the present study, a standard Fast Fourier Transform (FFT) cross-correlation and Gaussian peak detection algorithm were chosen to calculate the velocity vectors. In the cold acoustic flow cases, the interrogation area was 32 × 32 pixels, whereas in cases where combustion was present in an area of 64 x 64 pixels.

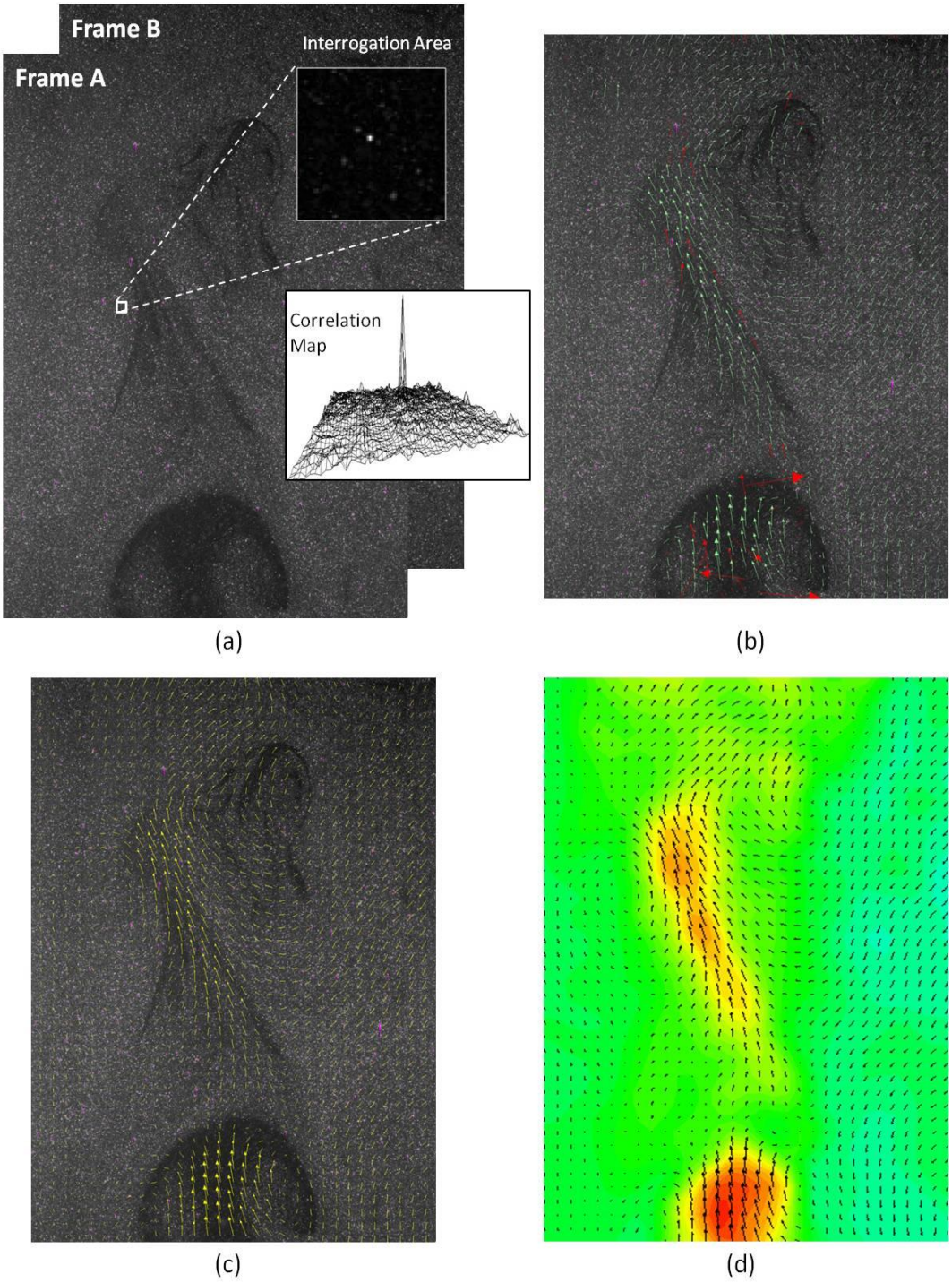

Figure 3.9 The diagrams of the PIV image processing steps. (a) Raw images, interrogation area (64 X 64) and correlation map, (b) After processing step, (c) After post-processing step and (d) Velocity contour and vector map presented by Tecplot.

Figure 3.9(a) shows the pair of the raw images which was taken in the case with flame in the bottom of the rig. Due to the large velocity gradient between upwardly propagating hot combustion gases and surrounding cold acoustic flow, the distribution of seeding particles was not uniform across the image. Figure 3.9(b) shows the calculated result after processing, here a 64 X 64 interrogation area was chosen. However, there are still some spurious vectors. (Shown in red) These make up less than 3.5 % of total vectors. The spurious vectors were detected by using a 'neighbourhood mean' filter, which removed vectors that were out of the range of the mean value ± 2 times standard deviation in a window size of 3 × 3. The resultant filtered vector map is shown in Fig. 3.9(c). Finally, the data was further processed and presented via Tecplot or MATLAB software; see Figure 3.9(d).

PIV measurement theory indicated that the estimation of each velocity vector can be affected by bias and sub-pixel errors [67]. Bias is the result of incorrect choice of PIV settings such that some velocity information cannot be captured. An example is when the capture timing between two frames is too short; the particle displacements are under-resolved. Then the bias error could be happened. Regarding the sub-pixel error, it is caused by the estimated displacements are ''locked'' toward integer pixel values. Figure 3.10 presents the peak-locking effects. Take an example, for a true mean particle displacement of 7.85 pixels, the sub-pixel estimator will ''lock'' the estimated displacement closer to 8 pixels. For a true mean particle displacement of 8.15 pixels would also be estimated closer to 8 pixels.

To investigate the accuracy of the PIV results, measured particle displacements were examined. Figure 3.11 illustrates an example of the acoustic cold flow vector map and the histogram of PIV particle displacements. Results showed that 84% of the particle displacements were within 6.5-7.5 % of the size of the interrogation area. Clearly the majority of particles have remained within the interrogation area resulting in low noise and this in term will avoid bias as all particle displacements are likely to be captured. Regarding the sub-pixel error, in a two-dimensional velocity field, the peak-locking phenomenon is the main source of sub-pixel error [67, 98]. In Fig. 3.11(b), there is no noticeable peak-locking effect in the histogram. These results demonstrate that suitable PIV settings have been used for the cold flow experiments and given confidence when compared to theoretical results in chapter 4.

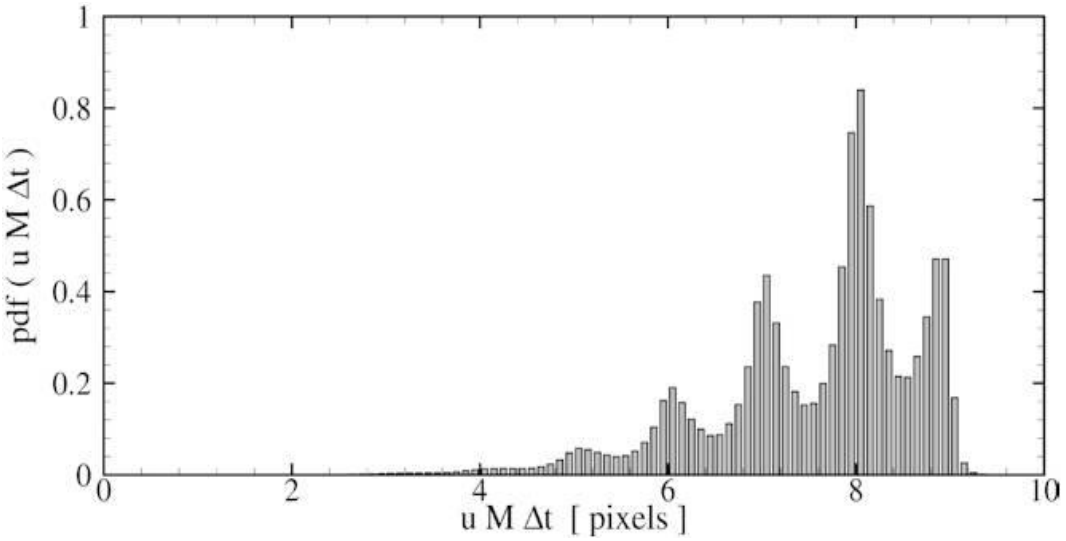

Figure 3.10 An example of particle-image displacement illustrating peak-locking effects [98].

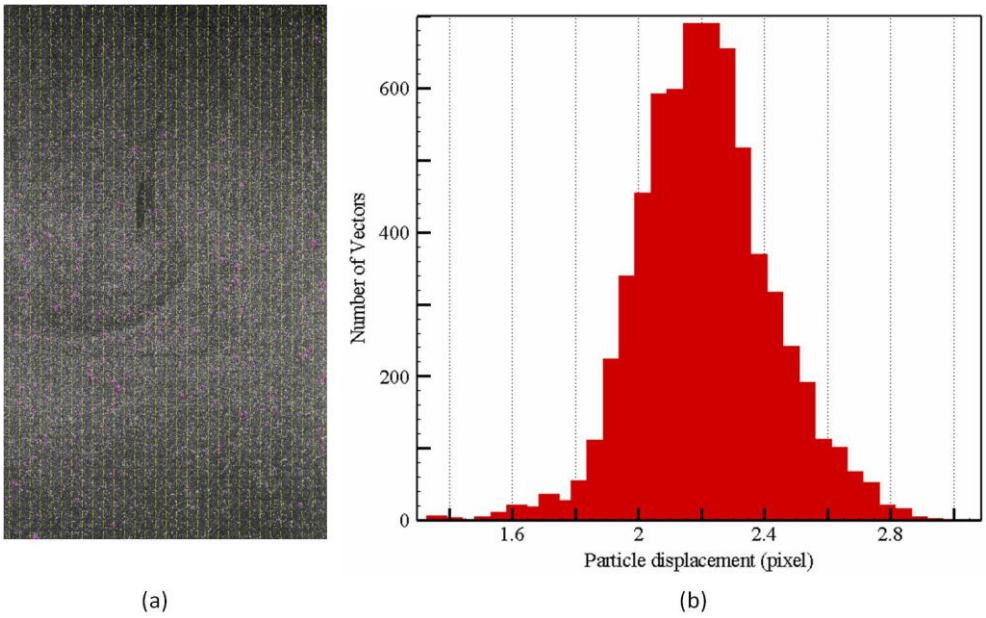

Figure 3.11 (a) The vector map of acoustic cold flow (32 X 32 interrogation area, the spatial resolution approx. 1.9 mm) and (b) the histogram of actual PIV particle displacement data. Histogram bin-width = 0.05 pixel.

3.6 Other Measurement Units

In order to quantify and specify the experiment data, the chemiluminescence emission measurement unit (PMT), the monochrome and colour high speed camera and a microphone were applied in this study. The experimental setup is shown in Fig. 3.12.

3.6.1 Chemiluminescence Emission Measurement

The chemiluminescence emission measurement apparatus consists of two photomultipliers (ORIEL, Model: 70704), a high voltage source supply, a converging lens arrangement, optical filters, and a randomly bifurcated fine fibre optic bundle. This optical system was designed to measure the flame chemiluminescence

intensity which was performed by the photomultiplier-tube (PMT). The filtering of the light collected from the flame used a set of monochromatic filters. Transmission of the light signal was accomplished using a fibre optic cable. The CH* chemiluminescence was collected by a lens system which is designed to image the flame onto the end of fibre optic cable. The data output from the multipliers were displayed and stored in a PC based system. The National Instruments DAQ card and LabVIEW software were then employed for data acquisition, monitoring and analysis. The setup of the chemiluminescence emission measurement system is shown in the right hand side of Fig. 3.12.

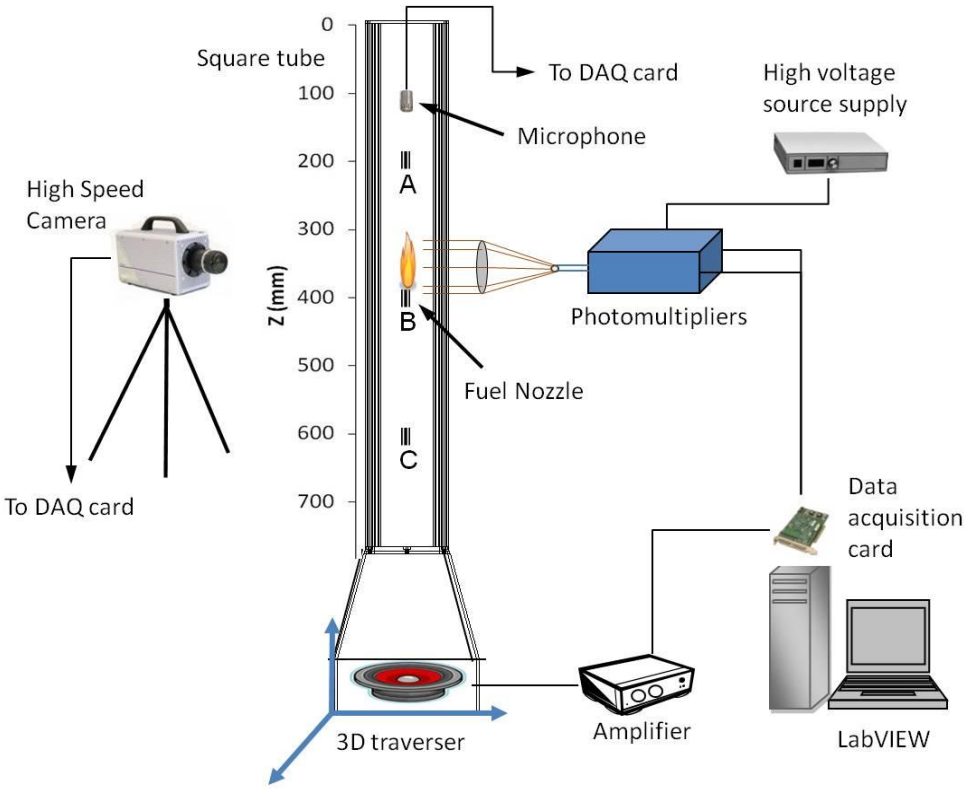

Figure 3.12: The experimental setup of the chemiluminescence emission measurement unit, high speed camera and the microphone.

3.6.2 High Speed Camera

Photron FASTCAM-SA3 monochrome and FASTCAM-SA4 colour high-speed video cameras were employed for capturing the schlieren images and the visible flame images respectively. A photograph of the SA3 camera is shown in Fig. 3.13 and the detailed specifications for the camera are shown in Table 3.4. The camera provides a frame rate of 5,400 fps at full resolution of 1024 x 1024 pixels and up to 120,000 fps at reduced resolution settings. The function of the FASTCAM-SA4 camera is similar to the SA3, but it provides colour images with a frame rate of 3,600 fps at full resolution of 1024 x 1024 pixels and up to 500,000 fps at reduced resolution settings. Both cameras provide the selectable TTL triggering signal which can be synchronised together or connected with the DAQ card to synchronise with the other devices.

Figure 3.13: Photron FASTCAM-SA3 high-speed camera.

Table 3.4: Specifications of Photron FASTCAM-SA3 high-speed camera.

Item	Specification
Sensor	12 bit CMOS with 20 µm pixel
Shutter	Electronic shutter speed from 16.7 ms to 2 µs, independent of frame rate
Memory	8 GB, 5400 frames (1024 x 1024 x 12 bits)
Camera Control	Through keypad with integrated viewfinder and Ethernet
Low light mode	Low ambient light, high frame rate or short exposure modes
Triggering	Selectable positive or negative TTL or switch closure
Timing	Internal clock or external source
Phase Lock	Enables synchronisation with a camera or external source
Data Acquisition	Photron MCDL and PCI DAQ cards
Power	100 V - 240 V AC, 1.5 A, 50-60 Hz

3.6.3 Acoustic Measurement

A PCB Piezotronics Model 377C10 microphone with a PCB signal conditioner Model 482C05 was applied to measure the acoustic pressure in the tube. The specifications of the microphone have been listed in Table 3.5. The signal obtained from microphone was collected by a data acquisition card (see section 3.3.2) and was processed by the NI LabVIEW system. The measurment position of the microphone was fixed and the square tube could be moved relative to the microphone. Hence the pressure field along the whole tube could be measured.

Table 3.5: The Specifications of the Microphone.

Item	Specification
Open Circuit Sensitivity (at 250 Hz)	1.0 mV/Pa
Open Circuit Sensitivity (± 3 dB)	-60 dB re 1 V/Pa
Frequency Range (± 2 dB)	4.0 to 70,000 Hz
Resonant Frequency	65 kHz
Dynamic Range	35-165 dB re 20 µPa
Low Noise Coaxial Cable x 2	3 m x 2

3.7 Summary

The experimental apparatus and operation procedures have been discussed in this chapter. The burner system, signal generating system, control system, data acquisition system and measurement devices have been described in detail. Quantitative measurements can be made by using Particle Image Velocimetry to observe the flow characteristics of acoustic waves and flame flow. Visualisation of the flame dynamics and structures can be achieved by using the Z-type high speed schlieren system. Photomultipliers tube was used to analyse the frequency component of flame/acoustic coupling effect under external forcing. The whole experimental system can then provide sufficient data for the analysis of the interaction phenomena between the flame dynamics and acoustic wave.

Chapter 4

Design, Testing and Preparation for the Experimental System

Particle Image Velocimetry is the main diagnostic tool in this study and is also new equipment in this research group. In order to facilitate the PIV measurement, a square tube was designed for the PIV experimental study. The acoustics of the tube introduced in the previous chapter were investigated using simple analytical expressions. In this chapter, the theoretical model was adopted to analyse the acoustic characterisation of the tube. These predictions were then confirmed using measurements of acoustic waves in the rig. Besides, although PIV has been become a commercial experimental device, using it appropriately in each specific experimental condition is still difficult. The biggest challenge is to take a suitable and high quality raw PIV image. This includes the selection of seeding particles, the seeding methods, and the trigger timing of the camera and laser. Processing and statistics the captured image data correctly is the next challenge in using PIV. The

purpose of this chapter is to present the preparation works for the PIV experimental study.

4.1 Square Tube

A square tube with a loudspeaker in the bottom of tube was used in this study as a setup for investigating the thermoacoustic phenomenon. The fundamental analysis of this acoustical system is given here. As mentioned in section 3.2, a square tube, instead of a cylindrical tube, was designed to facilitate the PIV and schlieren measurement in order to avoid the reflection from the curved surface. Due to the diameter of loudspeaker, the cross-section of the tube is slightly enlarged and forms a pyramidal structure in the lower half of the tube. This design is different from the simple theoretical acoustic analysis for one single straight tube. The difference between these two shapes of tube has been considered as following section.

4.1.1 Theoretical Acoustic Model

Due to the non-constant cross section of square tube, the acoustic equations for acoustic field in each part of tube are required. A similar shape of the square tube has been analysed by Marx et al. [99]. The result matched well with the experimental data. The test tube in the present study is smaller, the shape is simpler and the upper end of the tube is open. The detail geometry of square tube is shown in Fig. 4.1. The acoustic equations for each part of tube and the

mechanical characterisation of loudspeaker and its equations are discussed in the following paragraphs [99-101].

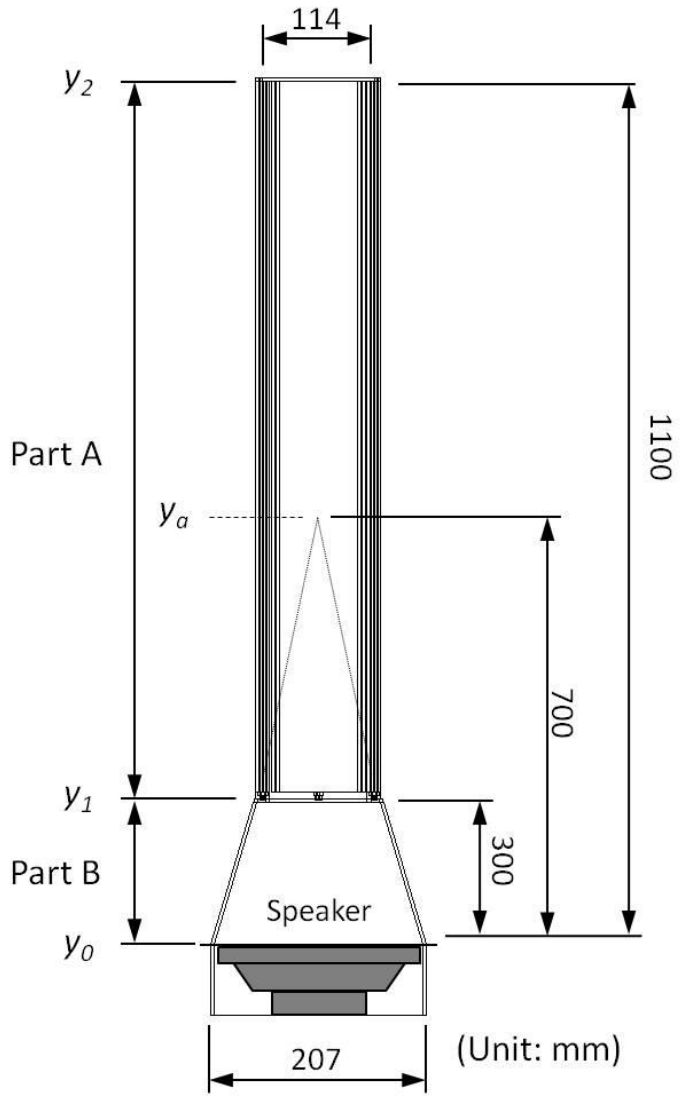

Figure 4.1: Schematic of the geometry of the square tube and loudspeaker.

- Acoustic equations

For part A, the linear acoustic equation for the complex acoustic pressure p in a square tube is [100]:

$$[1 + (\gamma - 1)f_k]p + \frac{C_0^2}{\omega^2}(1 - f_v)\frac{d^2p}{dx^2} = 0 \quad (4\text{-}1)$$

The functions f_k and f_v are thermal and viscous functions and depend on the geometry of the channel. Their expressions in the boundary layer approximation for a square tube of half-side length r are:

$$f_v = (1 - i)\frac{\delta_v}{r} \text{ and } f_k = (1 - i)\frac{\delta_k}{r} \quad (4\text{-}2)$$

where the viscous and thermal penetration depths are defined by:

$$\delta_v = \sqrt{2v/\omega} \text{ and } \delta_k = \sqrt{2k/\omega} \quad (4\text{-}3)$$

The boundary layer approximation holds as long as $r \gg \delta_v, \delta_k$, which is the condition in the present experimental. In these expressions, v is the kinematic viscosity, k is the thermal diffusivity defined by:

$$k = K/\rho_0 C_p \quad (4\text{-}4)$$

where K is the fluid thermal conductivity,

ρ_0 is ambient density,

C_p is isobaric specific heat,

γ is the ratio of specific heats and

c_0 is the speed of sound.

The working fluid is air, assumed to be a perfect gas of perfect gas constant R_{air}. Thus,

$$C_p = {\gamma R_{air}}/{(\gamma - 1)} \tag{4-5}$$

The physical properties of working fluids are as following [73]: $R_{air} = 287\ {J}/{Kg \cdot K}$, $V = 1.5 \times 10^{-5}\ {m^2}/{s}, \gamma = 1.4$, $T_0 = 293.15\ K$, $P_0 = 10^5\ Pa,$ and $C_0 = \sqrt{\gamma T_0 R_{air}}$. The section-averaged complex acoustic velocity is given by the Eq. 4-6.

$$u = -\frac{(1-f_v)}{i\omega\rho_0}\frac{d_p}{d_x} \tag{4-6}$$

For part B, in order to simplify the analytical results, thermoviscous effects are neglect. The pyramidal section is short, so that this does not affect the result significantly. Thus equation for pressure in part B is given by Eq. 4-7 [99]:

$$\frac{\partial^2 p}{\partial t^2} - \frac{C_0^2}{y'^2}\frac{\partial}{\partial y'}\left(x'^2\frac{\partial p}{\partial y'}\right) = 0 \tag{4-7}$$

This equation is simply the propagation equation written in spherical coordinates, where radial coordinate is $y' = y - y_a$. The velocity is given by the spherical momentum equation:

$$\rho_0\frac{\partial u}{\partial t} = -\frac{\partial p}{\partial y'} \tag{4-8}$$

- General solutions

The general solution of Eq. 4-1 and Eq. 4-6 to Eq. 4-8 are written for part A and part B of the tube.

For Part A ($y_1 \leq y \leq y_2$):

$$p_A = A\left(e^{-ik_A y} + R_A e^{ik_A y}\right), \tag{4-9}$$

$$u_A = \frac{k_A(1-f_{v,A})}{\omega\rho_0} A\left(e^{-ik_A y} - R_A e^{ik_A y}\right), \tag{4-10}$$

$$k_A = \frac{\omega}{c_0}\sqrt{\frac{1+(\gamma-1)f_{k,A}}{1-f_{v,A}}}, \tag{4-11}$$

$$f_{v,A} = (1-i)\frac{\delta_v}{r_A}, \quad f_{k,A} = (1-i)\frac{\delta_k}{r_A}. \tag{4-12}$$

For part B ($y_0 \leq y \leq y_1$) and $y' = y - y_a$:

$$p_B = \frac{B}{x'}\left(e^{-ik_B y'} + R_B e^{ik_B y'}\right), \tag{4-13}$$

$$u_B = \frac{1}{\rho_0 c_0}\frac{B}{y'}\left[\left(1 - \frac{i}{k_B y'}\right)e^{-ik_B y'} - R_B\left(1 + \frac{i}{k_B y'}\right)e^{ik_B y'}\right], \tag{4-14}$$

$$k_B = {}^{\omega}/_{c_0}. \tag{4-15}$$

The amplitudes of the travelling waves are A and B in parts A and B. The reflection coefficients are R_A and R_B.

- Joining conditions

The joining conditions are the pressure and volume flow rate continuity:

$$y = y_0: \quad S_B u_B(y_0) = U_0, \tag{4-16}$$

$$y = y_1: \quad p_B(y_1) = p_A(y_1), \tag{4-17}$$

$$S_B u_B(y_1) = S_A(y_1) u_A(y_1), \tag{4-18}$$

$$y = y_2: \quad p_A(y_2) = 0, \tag{4-19}$$

where S_A is the cross-section area of part A at ordinate y, $S_B(x)$ is the cross-section area of part B. U_0 is the volume flow rate at the loudspeaker membrane. The loudspeaker equation is given below:

- Loudspeaker equations

A linear model of the loudspeaker is used in the present study. The most important parameters for the loudspeaker are the electrical resistance R_e ; the force factor Bl; the damping h, the stiffness s, and the moving mass m. If the voltage amplitude V_e is sent to the loudspeaker, the volume velocity at the membrane U_0 is:

$$U_0 = S \frac{Bl}{Z_e(Z_{mec} + S^2 Z_{ac}) + (Bl)^2} V_e, \tag{4-20}$$

where

$$Z_e = R_e + iL_e\omega, \tag{4-21}$$

$$Z_{mec} = h + i(m\omega - {}^{S}/_{\omega}), \tag{4-22}$$

$$Z_{ac} = \frac{p_B(y_0)}{S_B u_B(y_0)} \tag{4-23}$$

where S is the loudspeaker membrane cross-section area,

Z_e is the electrical impedance of the loudspeaker coil,

Z_{mec} is the mechanical impedance of the loudspeaker,

Z_{ac} is the acoustical impedance of the resonator,

The relative linear parameters of loudspeaker and the loudspeaker membrane cross-section area are given in Table 3.1.

- Solution

According to the abovementioned acoustic equations (Eq. 4-9 to Eq. 4-15), the joining conditions (Eq. 4-16 to Eq. 4-19), and the electromechanical equation of the loudspeaker (Eq. 4-20), the solution of $R_A, R_B, Z_{ac}, U_0, A\ and\ B$ can be found. The upper end of the tube is opened; hence the pressure oscillation is to be assumed as zero at y_2. Then R_A and R_B can be found:

$$R_A = -e^{-2ik_A y_2}, \tag{4-24}$$

$$R_B = \frac{\frac{Z_1}{Z_{s,B,1}}\left(1 - \frac{i}{k_B y_1'}\right) - 1}{1 + \frac{Z_1}{Z_{s,B,1}}\left(1 + \frac{i}{k_B y_1'}\right)} e^{-2ik_B y_1'}, \tag{4-25}$$

where

$$Z_1 = Z_{s,A}\frac{e^{-ik_A y_1} + R_A e^{ik_A y_1}}{e^{-ik_A y_1} - R_A e^{ik_A y_1}}, \tag{4-26}$$

$$Z_{s,A} = \frac{\omega\rho_0}{S_A k_A\left(1 - f_{v,A}\right)}, \qquad (4-27)$$

$$Z_{s,B,1} = \frac{\rho_0 c_0}{S_B(y_1)}, \qquad (4-28)$$

$$Z_{s,B,0} = \frac{\rho_0 c_0}{S_B(y_0)}. \qquad (4-29)$$

Knowing the reflection coefficient R_B in part B, the acoustic impedance Z_{ac} can be calculated:

$$Z_{ac} = Z_{s,B}\frac{e^{-ik_B y_o} + R_B e^{ik_B y_0}}{e^{-ik_B y_o} - R_B e^{ik_B y_0}}. \qquad (4-30)$$

Now, the loudspeaker membrane U_0 in Eq. 4-20 can be calculated. Then the direct coefficients can be known:

$$\mathrm{B} = \mathrm{Z_{s,B0}} y_0' \mathrm{U_0}\frac{1}{\left[\left(1 - \frac{i}{k_B y_0'}\right)e^{-ik_B y_0'} - R_B\left(1 + \frac{i}{k_B y_0'}\right)e^{ik_B y_0'}\right]}, \qquad (4-31)$$

$$\mathrm{A} = \frac{\mathrm{B}}{\mathrm{y_1'}}\frac{e^{-ik_B \mathrm{y_1'}} + R_B e^{ik_B \mathrm{y_1'}}}{e^{-ik_A y_1} + R_A e^{ik_A y_1}}. \qquad (4-32)$$

According to these formulas, the theoretical acoustic characteristic in the tube can be calculated.

4.1.2 Theoretical Prediction of Acoustic Response of the Tube

Figure 4.2(a) shows the theoretical predictions of the frequency response of the tube. The result shows that the first four resonance frequencies are 63.6 Hz, 218 Hz, 385.1 Hz and 547.7 Hz respectively. To confirm this prediction, experimental measurements of the acoustic responses were made along the whole length of the tube using a microphone. (Detail specifications of microphone can be found in section 3.6.3.) Shown in the Fig. 4.2(b) are measurements made above the loudspeaker which correspond to the same position as Fig. 4.2(a). The experimental observation in Fig. 4.2(b) indicates that the first four mode of the present rig are 65 Hz, 220 Hz, 385 Hz and 550 Hz respectively. (The measure range of excitation frequency was between 20 Hz and 600 Hz in increments of 5 Hz at the voltage amplitude of 5 V.) The results of frequency response compare well with the theoretical predict data. However, the pressure value of theoretical predictions is higher than that the measured pressure data. The error is increasing from 23% for the first resonance frequency to 43.3% for the forth resonance frequency. Many factors could affect the error between theory and measurements. The similar results, which showed the disagreement between theory and measurements was increased with the increasing of excitation frequency, were also observed by the Bailliet et al. [102] and Marx et al. [99].

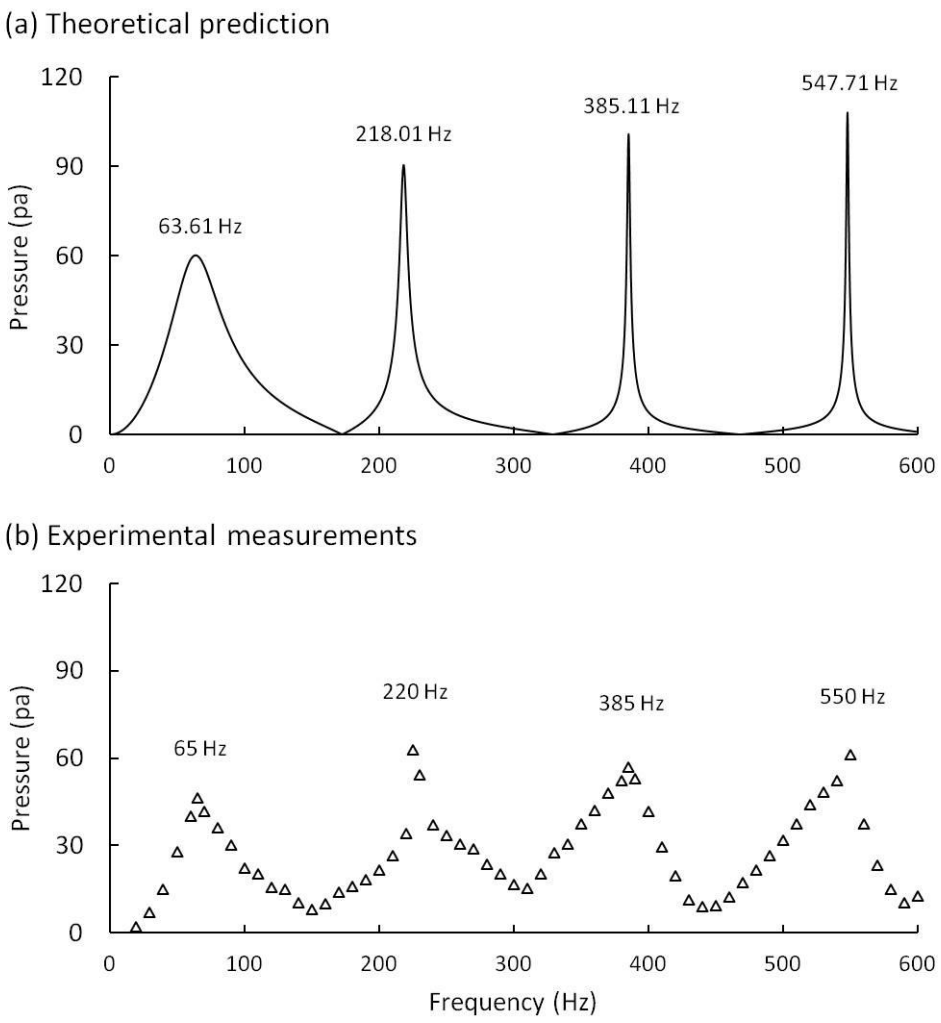

Figure 4.2: The frequency response of the tube. (a) Theoretical prediction, (b) Pressure measurements. (Both relate to y_0)

In the present study, the upper end of the tube is open. Hence the pressure oscillation in the open end of the tube was assumed as zero at theoretical model. However, in the practical situations, the large pressure drop loss could happen in the open end of the tube (see Fig. 4.3 at Z = 1.1m). This could increase the error between theoretical prediction and experimental measurements. Moreover, the measured pressure peak of the resonance frequencies was not very sharp as theoretical prediction. Also, the trend of frequency response in the bottom area of

Fig. 4.2(b) was broader than Fig. 4.2(a). There is no relating experiments result about this phenomenon in literature. However, some reasons could cause this error. Firstly, as mentioned in previous paragraph, the pressure drop loss is the main reason to cause this error. Secondly, the measure range of excitation frequency was in increments of 5 Hz. This was much larger than the frequency range of theoretical calculation which was 0.1 Hz. Hence the real peak of resonance frequencies could be missed in the experimental measurements. However, the overall trend of the resonance frequency of the tube was similar between theory and measurements. It can be seen that the number of experimental data was enough to compare the theoretical predictions.

Figure 4.3 shows the acoustic pressure fields of the tube at the first four harmonic frequencies. The voltage of acoustic signal was fixed at 5V. The measure point was in the centre of the tube and starts from $y_0\ to\ y_2$ in increments of 20 mm. In the right hand side of the figure where the upper end of the tube is, the pressure is assumed as zero in the theoretical. Yet the pressure is much higher in the real situations. Moreover, due to the pyramidal structure in the lower half of tube, the pressure is smaller in the left hand side of the figure. In general, the result shows a good agreement between the measurements and the theoretical predictions. The trend of frequency response alone the tube was similar between two figures. The pressure node and anti-node regions were also matched well. However, due to the pressure drop loss, friction loss and acoustic streaming effect, the pressure at the node regions and the upper end of the tube are not zero in the experimental data.

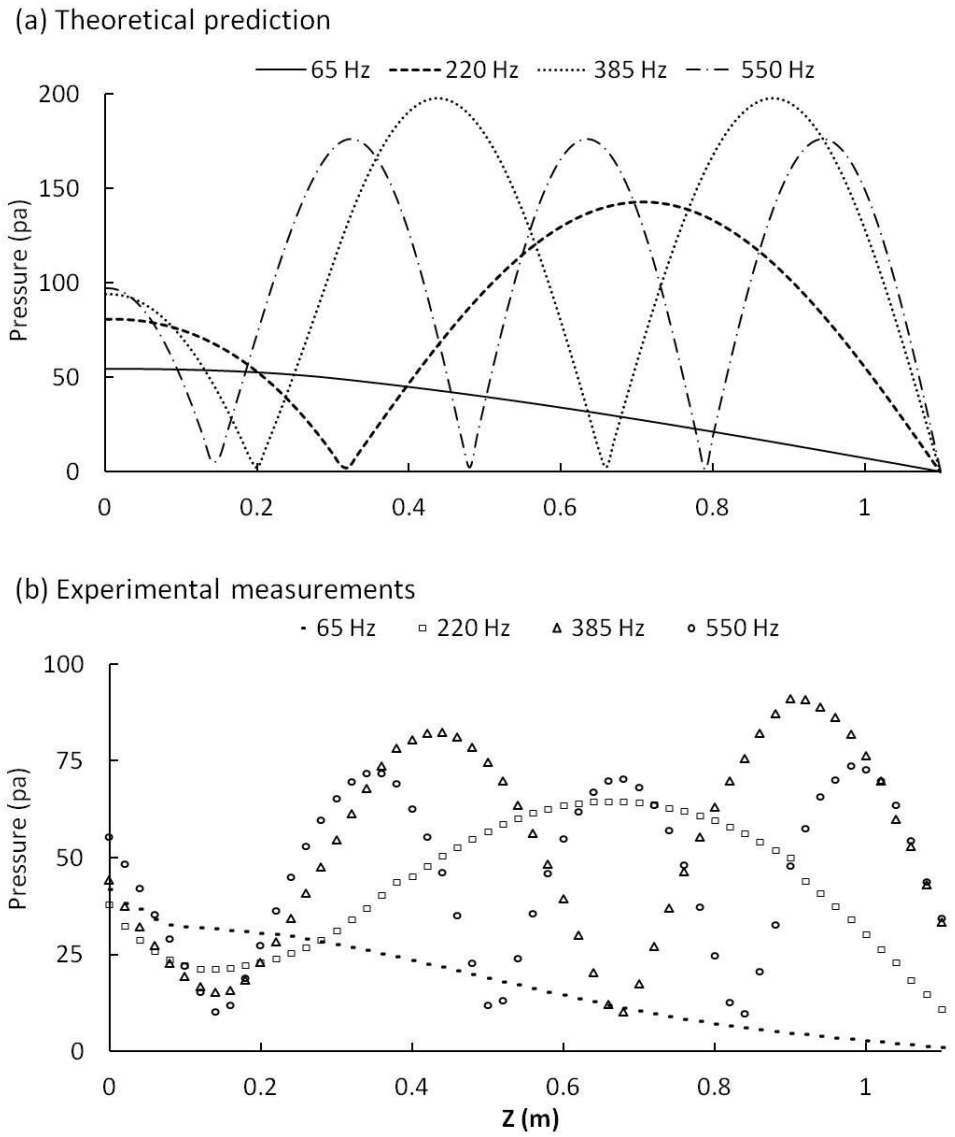

Figure 4.3: The acoustic pressure fields of the tube at the first four harmonic frequencies. (a) Theoretical prediction, (b) Experimental measurements.

The acoustic velocity fields of the tube at the first four harmonic frequencies are illustrated in Fig. 4.4. The velocity data is not smooth at Z = 0.3 m, which is in the upper end of pyramidal structure. This proves that the acoustic fields are very sensitive to the change of the shape. In order to understand more about the acoustic fields in the tube, the detail velocity fields will further discuss in the section 5.1. The comparison between theoretical prediction and experimental

measurement will also be included. However, to simplify the experimental data and get the clearer observation, third harmonic frequency (385 Hz), which the wavelength is fitted the observable area of the tube (Z = 0.3 to 1 m), are chosen as main test frequency (see Fig. 5.1.).

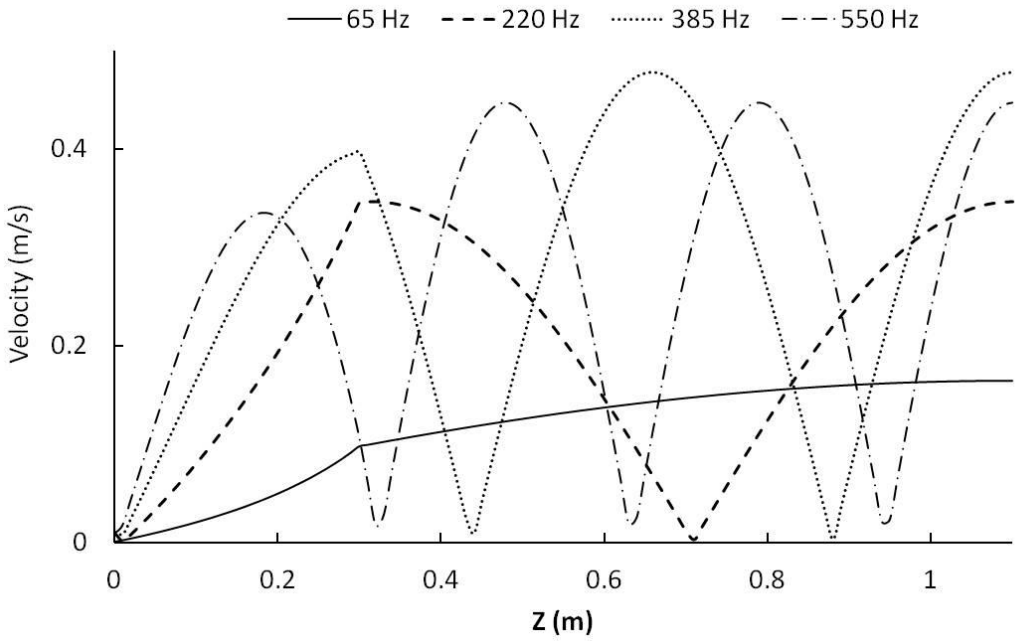

Figure 4.4: The theoretical measurements of the acoustic velocity fields of the tube at the first four harmonic frequencies.

4.2 Selection of Seeding Particles

The quality of a PIV image is mainly determined by the type of tracer particles. Titanium dioxide (TiO_2), aluminium oxide (Al_2O_3), hollow glass balls and glycerol smoke were tested in this experiment. The properties of these seeding particles are shown in Table 4.1. The accuracy of the measured velocity field is determined by the ability of the particles to follow the instantaneous motion of the working fluid. In order to consider the gravity effect and to find the drag force of particles and the

viscosity of working fluid, the minimum flow velocity required to float the seeding particles can be calculated. According to Eq. 2-8, the lowest flow velocity to support the seeding particles are shown in Table 4.1. The results indicate that the hollow glasses have the highest settling velocity and glycerol smoke has the lowest settling velocity. In order to increase the experimental accuracy, the glycerol smoke was selected for the first test. However, it was found that the glycerol smoke easily evaporated in the hot gas surrounding the flame, as shown in Fig. 4.5. Figure 4.5(a) shows the PIV raw image without firing and both the fuel streamline and co-flow field can be seen very clearly. After ignition, as shown in Fig. 4.5(b), the glycerol smoke particles had all been evaporated by the hot gas and the flow field near the combustion areas cannot be observed. In order to prevent this phenomenon, the titanium dioxide and aluminium oxide particles were adopted instead. The settling velocities of the titanium dioxide and aluminium oxide are similar, but the titanium dioxide particles have a higher light scattering rate. Hence, the titanium dioxide particles were chosen as the main seeding particles in this study.

Table 4.1: The properties of seeding particles.

Material	**Density (kg/m^3)**	**Diameter (m)**	**Cd factor**	**Settling velocity (m/s)**
TiO_2	4200	0.000003	0.47	0.00527
Al_2O_3	4000	0.000003	0.47	0.00527
Glass(hollow)	1050	0.00001	0.47	0.01667
Glycerol Smoke	1261	0.0000005	0.47	0.00373

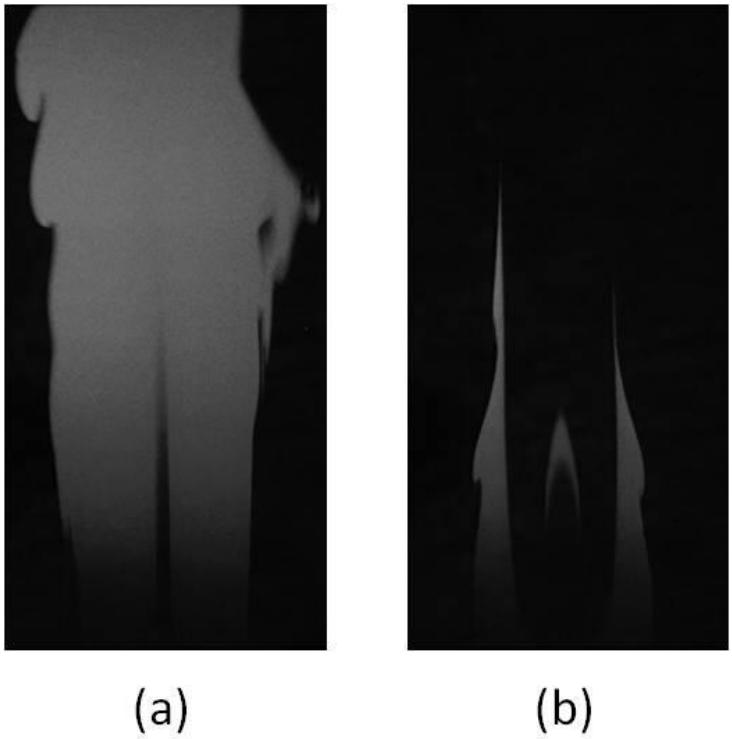

Figure 4.5: PIV raw images of co-flow flames, (a): without firing, (b): after ignition. (Co-flow air seeded by glycerol oil smoke).

4.3 PIV Seeding Methods

Two seeding methods are usually adopted in combustion experiments to observe the characterisation of the flame flow. Sending the seeding particles from the fuel pipe or co-flow pipe is the most used method to provide the light scattering source. Many PIV researchers are using this seeding method, such as Papadopoulos's research group [31] and Gupta's research group [103]. In the present study, this seeding method was first adopted for the flow image capture test. The co-flow burner was used as the test rig. The results show that the particles are easily blocked in the fuel pipe due to the narrow diameter (fuel pipe = 6 mm, fuel nozzle = 4.3 mm). In the current fuel flow condition (fuel flow rate = 1 l/min), only a few

particles can come out intermittently from fuel nozzle. With such a low density and non-uniformity of particles, it is not possible to do the post-processing. Regarding the co-flow air, the seeding particles were able to come out from the co-flow nozzle when a larger air flow rate was supplied (> 9 l/min). The detailed testing results are further demonstrated in section 4.6.

Another seeding method is to inject the particles into an enclosed system. After the whole box is filled with the uniform seeding particles, the working system is switched on and the PIV images are captured. PIV experiments that have used this seeding method can be found in the research groups of Otsuka et al. [86], Yilmaz et al. [87] and Shoshin et al. [104]. The results show that the flame flow velocity and vector maps can be calculated by using this seeding method. The relatively steady seeding condition is also suitable for the observation of the low flow field. The only disadvantage of this seeding method is that the particles only fill the surrounding flow and so the flow behaviour in the combustion reaction zone, which is above the nozzle exit, is difficult to measure accurately. In this study, the characteristics of flame behaviour and effects of the acoustic excitation in the surrounding air need to be measured. However, since the seeding particles are difficult to deliver from the tiny fuel nozzle (the nozzle diameter of the main test is 1.8 mm) and acoustic wave motion is relatively low, seeding in the whole test tube was chosen in the present experiment.

4.4 Signal Synchronisation System

Taking the Phase-locked image is important in order to know the phase angle of the oscillation image. In order to observe the flame flow at a certain acoustic wave phase angle, the trigger timing for all of the relative instruments have to be synchronised. An electronic circuit, used to generate a trigger signal to the loudspeaker, high speed camera and PIV system, was developed. The trigger timing between certain acoustic wave phase angles and output trigger signals were synchronised and adjusted by the LabVIEW software and NI-DAQmx system. In this study, the functions that send a synchronised signal to loudspeaker and PIV system were edited by a LabVIEW vi diagram. The vi front panel is shown in Fig. 4.6. The frequency of the acoustic signal can be adjusted by the “Frequency” icon. The phase angle can be defined by keying-in the phase angle in the “Phase (degree)” column. The delay timing between the acoustic phase angle and the output trigger signal can be controlled by the “Freq multiple” function. The “Acoustic” icon is for switching on the function that starts to send the signal to the loudspeaker. After setting the phase angle to trigger the high speed camera system, the “timing and synchronisation” function in LabVIEW will then synchronise the trigger signals to send them at the same time. The phase can be adjusted from 0 to 2π and covers the whole period of the excitation waveform.

Figure 4.7 shows the triggering sequence of the synchronisation signals. The trigger timing depends on the given acoustic signal. Firstly, the frequency and phase angle have to be inputted into the synchronisation program. Then the frequency sine wave signal will be sent to the loudspeaker. After the sine wave reaches the given phase angle, a trigger signal will be sent out to the PIV system. (An example at the phase angle of 90° is shown in the dash line of Fig. 4.7.) However, at high frequency, the velocity of the acoustic flow is much higher than the highest PIV laser pulse which is only 7.25 Hz. A signal delay function was designed in this program to solve this problem. For example, at 75 Hz, a 20 times delay is set, the trigger signal will only be sent out every 20 acoustic cycles which is 3.75 Hz. Therefore, the PIV camera can be synchronised to catch images in any excitation frequencies and at each phase angle.

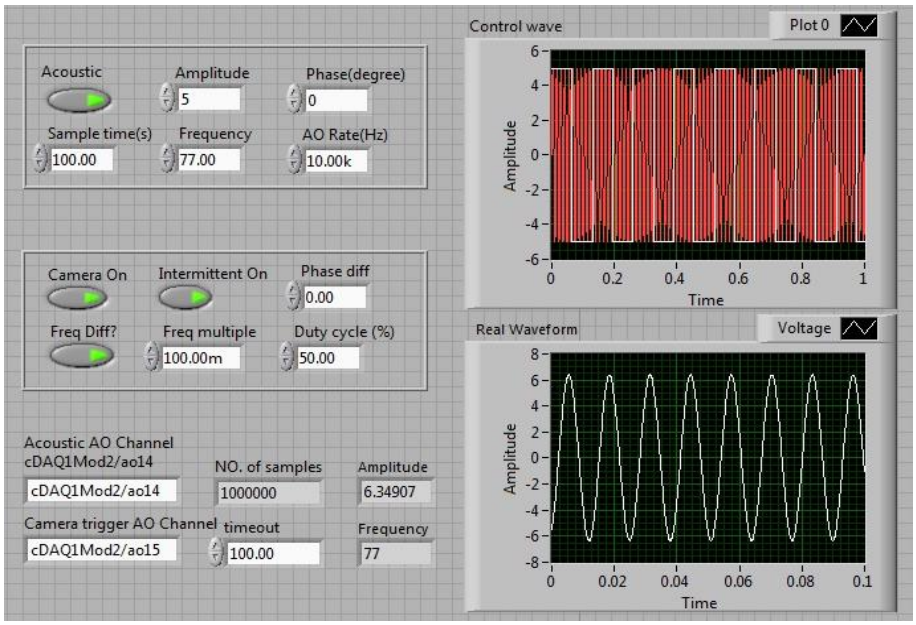

Figure 4.6: LabVIEW vi front panel for the synchronisation function.

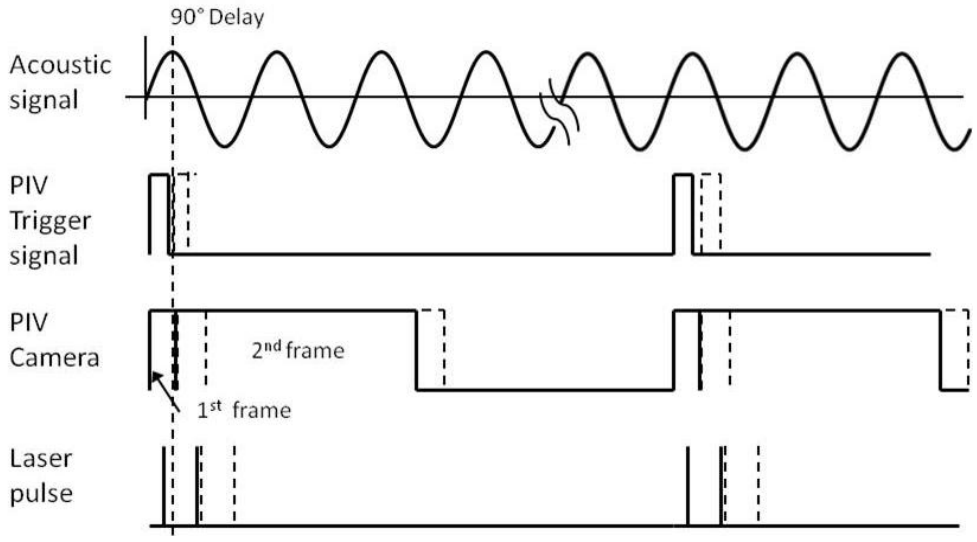

Figure 4.7: The triggering sequence of synchronisation system. (Dash line is an example of 90° delay.)

Due to some potential errors such as the delay of acoustic signal and the acoustic streaming effect, the velocity data may vary in each excitation cycle and phase angle at the same excitation frequency. In order to know the accuracy of synchronisation system in the present experimental system, a simple test between the NI-DAQ card output signal and the high speed camera recording timing were performed. The test is divided into cold acoustic excitation case and hot flame gas case. Figure 4.8 is the phase-locked velocity data at an excitation frequency of 385 Hz. The data was captured at Z = 400 mm in the centre of the tube, and every 36 degrees and a 100 times delay was adopted in each phase angle. The measured phase-resolved velocity data remained similar over 1,000 acoustic cycles. The largest velocity difference is calculated in the value of 2.8 %.

For the case of hot flame gas, a sequence of direct flame images and flame heights at an excitation frequency of 10 Hz is shown in Fig 4.9. The data was captured at every 10 degrees and a 10 times delay was adopted in each phase angle. The flames have the same pattern at certain phase angles and the pattern repeats for eight hundred excitation cycles. The measured flame height indicates that the flame patterns are remained the same at phase angles of 280° to 360° and 0° to 30° over eight hundred excitation cycles. The largest difference is observed at a phase angle of 210° and the difference is 4.4 %.

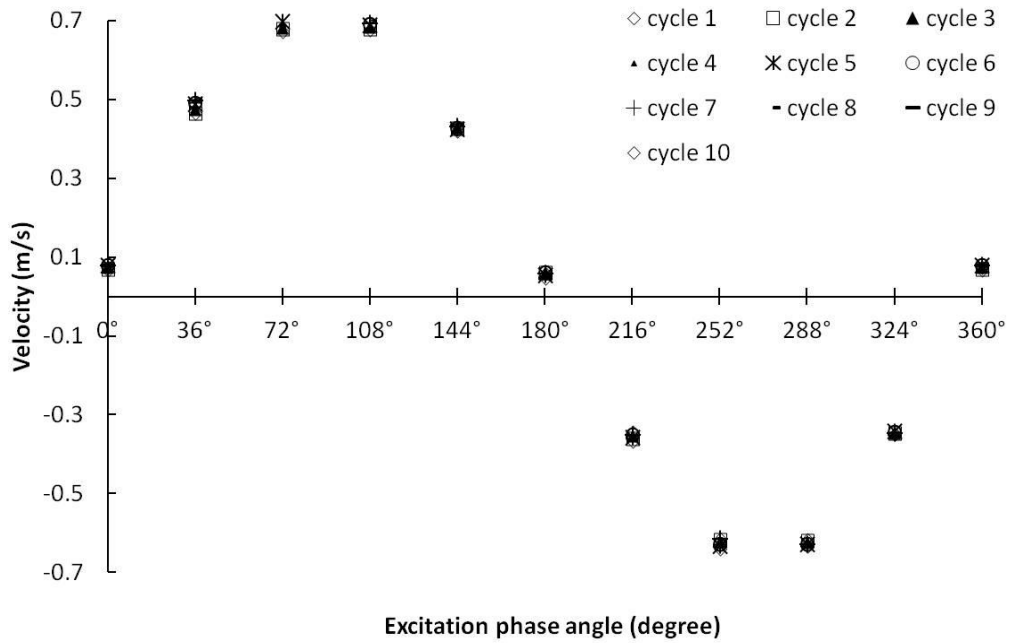

Figure 4.8: Phase-locked acoustic velocity data in the excitation frequency of 385 Hz. The data were captured in every 36 degree with 100 times' delay.

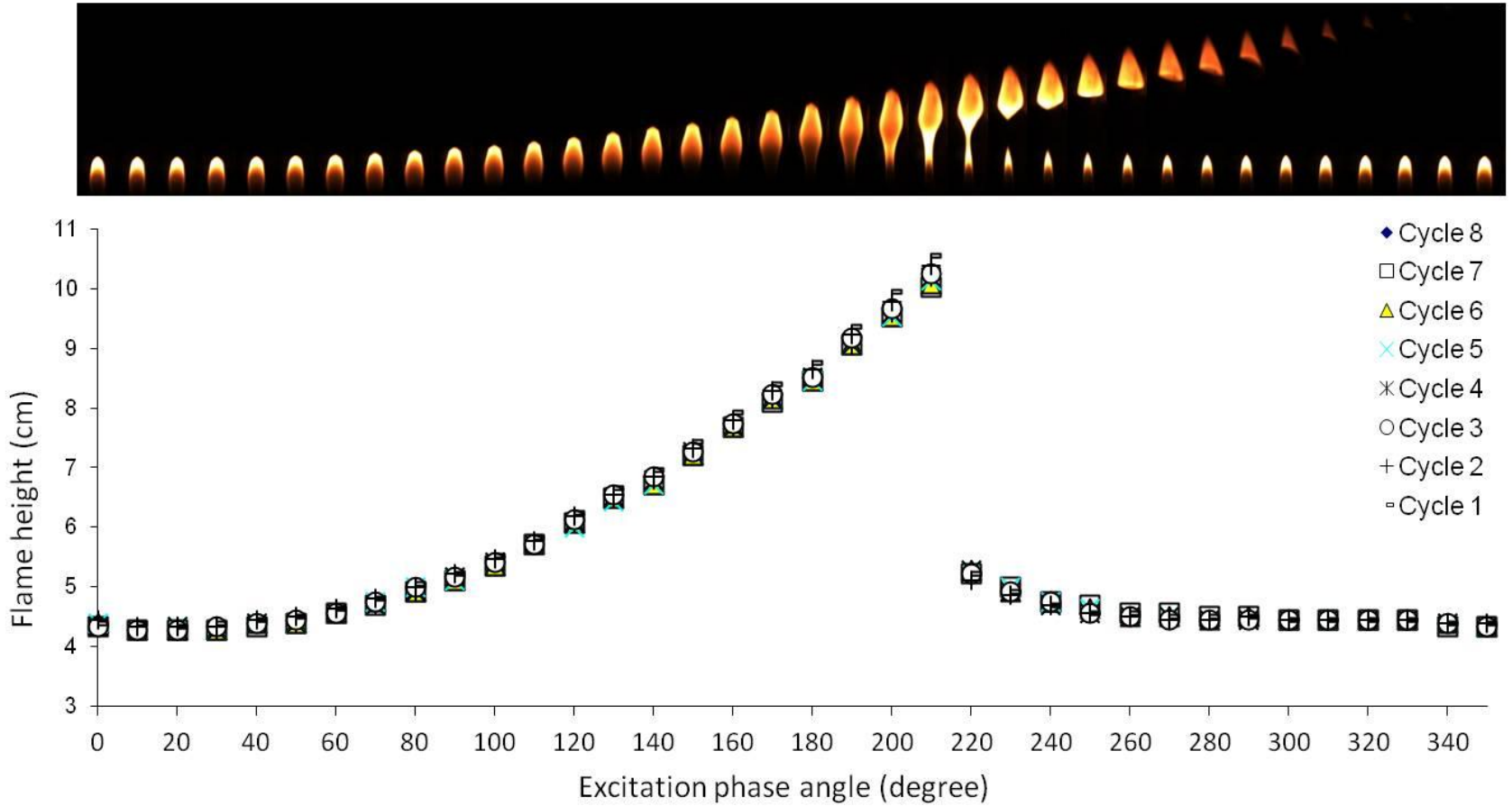

Figure 4.9: Flame direct images and flame heights in the excitation frequency of 10 Hz. The data were captured in every 10 degree with 10 times' delay in each phase angle and 8 excitation cycles were recorded.

4.5 Statistical Analysis of the PIV Data

4.5.1 Instantaneous PIV data

The instantaneous PIV results are often used to measure and analysis the magnitudes of the local velocity and vector fields in the research area of combustion instability [43, 105-107]. Demare and Baillot [43] presented the flow characterisations of lifted diffusion flame under acoustic excitation by using classical instantaneous PIV measurements. The flame flow behaviour and the instantaneous velocity fields were analysed. The results proved that the acoustic excitation can provide premixing and enhance the combustion. Muniz and Mungal [107] used PIV to provide instantaneous, two-dimensional velocity fields in the region of the lifted flame base to study the stabilisation characterisation of methane and ethylene flame. The result showed that the fluid velocity in the flame base is three times less than the laminar flame speed. Ji and Gore [106] also took instantaneous PIV data to study the flow structure in lean premixed swirling combustion and compared the averaging data. They argued that the highest velocity magnitudes in the instantaneous velocity fields are much larger than those in the mean velocity fields. In the mean velocity fields, only a single large recirculation zone can be observed. Multiple smaller recirculation zones, which are usually predominant in the flames, can only be observed in the instantaneous velocity fields. At some locations, there are sudden increases in the velocity magnitude in the instantaneous velocity fields, which are not found in the mean velocity fields. Therefore the instantaneous PIV images are more suitable for study

the detail velocity fields in combustion area. The phase-locked instantaneous PIV data was applied to measure and calculate the characterisation of flame flow under external excitation.

4.5.2 Ensemble Averaged PIV data

To study the overall flow velocity field and turbulence statistics, averaging a large number of vector maps is another PIV statistic method. The number of instantaneous images is important to get a reliable ensemble averaged flow characteristic. Papadopoulos [31] used ensemble averaging PIV results to observe the characterisation of flame flickering structure. The frame number of 72 was used to statistic the phase-resolved velocity fields. Zhou et al. [108] studied the Vorticity distribution in a buoyant diffusion flame using averaged PIV results. Agreement between mean velocities from the first 50 and the last 50 images showed that 100 images yield statistically converged data. Mao and Jaworski [109] used the classical Reynolds decomposition to calculate the frame number to study the turbulence characteristics of acoustic flow velocity fields in a thermoacoustic devices. The result showed that the 100 frames are judged sufficient to obtain a good representation of the flow over the whole flow field, and a reasonable representative of the convergent statistics. In the present study, the same methodology was applied to separate the instantaneous flow fields into mean flow field to estimate the number of instantaneous frames. Based on the assumption, the mean velocity fields are the same at any time corresponding to the same phase in one acoustic cycle. The corresponding mean velocities $U(x, y, \varphi)$ and $V(x, y, \varphi)$,

and the RMS values of the velocity fluctuations $u'(x, y, \varphi)$and $v'(x, y, \varphi)$ can be calculated by the following equations [109, 110]:

$$U(x, y, \varphi) = \frac{1}{N}\sum_{i=1}^{N} u(x, y, \varphi, i), \qquad (4-33)$$

$$V(x, y, \varphi) = \frac{1}{N}\sum_{i=1}^{N} v(x, y, \varphi, i), \qquad (4-34)$$

$$u'(x, y, \varphi) = \sqrt{\frac{1}{N}\sum_{i=1}^{N} [u(x, y, \varphi, i) - U(x, y, \varphi)]^2}, \qquad (4-35)$$

$$v'(x, y, \varphi) = \sqrt{\frac{1}{N}\sum_{i=1}^{N} [v(x, y, \varphi, i) - V(x, y, \varphi)]^2}. \qquad (4-36)$$

where the summation is over $i = 1,2,3 \ldots \ldots, N$ images taken at phase φ.

The convergence of the ensemble averaged PIV data is checked by plotting the variation of averaged flow quantities with number of samples at a certain location in the flow field. In the present study, the fixed phase angle of 1000 instantaneous PIV images taken at Z = 600 mm of centre of the tube has been applied to gather the statistic data. The result in Fig. 4.10 illustrates the mean velocity and the rms values of the velocity oscillations are converging to a constant value at around 120 images. Hence the sample number for ensemble averaging PIV data was set at 120 images in the later analysis.

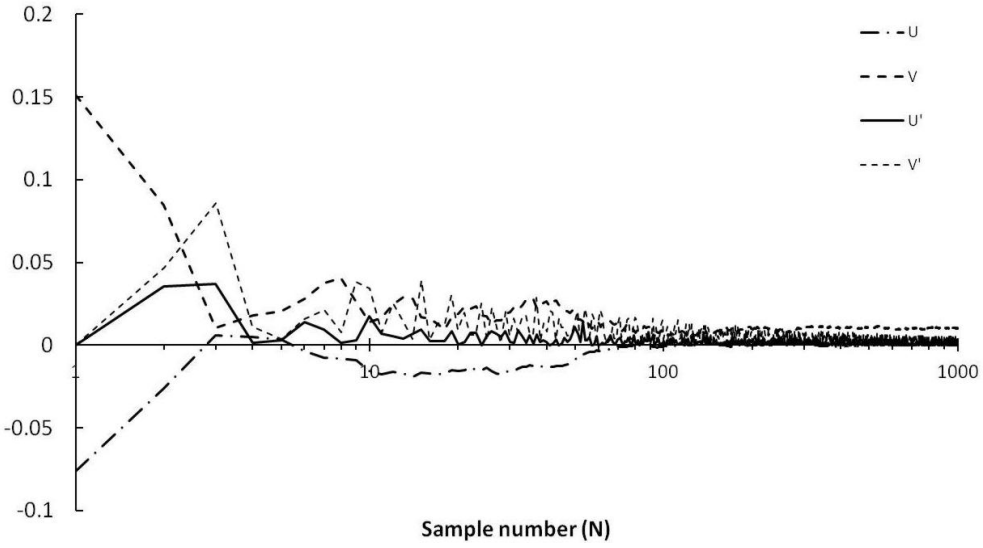

Figure 4.10: Effect of number of instantaneous measurements on the computation of the flow statistics. The data is taken at nozzle position C and at excitation phase angle of 0 degree.

4.6 Demonstration of PIV Test Results Using the Co-Flow Burner

4.6.1 Co-Flow Burner and PIV Experimental System

The co-flow burner has a central fuel tube with a 4.3 mm diameter, surrounded by a 43 mm diameter air annulus. The air chamber was filled with glass beads and a honeycomb to obtain uniform flow velocity across the air annulus exit. The sectional drawing of the co-flow burner is shown in Fig. 4.11. The fuel flow rates and co-flow air flow rates were measured and controlled by digital mass flow controllers. An AALBORG GFC 17 mass flow controller was used for the fuel gas and an AALBORG GFC 37 mass flow controller was used for the co-flow air. Both controllers were connected with the LabVIEW system so that the flow rates could be adjusted. The test conditions of the experiment are shown in Table 4.2. The fuel

flow rate was set at 0.4 l/min. The coflow air flow rate was varied from 10 l/min to 40 l/min. Figure 4.12 shows the experimental system, which consisted of a co-flow burner and flow controllers, and the PIV system.

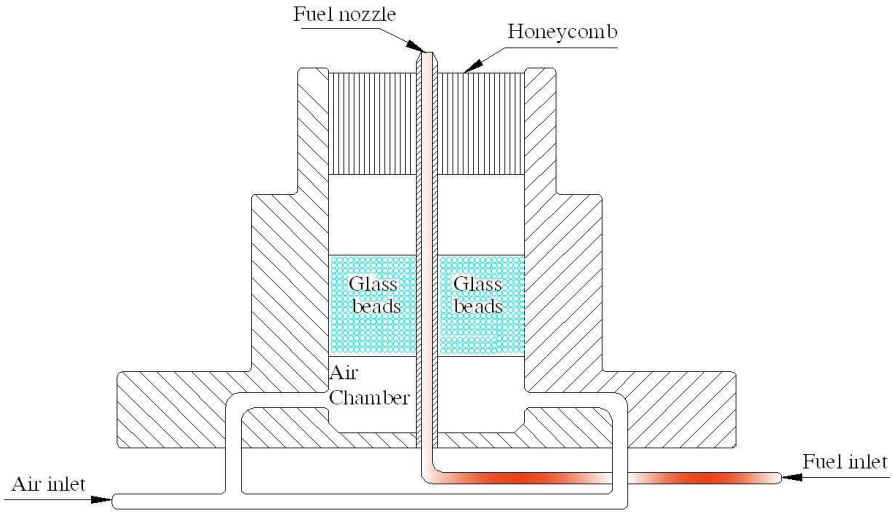

Figure 4.11: A sectional drawing of the co-flow burner.

Table 4.2: The test conditions of the flows.

	Flow rate (l/min)	Nozzle d(m)	Density (kg/m^3)	Viscosity ($N.s/m^2$)	Velocity (m/s)	Re
Fuel	0.4	0.003	0.717	1.34E-05	0.943	151
Co-flow Air	10	0.04	1.2	1.80E-05	0.133	354
	20	0.04	1.2	1.80E-05	0.265	707
	30	0.04	1.2	1.80E-05	0.398	1061
	40	0.04	1.2	1.80E-05	0.531	1415

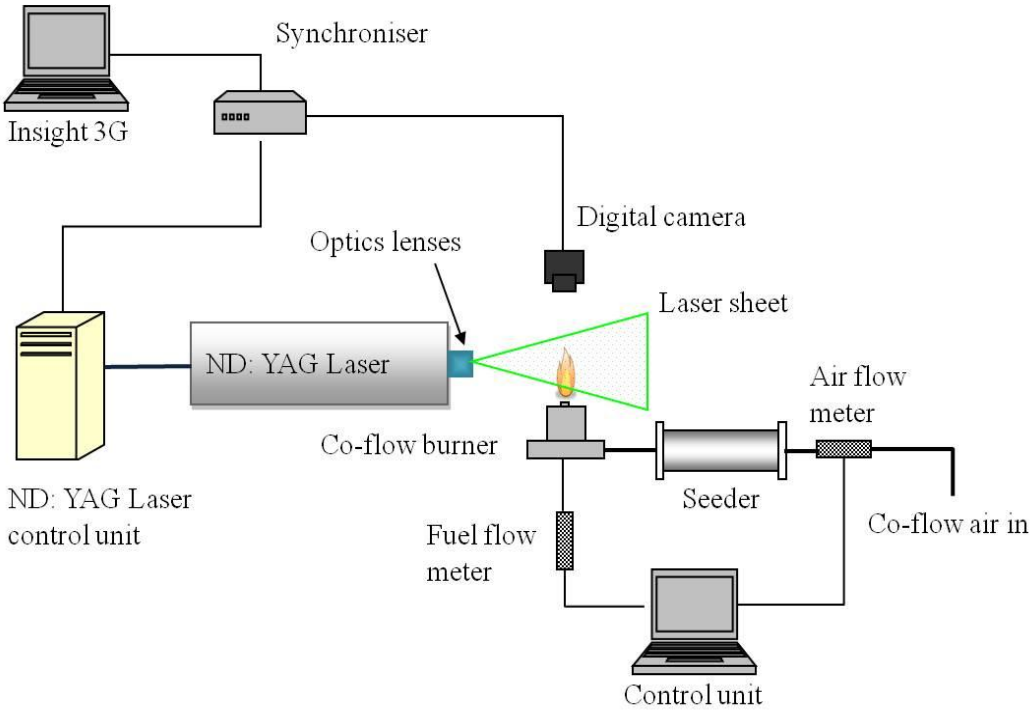

Figure 4.12: PIV experiment system for co-flow burner.

4.6.2 Seeding from the Fuel Nozzle

Figure 4.13 illustrates the PIV raw images that were seeded from fuel pipe. The time interval was 7.25 Hz and the premixed fuel flow rate was 7 l/min (with 1 l/min fuel and 6 l/min air). The results show that the concentration of seeded fuel flow fluctuates in each image. This is because the particles are easily blocked in the narrow pipe and junctions. This blockage may cause the rise of flow pressure. After the pressure reaches a limit value, the particles are ejected from nozzle suddenly. Reliable experimentation is impossible due to this uncertain factor. The nozzle diameter of the main experimental rig is even smaller than this test rig; hence seeding from fuel nozzle is not suitable for the present experiment.

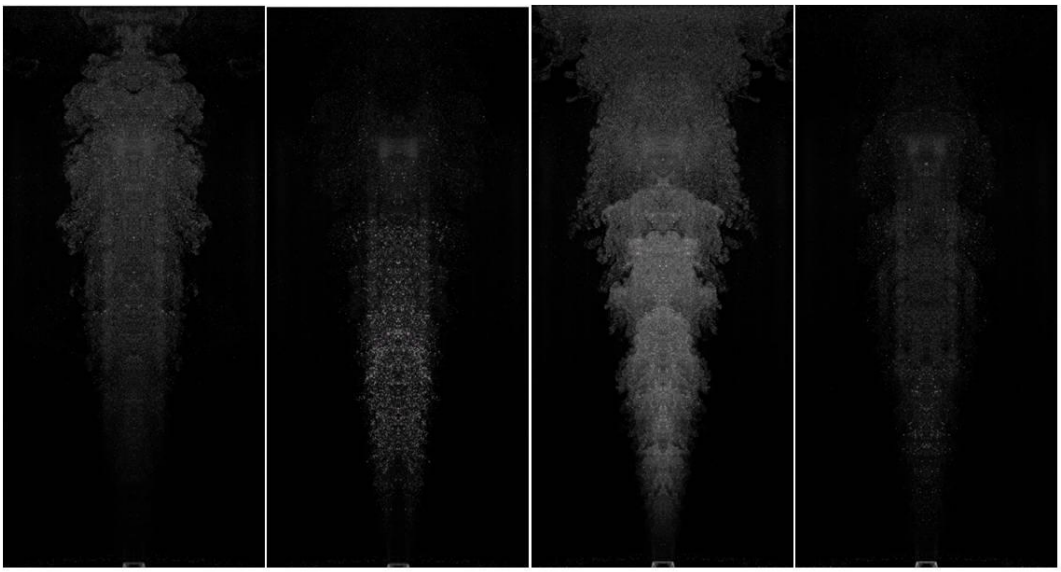

Figure 4.13: A sequence of PIV raw images with seeded premixed flow rate of 7 l/min.

4.6.3 Seeding from the Co-Flow Nozzle

Figure 4.14 was generated from a sequence of co-flow flame images with a fuel flow rate of 0.4 l/min, and a co-flow rate of 10 l/min, with a time interval of 7.25 Hz. The flame position can be seen in these images and also the periodic and reproducible oscillating characteristics of the vortices are shown clearly. Although the lower frame rate of the camera could not completely record the flickering features of the flame, the characteristics of the flame evolution, expansion and part quenching by the outer vortices could still be seen clearly. The results prove that uniform seeding particles can come out from co-flow nozzle stably and reliably.

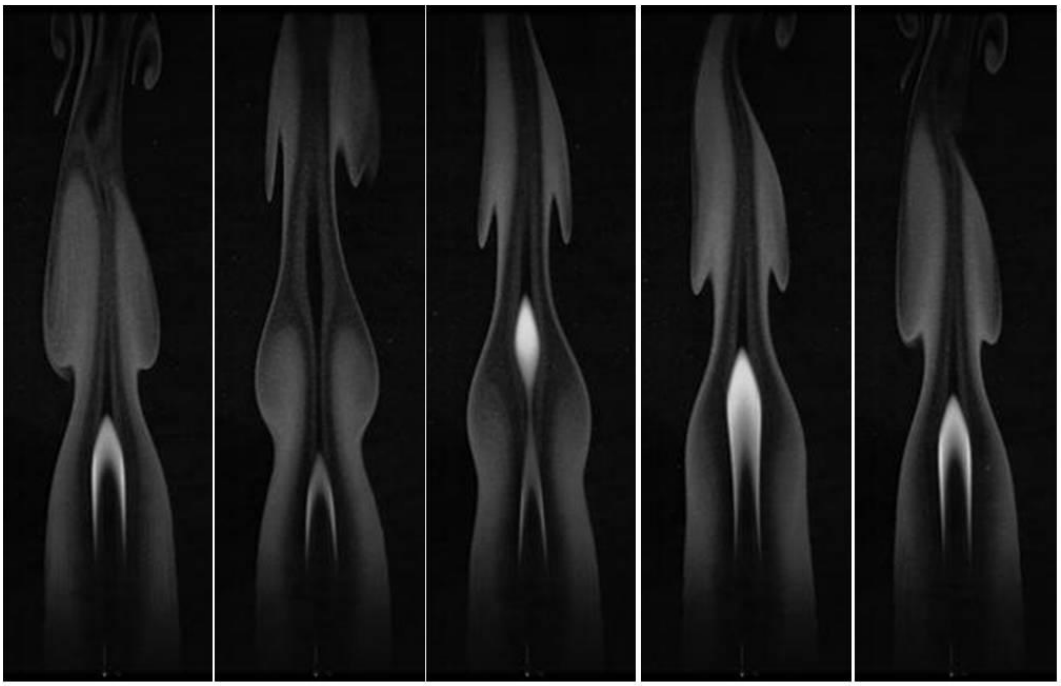

Figure 4.14: PIV raw images of co-flow flames with fuel flow rate = 0.4 l/min and co-flow rate = 10 l/min. The co-flow air was seeded by TiO_2.

With a further increasing of the air co-flow rate to 20 l/min, as shown in Fig. 4.15 (A)-b, the co-flow air becomes strong enough to suppress the flame flickering; therefore, the flame becomes laminar and stable. After the air flow rate is raised to 30 l/min, as shown in Fig. 4.15 (A)-c, roll up vortices are generated at the outer boundary of the co-flow air, due to the increase of shear stress between co-flow air and the surrounding air. Furthermore, after the air flow rate increases to 40 l/min, the roll up vortices is even stronger, as shown in Fig. 4.15 (A)-d. The results prove that the flow structure affected by the co-flow air can be observed by this seeding method. The velocity vector maps and vorticity contours shown in Fig. 4.15 (B)

further demonstrate that this concentration of seeding particles can be used by the PIV processing function.

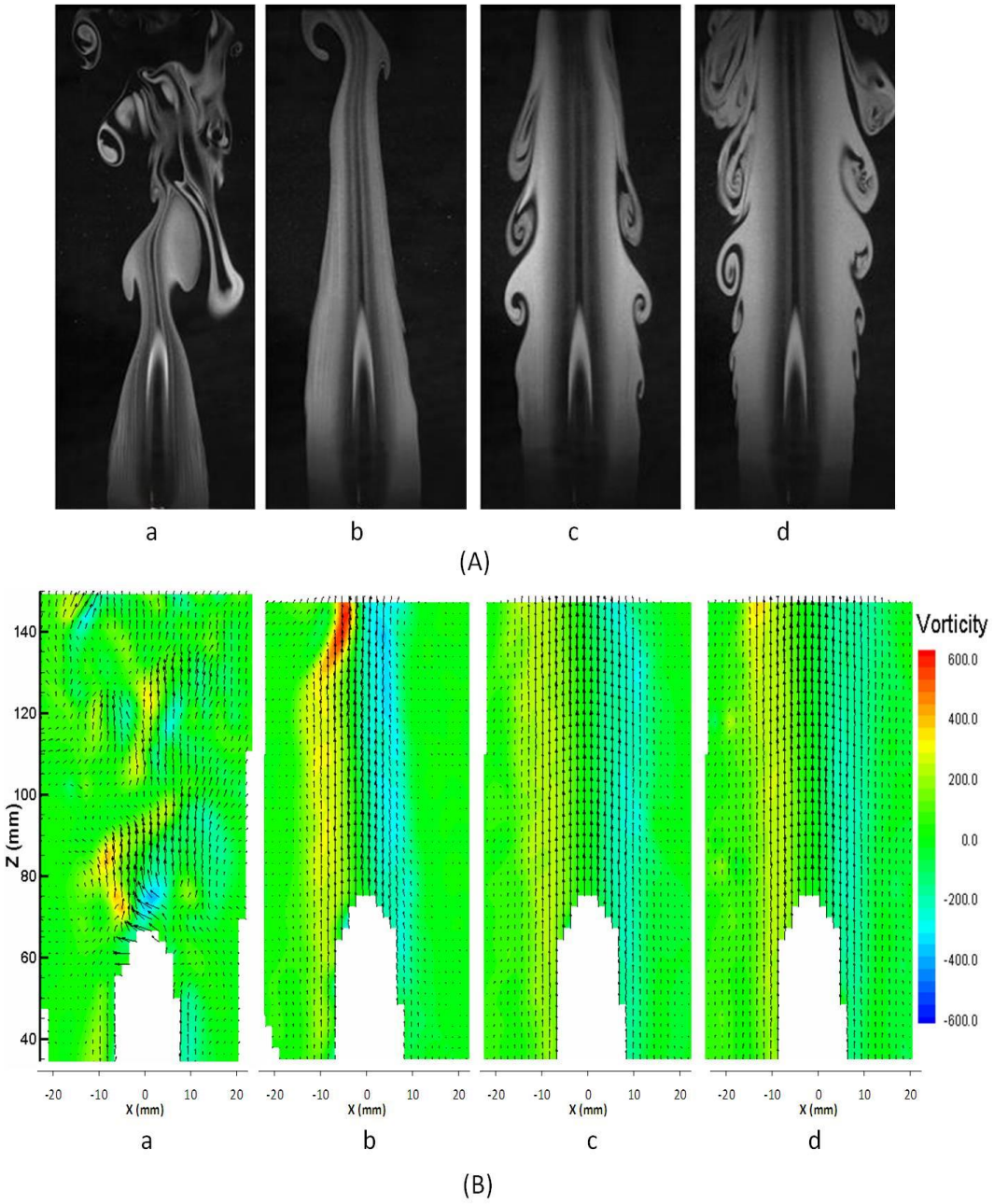

Figure 4.15: (A) PIV raw images of co-flow flames, (B) The vector maps and vorticity contours of co-flow flames with fuel flow rate = 0.4 l/min and different co-flow air flow rates; a: Co-flow rate = 10 l/min, b: Co-flow rate = 20 l/min, c: Co-flow rate = 30 l/min, d: Co-flow rate = 40 l/min.

The abovementioned results show that the flow that is seeded from fuel pipe is impossible to adopt in this study. Seeding in the co-flow pipe is available for the combustion experiment; however, a high flow rate is needed. When such high flow rates are compared with the low acoustic energy, it is difficult to measure the variation of the air flow motion induced by acoustic excitation. Moreover, in Fig. 4.15 (B), the central area near the x-axis is blank. This is because the seeding particles could not be traced effectively as only the co-flow is seeded. Therefore, the flow field near the flame area is unable to be diagnosed.

4.7 Summary

The theoretical predictions of acoustical characterisations of the square tube and their comparison to experimental results have been discussed in this chapter. Results showed that the theoretical predict harmonic frequency data match well with experimental measurement. The acoustic velocity field at first four harmonic frequencies were also calculated. The wavelength of the 3rd harmonic frequency fits the observable area of the present test rig. The velocity node and anti-node area in the tube can be clearly observed. Therefore, this frequency was chosen for further analysis in the later chapters. The preparation processes of the PIV experimental system has also presented. The design of signal synchronisation system, the selection of seeding particles, the test of seeding methods and the statistical analysis of the PIV data were introduced. A signal synchronisation system was built to synchronise the trigger timing for all of the related instruments. The titanium dioxide (TiO_2) was selected as the seeding particle for the PIV. Regarding

the seeding method, the co-flow burner was used to test the seeding method whereby the flow was seeded from the fuel pipe and the co-flow pipe. The results demonstrated that this seeding method was able to measure the flow field. However, the high flow rate required was not suitable for the measurement of the acoustically excited flow. To take into account the whole set of experimental conditions, injecting the seeding particles into the test rig as a light scattering source was chosen as the seeding method in the further study.

Chapter 5

Flow Characterisation of Diffusion Flames in a Standing Wave Tube

This chapter relates to the study of the motion of acoustic flow in a tube. A phase-locked PIV system has been applied to measure the velocity field of acoustic wave. The air motion induced by external excitation in a tube at different frequencies and phase angles have been measured and analysed. According to the theoretical modelling results, the acoustical node and anti-node regions fit the observable area of the present test rig at the external excitation frequency of 385 Hz (third harmonic frequency). Hence, the acoustic excitation frequency of 385 Hz was set as the main frequency for further analysis in order to understand the flow characteristics of a cold fuel jet flow and diffusion flames. The flow characteristics affected by the fuel nozzle position in a tube and in different acoustic phase angles were chosen as the main parameters in this study. Hydrogen flames (as well as propane flames) were also used to investigate the acoustic standing wave effect on

different fuel types. The experimental results and discussions are explicitly introduced in this chapter.

5.1 Acoustic Flow Field Induced by Standing Waves in a Tube

Figure 5.1 displays the experimental measurements of the averaged velocity profiles and theoretical predict velocity data of third harmonic frequency of the tube. The voltage amplitude of acoustic signal was set at 13.7 V (applied to all experimental at 385 Hz in this chapter). The sine-wave form can be clearly observed in the figure. The velocity field was lower in the left hand side of the tube and was not smoothed at Z = 0.3 m due to the pyramidal structure affects the acoustic wave. In the observable area, the good agreement between the experimental measurements and the theoretical predication was observed. The acoustic velocity node and anti-node regions were matched well. However, the predict velocity data at velocity anti-node region was 29.1% higher than that the experimental measurements. The trend is similar as the pressure data which has been discussed in chapter 4.1.

The data of velocity distribution is important in knowing the acoustic wave effect on the fuel jet and flame structure. In order to get more quantitative velocity data along the tube, the detail velocity fields at each phase angle and at different position of tube were measured and discussed in the following section.

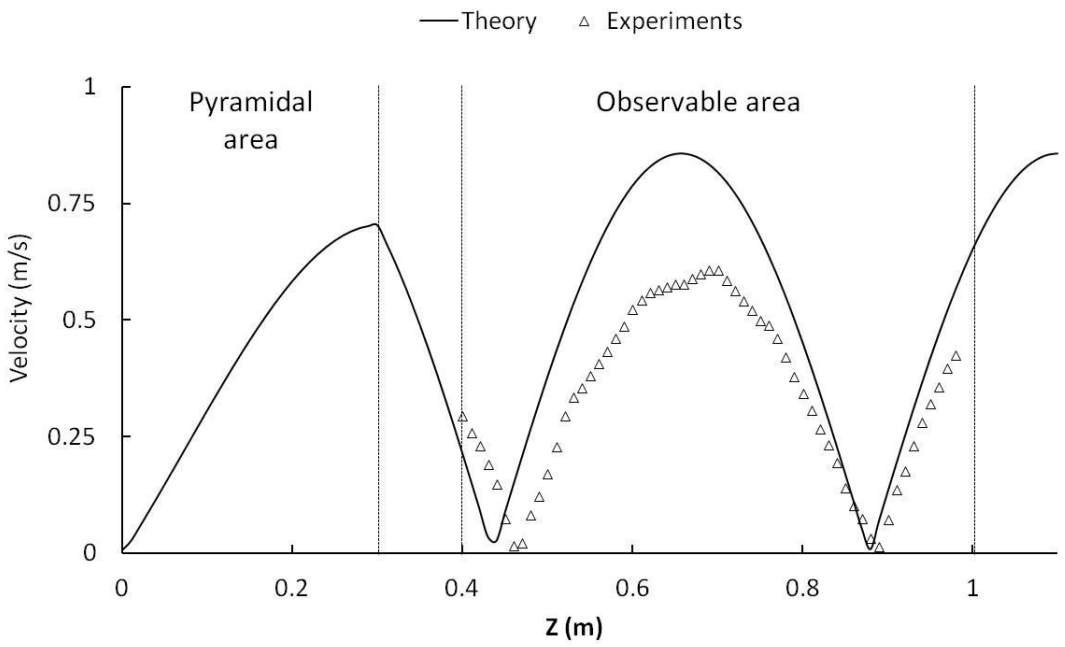

Figure 5.1: Experimental measurements of the averaged velocity profiles and theoretical predict velocity data at third harmonic frequency in the tube. (The experimental data was synthesised from 6 view fields of the PIV data).

Figure 5.2 further shows the velocity variations of different phase angles in the velocity node and anti-node regions at an excitation frequency of 385 Hz. The value is phase-resolved and 10 phase angles are presented in one ensemble excitation cycle. The maximum velocity displacement is observed in view field 4. The minimum velocity variation are found at Z = 200 mm and Z = 650 mm respectively. The velocity variations at one excitation cycle of 385 Hz at different nozzle positions are shown in Fig. 5.3. It is observed that at nozzle position B, the velocity variation can reach up to more than ± 0.7 m/s, while only up to around ± 0.1 m/s at nozzle position A. Moreover, the sine-shaped velocity variation also indicates that the air motion in the tube follows the external excitation signal.

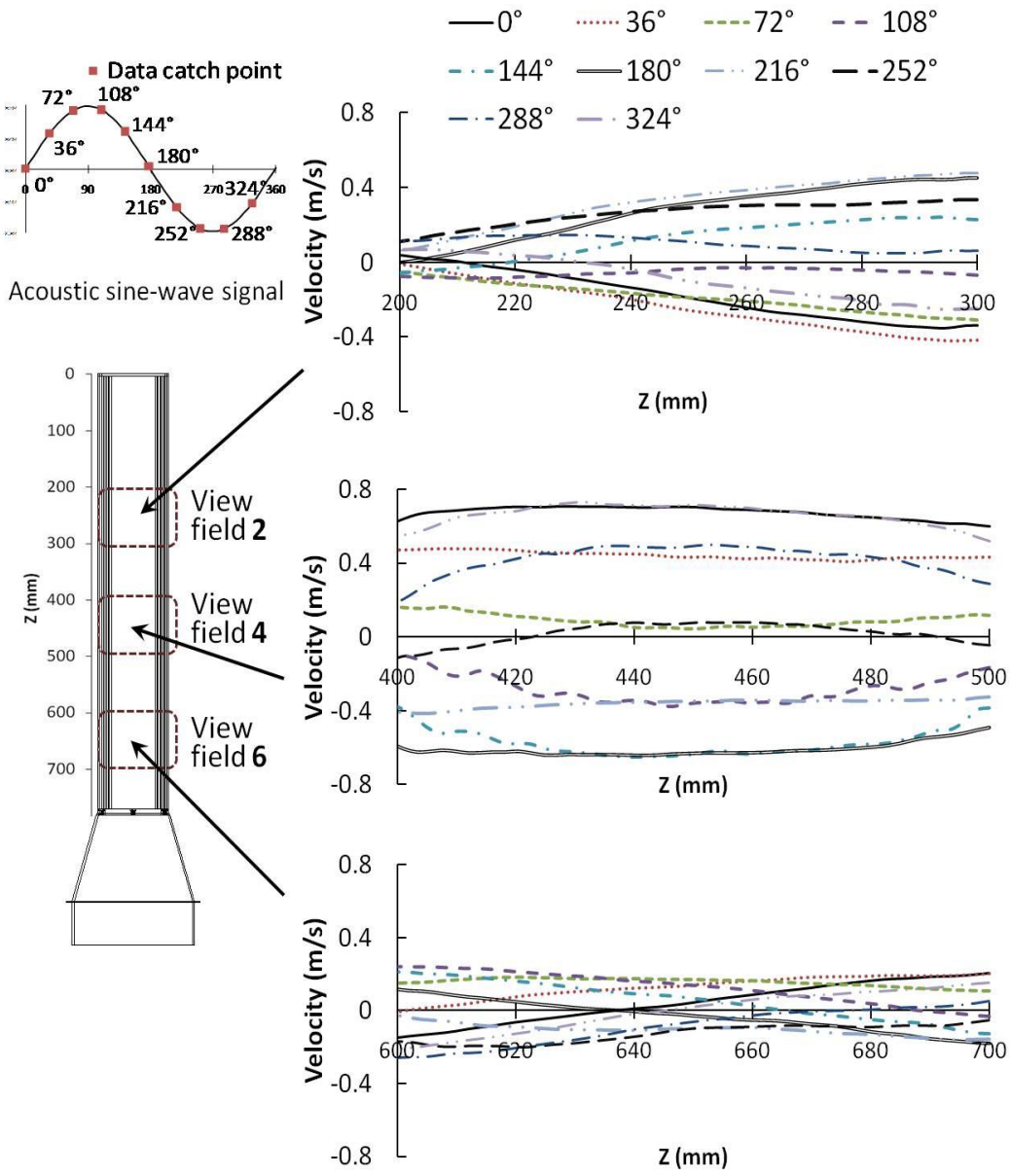

Figure 5.2: Averaged velocity profiles in view fields 2, 4 and 6 of the tube at an excitation frequency of 385 Hz (with 10 phases in one excitation cycle).

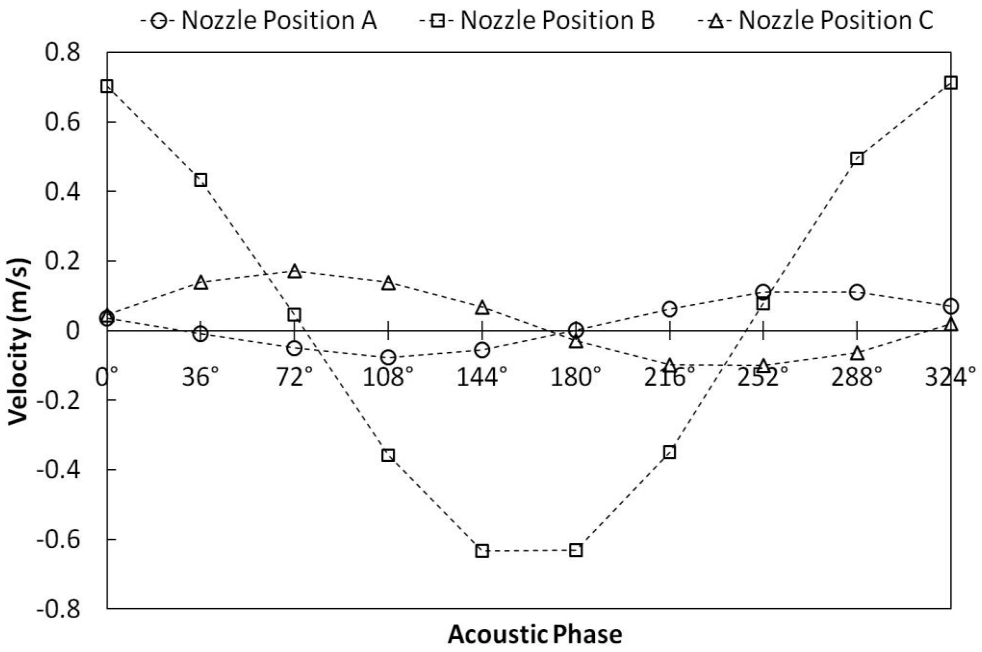

Figure 5.3: Velocity variation at nozzle positions A, B and C (refer to Fig. 3.2) in one cycle at 385Hz.

5.2 The Effect on a Cold Fuel Jet Flow

The excitation effect on a cold fuel jet flow was investigated in this section. Figure 5.4 shows the instantaneous velocity contour map and streamline plots of a cold fuel jet positioned at different locations and different acoustic phase angles. The case without external excitation is also presented as a reference, which is shown in Fig. 5.4(a). From the sub figures, it can be seen that the cold fuel jet flowed upwards with little disturbance to the jet development. Figures 5.4(b) to 5.4(d) show the flow field above the nozzle at positions A to C respectively. For figures 5.4(b) and (d), it is interesting to see that the velocity of cold flow jet reaches 0.6 m/s, which is higher than that without excitation at the phase angle of 72°. This is

because the upward acoustic flow helps to increase the velocity of the cold jet. At acoustic phase angles of 216° and 288°, the acoustic flow turns downward. Therefore, the cold jet is decelerated by the acoustic excitation. In these cases, the upward cold jet flow is still observable on the contour maps. Figure 5.4(c) shows that the upward cold jet flow has totally disappeared above nozzle position B. It is obvious that the acoustic flow velocity in this area is higher than the velocity of the cold fuel jet. The data in Fig. 5.3 indicates that the highest velocity oscillation of acoustic flow above nozzle position B can be as high as ±0.7 m/s. This is more than twice as high as the initial velocity of the cold fuel jet, which is less than 0.32 m/s. Hence, the acoustic wave has completely overshadowed the fuel jet. It is also interesting to note that the flow has changed direction from upward to downward at different phase angles for the three test sections, which means that fresh air can be drawn from the top of the tube and it takes time for the flow to reach the lower section of the tube.

The initial cold fuel flow velocity magnitude is shown in Fig. 5.5. It is clear that the velocity variation of the cold jet follows the sine wave signal. In the acoustic anti-node region (nozzle position B), the fuel flow fluctuation was much higher than that in the acoustic node region (nozzle positions A and C). Very strong negative fuel flow velocity was measured in nozzle position B. It can be seen that the fuel is pushed back into the nozzle.

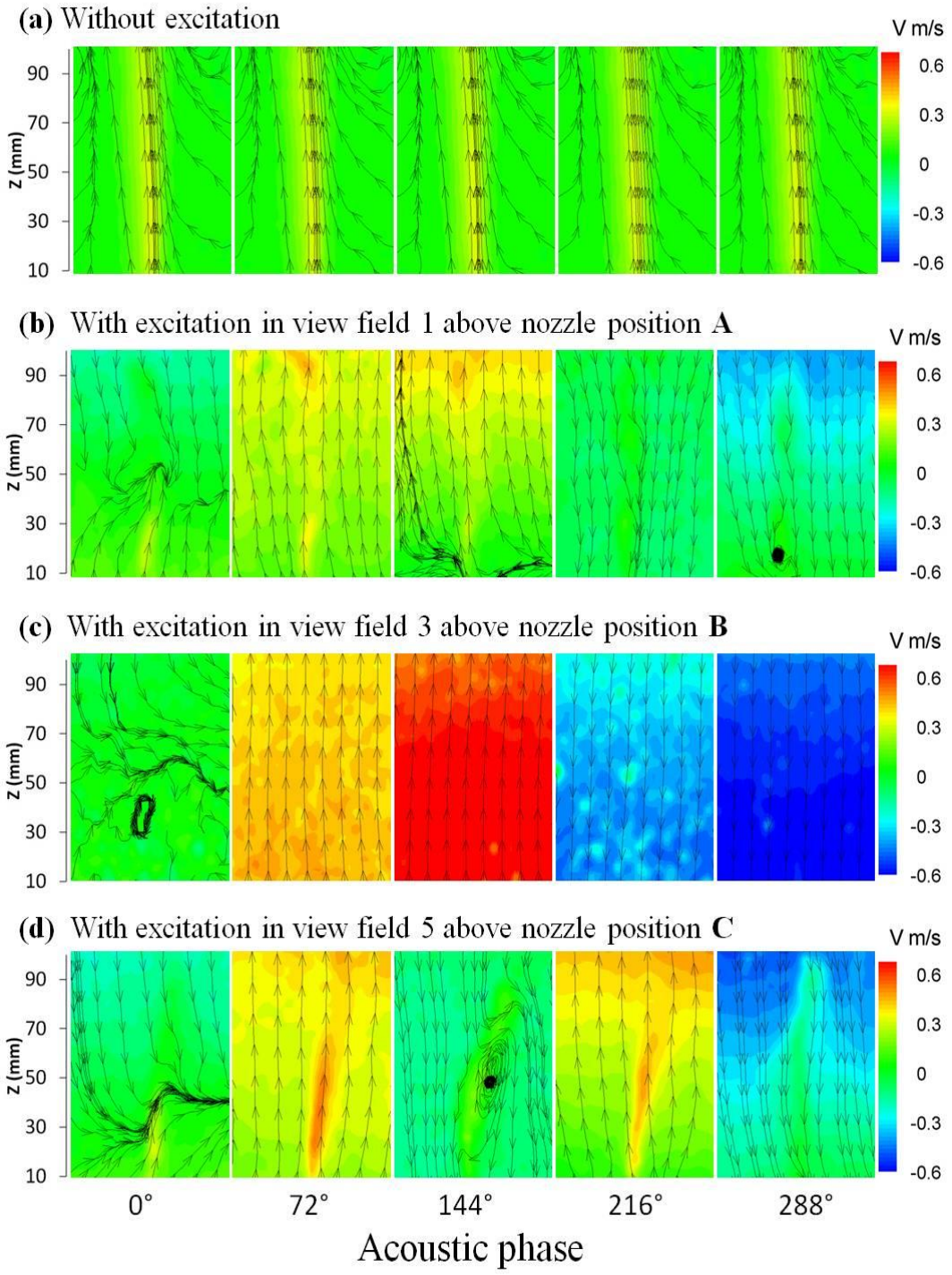

Figure 5.4: Velocity contour and streamline plots of instantaneous cold fuel jet flow. (a) Without acoustic excitation (frame rate = 7.25 fps) and (b, c and d) With acoustic excitation at 385 Hz in view fields 1, 3 and 5 (see Fig. 3.2.). Notice the change of flow direction from upwards to downwards is at 216° for positions A and B while for position C it is at 288°.

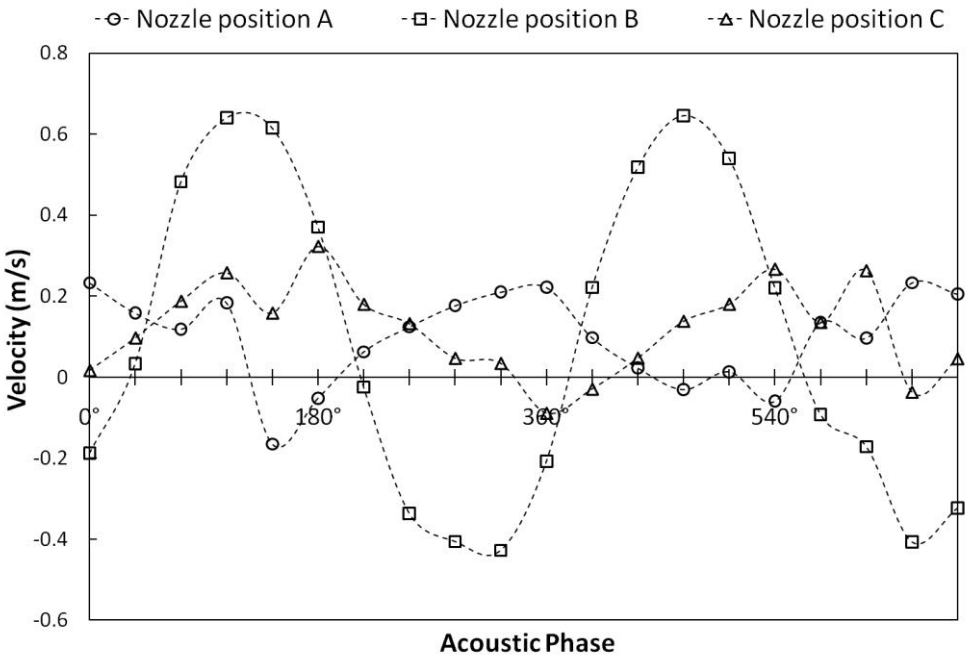

Figure 5.5: Velocity magnitude of cold fuel flow at 3 mm above the nozzle exit at excitation frequency of 385 Hz. The initial fuel flow rate was set at 55 ml/min.

5.3 The Effect on Flame Dynamics

As mentioned in chapter 4, the wavelength of the third harmonic frequency fits the observable area of the present test rig. The acoustic velocity node and anti-node regions in the tube can be clearly measured. Therefore, this frequency was chosen for further analysis. A two-dimensional velocity vector map in the tube at the third harmonic frequency (385 Hz) is shown in Fig. 5.6(a). The velocity profiles were taken at an acoustic phase angle of 0°. The view fields were from Z = 100 mm to Z = 700 mm (to Z = 600 mm in the case with flame). The velocity variation of the air particles in the tube is observed clearly in the figure. From the lower to upper

regions, the velocity magnitude increases from zero to the maximum in the middle area (Z = 400 mm) and then decreases again to zero in the upper area (Z = 200 mm). Figure 5.6(b) shows the velocity map of the diffusion flame under acoustic excitation at a phase angle of 0°. Figure 5.6(c) shows the same flame jet in the tube without acoustic excitation. It can be seen that the regular acoustic field is distorted to turbulent structure by the flame and also the acoustic excitation has a significant effect on the flame structure.

Figure 5.7 shows the velocity magnitude at 40 mm above the nozzle exit. Under external excitation, the maximum velocity displacement in the cold fuel flow case is around 0.5 m/s and that of flame jet without acoustic excitation is around 1.47 m/s. However, the maximum velocity displacement rises to more than 3 m/s with acoustic excitation. The velocity curve line also shows that the sub-harmonic behaviour can be induced in this case. It can be seen that when the downward acoustic flow pushes the fuel jet back into the nozzle, the motion of fuel jet is not only in the axial direction but also in the radial direction. In the case of the flame is attached to this jet, the asymmetric radial flow motion leads to a strong hysteresis and generates the sub-harmonic behaviour. The similar phenomenon is also observed by Demare and Baillot's group [42, 43].

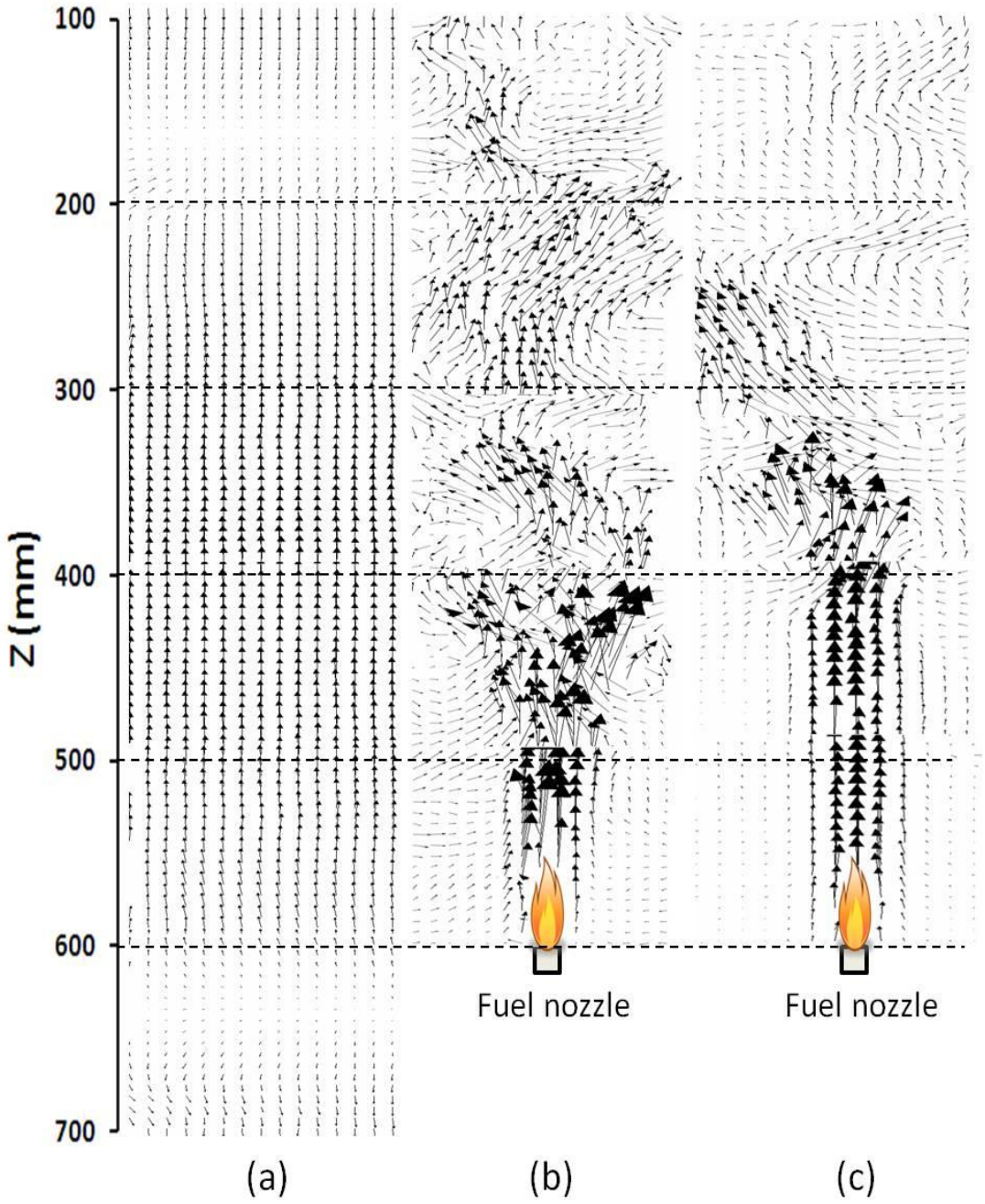

Figure 5.6: Two-dimensional velocity vector maps in the square tube. (a) Excitation at 385 Hz without flame, (b) Excitation at 385 Hz with flame at Z = 600 mm, (c) Flame at Z = 600 mm without excitation. In the cases (a) and (b), the PIV images were taken at an acoustic phase of 0°. The vector map is synthesised from 6 view fields of PIV data. (Note that the plot has been scaled up in the horizontal direction for clarity).

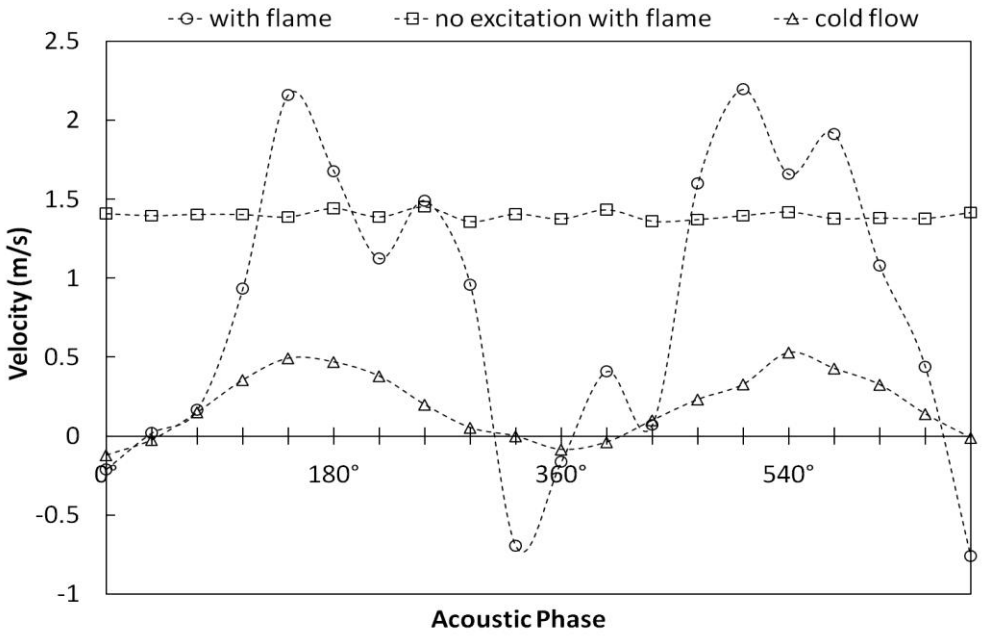

Figure 5.7: The velocity magnitude at 40 mm above the exit of nozzle position B at excitation frequency of 385 Hz. (The initial fuel flow velocity is 0.32 m/s).

Farhat et al. [38] observed that the flame pattern inside an acoustically driven tube is highly sensitive to the location of the fuel nozzle along the tube. The present study demonstrates how the standing wave affects the flame flow field in the tube. The visible flame images in Fig. 5.8 show that the flame is stable in nozzle position A (Z = 200 mm). The flame height and shape remain the same as that without excitation. When the fuel nozzle was move to nozzle position B (Z = 400 mm), the flame oscillation become stronger, while both the mushroom-shaped yellowish flame and blue flame near the nozzle are observed. In nozzle position C (Z = 600 mm), the large scale flame oscillation reduced again. The result in Fig. 5.5 indicates that the velocity variation of the acoustic field in nozzle positions A and C are low; therefore the flame pattern is almost the same as that without excitation. In nozzle

position B, the flame experiences high acoustic variation; hence strong flame oscillation structure is observed. Figure 5.5 also shows that the velocity variation of the cold fuel jet follows the acoustic excitation in a sinusoidal form. In the velocity anti-node region (nozzle position B), the acoustic effect is particularly strong and the fuel is even pushed back to the fuel nozzle. In the case of continually raising the excitation intensity or reducing the fuel flow rate, the flame will eventually blow out.

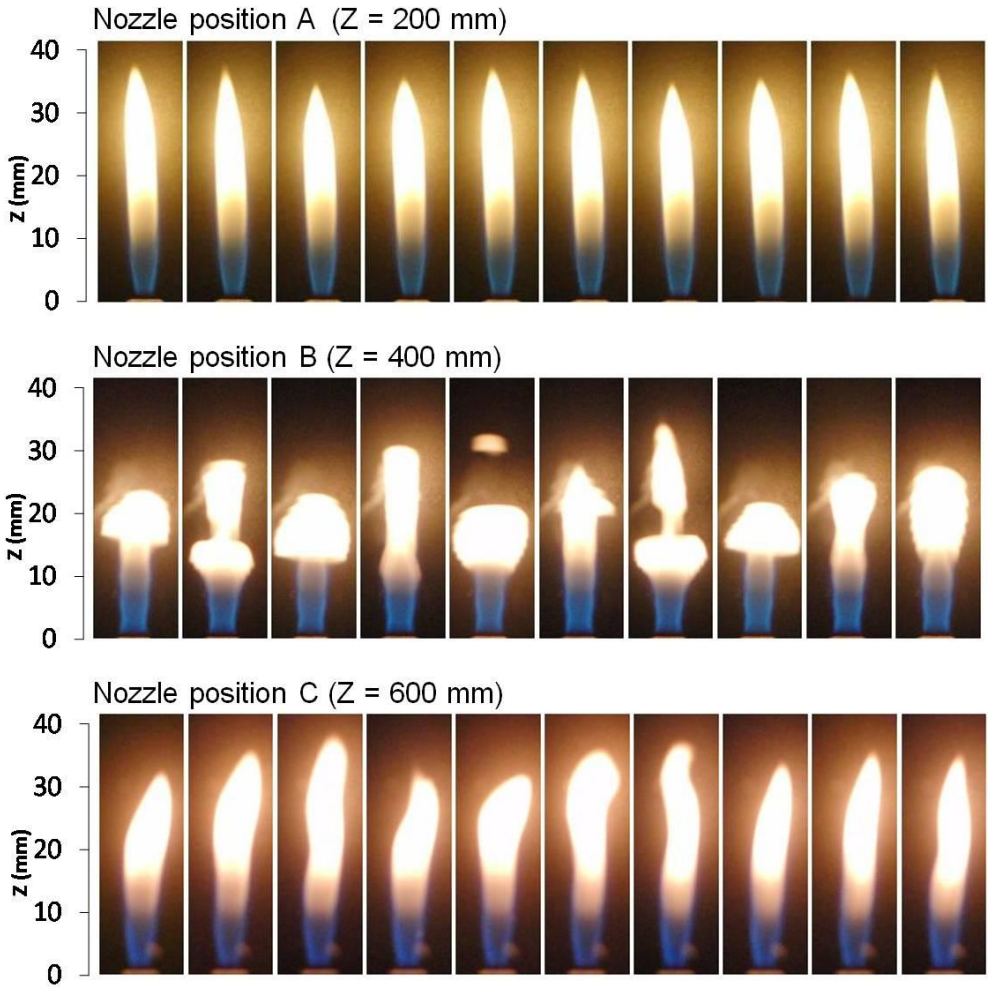

Figure 5.8: Flame images at an excitation frequency of 385 Hz. (Time interval = 1/60s).

Figure 5.9 shows the schlieren images of the flame at different locations of the tube at the excitation frequency of 385 Hz. Due to the variation of flow density gradient in each case, the reacting region and the mixing zones of the hot gases can be observed. The case without excitation is also shown in Fig. 5.9(a), in which a stable and laminar hot gas flow pattern is observed. After triggering the acoustic signal, the flow pattern of the hot gases is disturbed slightly at the upper half of the images in nozzle position A and C. In nozzle position B, the hot gas flow is strongly disturbed and a mushroom-shaped turbulent flow pattern is observed.

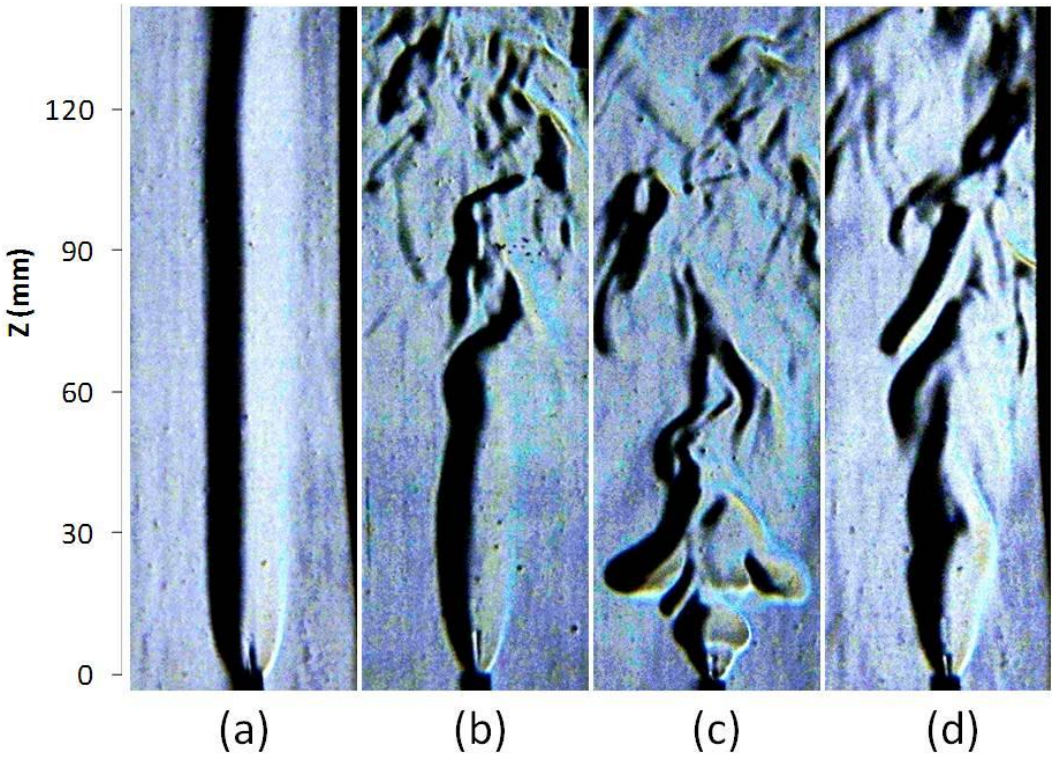

Figure 5.9: Instantaneous schlieren images, (a) No excitation with the flame in nozzle position C, (b) Excitation at 385 Hz with the flame in nozzle position A, (c) Excitation at 385 Hz with the flame at nozzle position B, (d) Excitation at 385 Hz with the flame in nozzle position C.

Figure 5.10 shows the schlieren images, which are enlarged in the region above the nozzle exit, with nozzle positions at A (Z = 200 mm), B (400 mm) and C (600 mm) respectively. The periodic and reproducible characteristics of the unburnt fuel jet are shown in each case. The unburnt fuel jet comes out continuously from the nozzle exit at Z = 200 mm and 600 mm (velocity node regions). At Z = 400 mm (velocity anti-node region), the unburnt fuel jet is shown to be pushed back to the fuel nozzle after the third image and then comes out again in the last image. This result confirms that the acoustic excitation has a significant effect on the fuel flow at the velocity anti-node regions. This is consistent with the result in Fig. 5.5.

Figure 5.11 shows a sequence of schlieren images at the excitation frequency of 385 Hz at Z = 400 mm. The time interval between each image in Fig. 5.11(a) is 1/2,000 second. The variation of the flow pattern is tiny and difficult to detect over 5 images, which is approximately one excitation cycle. In Fig. 5.11(b), the time interval between each image is 1/60 s. The variation of the mushroom-shaped flow pattern is shown to be periodic and the frequency between each cycle is around 13 Hz. The results indicate that the external excitation has a significant effect on the flame dynamics, but the major oscillation of the mushroom-shaped pattern follows the natural flickering frequency of flame.

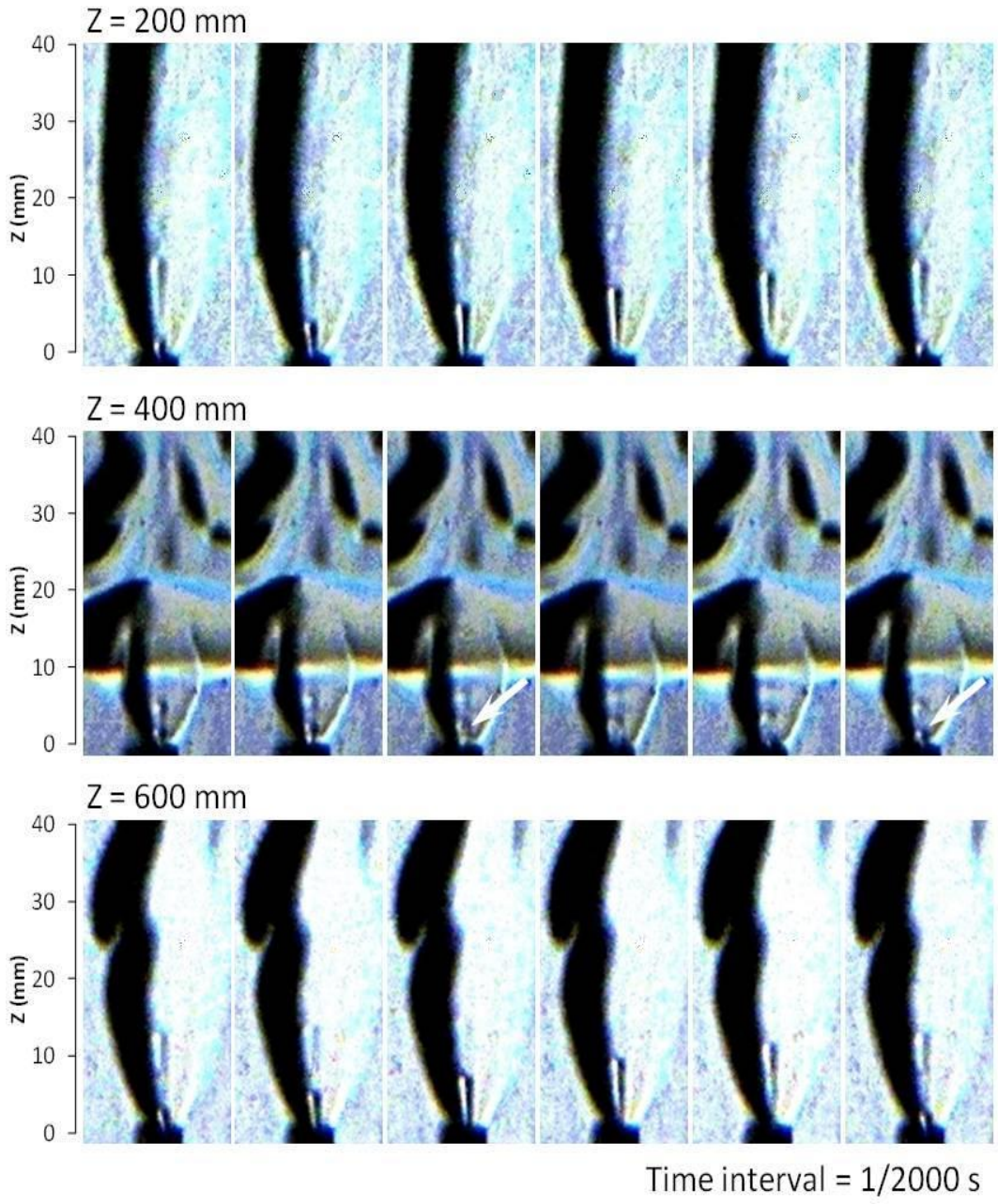

Figure 5.10: The variation of the unburnt fuel jet under the excitation frequency of 385 Hz with the flame at Z = 200, 400 and 600 mm (refer to Fig. 3.2.).

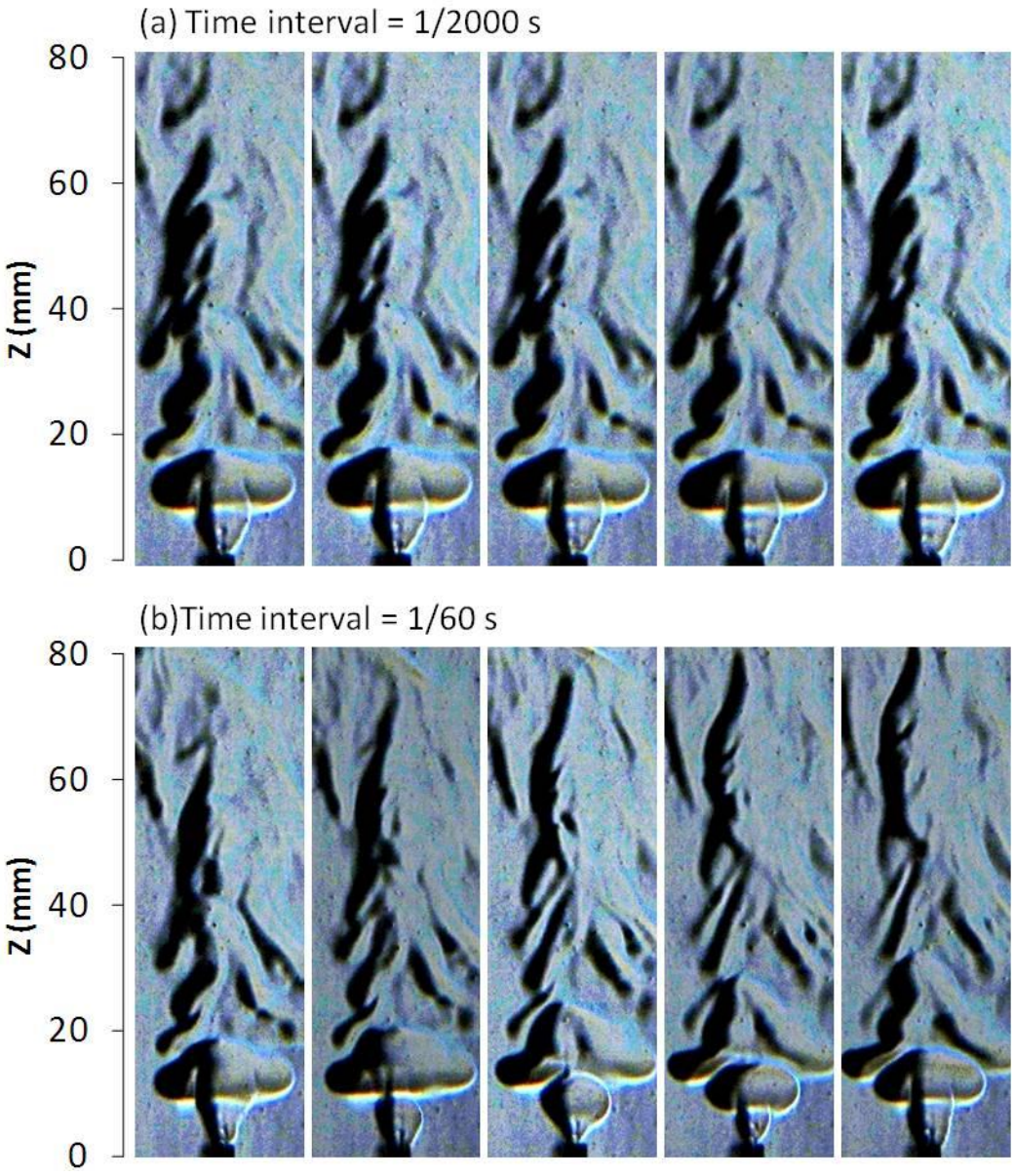

Figure 5.11: Time sequence of schlieren images at the excitation frequency of 385 Hz at Z = 400 mm, (a) The time interval between two images is 1/2,000 s and approximately one excitation cycle is shown and (b) The time interval between two images is 1/60 s.

Velocity vectors and the vorticity contour maps of phase-resolved PIV results are shown in Fig. 5.12. In nozzle position C, upward flow motion is observed at phase angles of 0°, 72° and 144°, while reverse flow is observed at 216° and 288°. Compared with Fig. 5.4 of cold fuel jet flow, it can be seen that, due to combustion, the flow reversal is observed at the same phase angle of 216^{o} for all three positions instead of at variable angles. The buoyancy effect in the flow is clearly shown in the velocity vectors maps. Maximum flow velocity fluctuation was observed in the areas above the flame tip. At an acoustic phase angle of 72°, due to the highest upward flow combined with the buoyancy effect of flame, the highest velocity among the maps was observed and the velocity can reach to 2.3 m/s. In nozzle position B (Z = 400 mm), as the maximum velocity fluctuation occurs in this region, a particularly large variation was observed at each phase. In nozzle position A (Z = 200 mm), due to the acoustic node in this region, the velocity fluctuation becomes more stable. However, the vorticity contour maps show that the vortices are stronger. In comparison, no obvious vortex is observable for the cold jet case shown in Fig. 5.4. This may be explained by the fact that the stable flame created a continuously stronger upward flow, while fresh air was sucked back into the tube, which was caused by the acoustic standing wave. Hence, due to the effect of Kelvin-Helmholtz instability, two opposite direction flows form a stronger vortex. The vorticity production correlates well with the local flame geometry was also observed in the vorticity contours. For example, the flame front of mushroom flame shapes in Fig. 5.8 at nozzle position B and the schlieren images in Fig. 5.9(c) at Z = 30 mm to 60 mm. To sum up, the results demonstrate that the phase sensitivity

cannot be ignored in the investigation of flame and acoustic wave coupling phenomena.

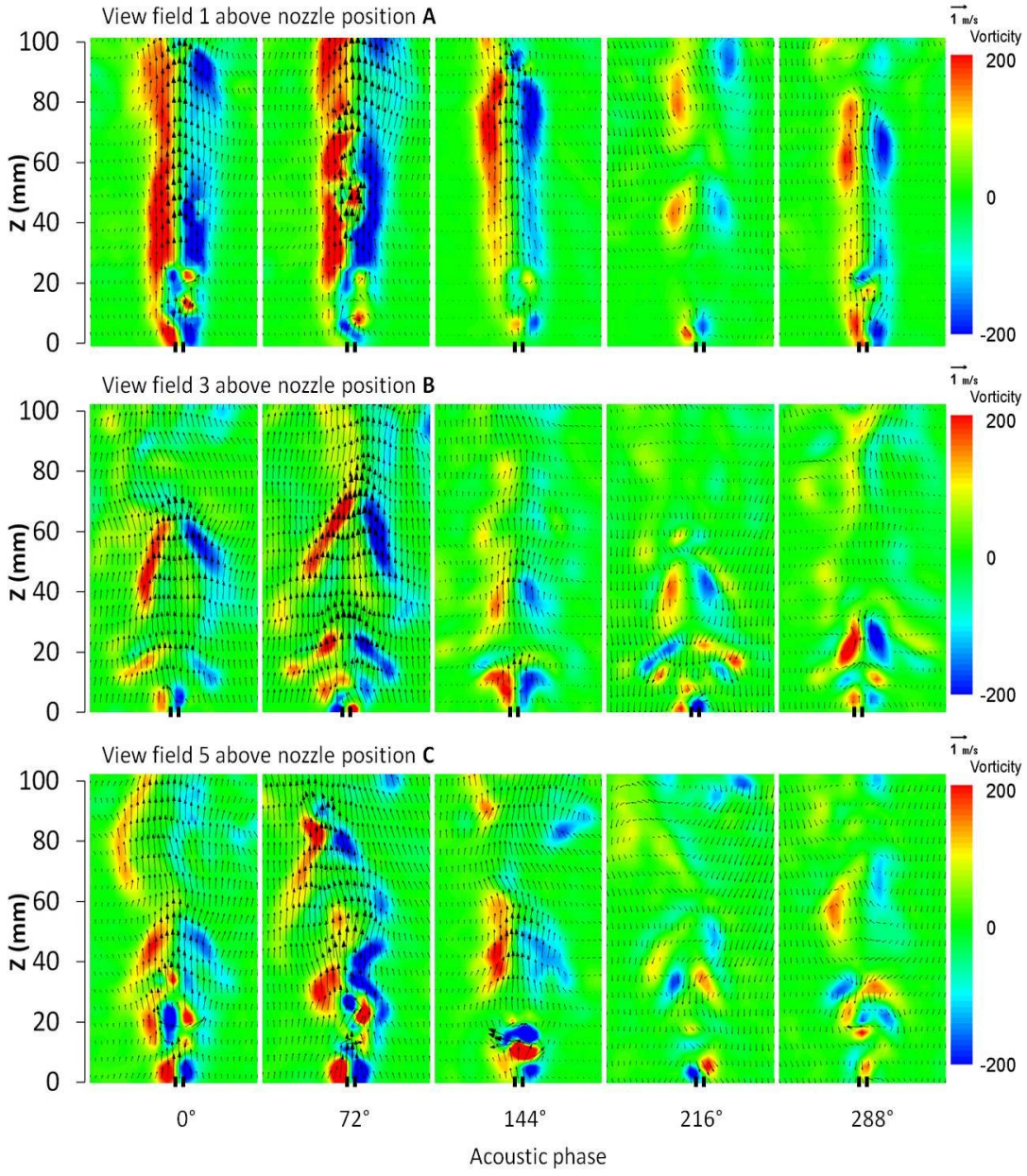

Figure 5.12: Velocity vectors and the vorticity contour maps of diffusion flame flow in view fields 1, 3 and 5 (see Fig. 3.2.). Notice the reverse flow occurs at 216° for all three positions, instead of at variable angles as shown in Fig. 5.4. (Phase-resolved instantaneous PIV results at acoustic excitation frequency of 385Hz).

5.4 The Effect on Hydrogen Flame

Hydrogen contains no carbon or sulphur, hence no carbon monoxide, soot or any unburnt hydrocarbons are produced during the combustion reaction. It has the potential to become a major clean energy source in the near future. Also, the use of hydrogen has been shifted from the application of high-speed aero-propulsion systems to the application for industrials in recent years. However, the hydrogen flame has rarely been touched in the research area of flame/acoustic interaction. In this section, hydrogen fuel test is used in order to understand the acoustic standing wave effect on a different fuel type.

The flow parameters in the experiment are shown in Table 5.1. The thermal loading of hydrogen combustion was set to be the same as for the propane diffusion flame case. The thermal loading was calculated from Eq. 5-1:

$$\text{Thermal loading} = \dot{Q} \times \rho \times h_f \tag{5-1}$$

where $\dot{Q}$ is flow rate (m^3/s),

ρ is the density of fuel (kg/m^3) and

h_f is the calorific value of fuel (KJ/kg).

The result shows that the thermal loading of propane gas in the flow rate of 9.2 $\times 10^{-4}$ m^3/s (55 ml/min) is 0.088 KW. The flow rate of hydrogen gas at 6.9 $\times 10^{-3}$ m^3/s (415 ml/min) has the same thermal loading as propane.

Table 5.1: Hydrogen flow parameters in the experiment.

Gas type	Flow rate (m^3/s)	Density (kg/m^3)	Δhf (KJ/kg)	Thermal Loading (KW)
C_3H_8	9.2×10^{-4}	1.91	50.32	0.088
H_2	6.9×10^{-3}	0.09	141.8	0.088

Figure 5.13 illustrates the hydrogen flame images with and without acoustic excitation. Hydrogen flames are difficult to visualise in the daylight. To visualise the flame pattern, the TiO_2 particles were seeded to the surrounding air, which caused the hydrogen flame colour to become light orange. In the case without acoustic perturbation, the flame was stable over five images. In comparison with the propane flame, the hydrogen flame pattern was twice as high as, and wider than, the propane flame under the same thermal loading. After triggering the acoustic signal, the hydrogen flame was slightly disturbed by acoustic perturbation, particularly, at nozzle position B. The flame shape becomes shorter and the lower half of the visible flame turned thinner. At nozzle position C, the flame oscillating behaviour was difficult to detect and only a wavy-shaped flame surface was observed. The result is similar to the propane diffusion flame, in which the flame was the most unstable in the acoustical anti-node region. However, the flame oscillation was smaller and the flame remained attached to the nozzle edge during each excitation cycle.

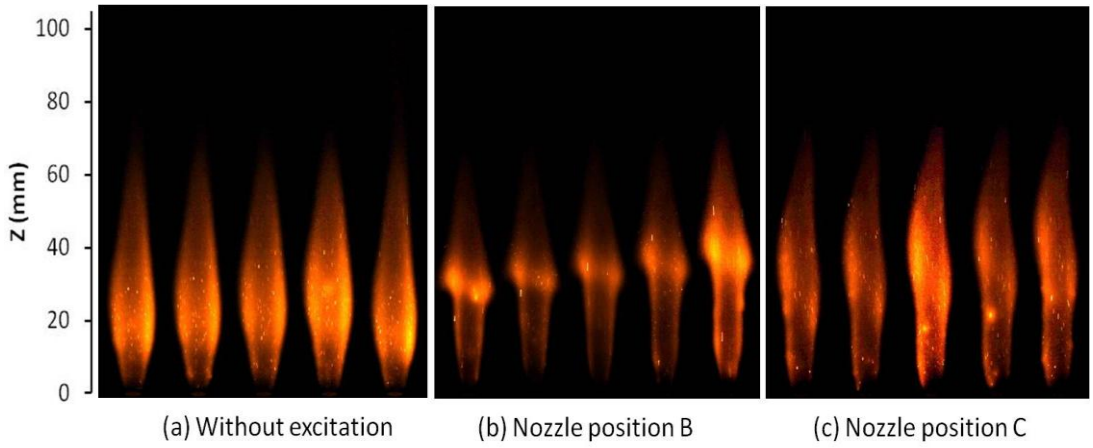

Figure 5.13: Hydrogen flame images under the excitation frequency of 385 Hz. (time interval = 1/250s).

Figure 5.14 displays the instantaneous schlieren images of the hydrogen flame under acoustic standing wave in nozzle positions B and C. The case without excitation is also presented as a reference, which is shown in Fig. 5.14(a). A symmetrical vortex like flow pattern is observed at Z = 40 mm, which indicates that a very stable flame with slight flame flickering occurs at that condition. After triggering the acoustic signal, the image shows that the hot gas flow pattern is easily disturbed by acoustic excitation at nozzle position B (velocity anti-node region). The strong mushroom-shaped turbulent flow pattern is observed in the schlieren images. At position C, the mushroom-shaped flow pattern is still obvious, but it is much weaker than that at position B. The result is unlike the visible flame images, which look quite stable and only small wavy-shaped flame surface is observed. It can be seen that the flame flow still follows the up-and-down flow motion of acoustic flow field. However, due to the high burning velocity and high

initial velocity of the hydrogen fuel jet, the visible flame looks less affected by the excitation.

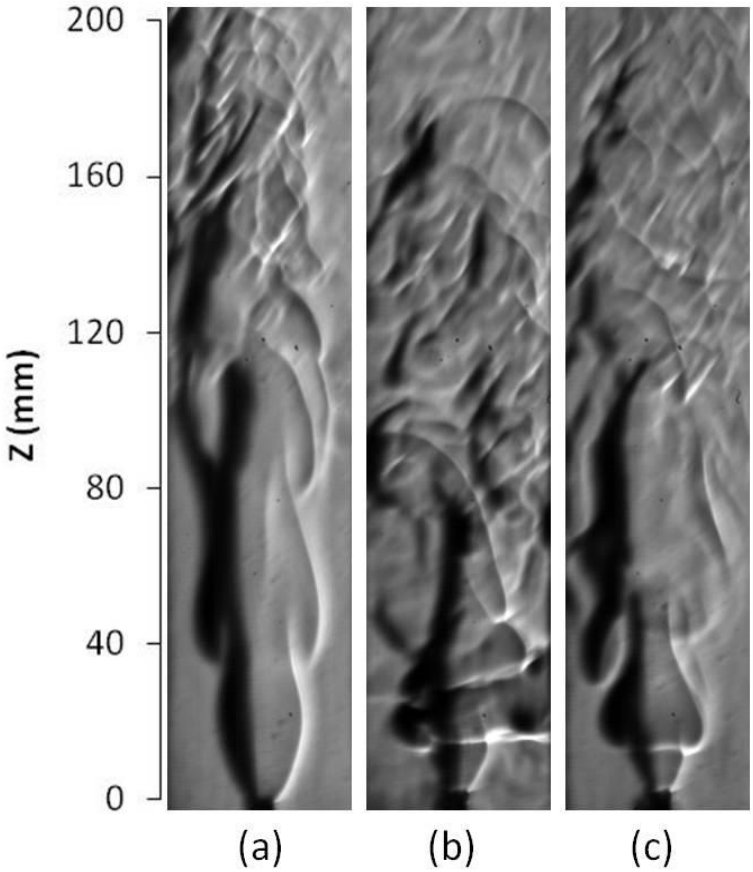

Figure 5.14: Instantaneous schlieren images of the hydrogen flame under the excitation frequency of 385 Hz, (a) Without excitation; (b) Nozzle position B; (c) Nozzle position C. (Nozzle positions refer to Fig. 3.2.)

Figure 5.15 shows the phase-locked velocity contours and streamlines plots of the hydrogen flame flow at velocity node and anti-node regions. The flow velocity of the hydrogen flame is higher than that of the propane diffusion flame, and the buoyancy effect is also stronger (see Figure 5.12.). No matter at which position the

fuel nozzle is in the tube, or at which phase angle of the excitation signal, the flow always maintains an upward motion. The downward acoustic flow is not strong enough to reverse the upward flow trend. For nozzle position B (velocity anti-node region), at phase angle of 288°, strong vortices are observed at Z = 40 mm. Comparing the data with the Fig. 5.13(b), the vortex has appeared above the flame front. In this region, the strongest downward acoustic flow pushes the flame front, while the upward flame is resisting it. Hence, the cone-shaped flame is formed and the two strong opposite direction flows form a strong vortex due to the effect of Kelvin-Helmholtz instability.

Figure 5.16 is the velocity magnitude of the acoustic flow at the excitation frequency of 385 Hz. The measure positions were at 20 mm left of the nozzle centre (flame tip region) and 70 mm above the nozzle exit (non-combustion reaction region). The results show that the flow motion follows the sine-wave signal, both in the flame tip region and in the non-combustion reaction areas. The flow motion of the acoustic at nozzle position C (velocity node region) is smaller than that of nozzle position B (velocity anti-node region). However, due to the high initial flow velocity of the fuel jet and strong upward flow, the surrounding air motion trends to go upward. The downward flow motion is not obvious. In the flame tip region, the strong velocity oscillation is observed, but no downward flow motion is detected. Therefore, the flame pattern shows strong under excitation perturbation and the flame shape is only slightly affected by the acoustic variations.

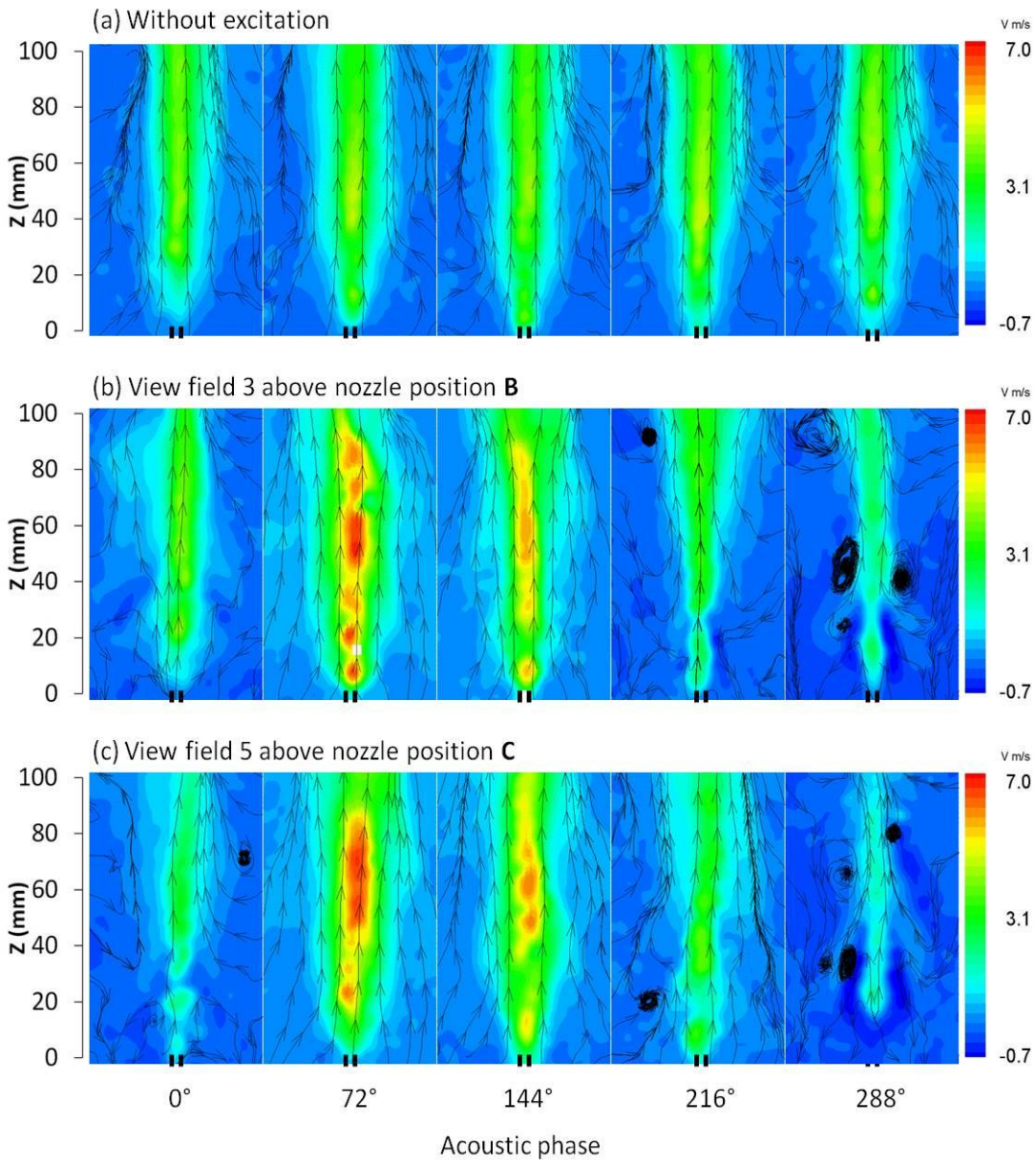

Figure 5.15: Phase-locked velocity contour and streamline plots of the instantaneous hydrogen flame flow, (a) without acoustic excitation (frame rate = 7.25fps) and (b and c) with an excitation frequency of 385Hz and at nozzle position B and C (see Fig. 3.2.).

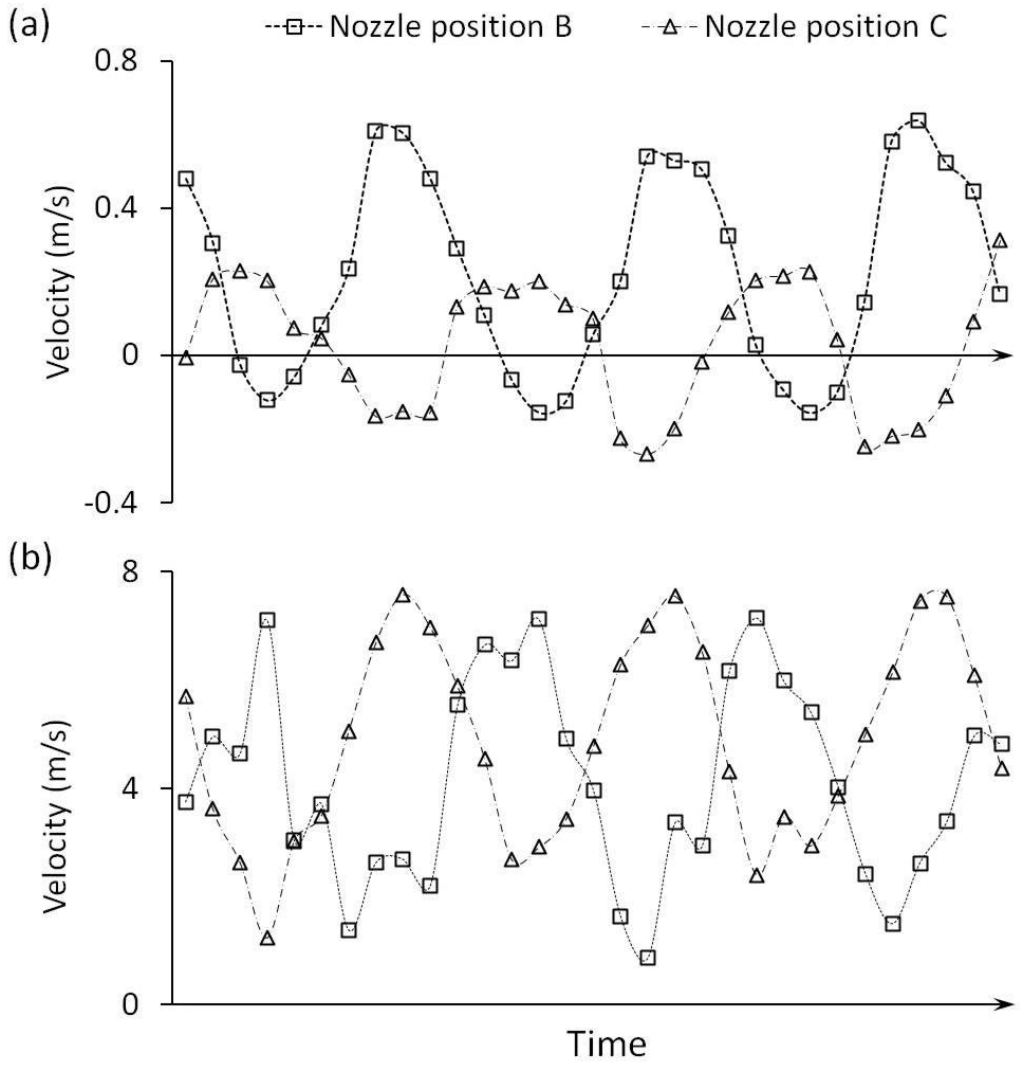

Figure 5.16: Velocity magnitude of acoustic flow and hydrogen flame flow at the excitation of 385 Hz, (a) Measured at 20 mm left of the nozzle centre and (b) Measured around 70 mm above the nozzle exit. (Frame rate = 7.25 fps)

5.5 Summary

In this chapter, a phase-locked PIV system, combined with a high speed schlieren visualisation system, was applied to investigate the flow characteristics and flame structure in an acoustically excited tube. The velocity distributions of acoustic flow

along the tube were measured. The effect of the standing waves on both the cold jet fuel flow and the jet flame were also analysed. The results indicated that the cold jet flow and the propane jet flame are a strong function of the phase angle and also highly sensitive to the location of the standing wave in the tube. At some phase angles the jet characteristics were completely blurred by the acoustic flow field. In the velocity node area, the jet was less affected by the excitation. In contrast, the jet was observed to experience large velocity variations in the velocity anti-node area. This proves that under the acoustic excitation, the flame behaviour is affected by both the spatial variation and phase angle of a strongly oscillating acoustic field. The variation of ambient air motion and the acoustically induced fluctuation of the jet fuel flow should also be considered in the investigation of the flame and acoustic wave coupling. For the hydrogen flame case, the high velocity of the initial fuel jet and strong upward flame flow were enough to resist the largest downward acoustic flow. The flame dynamics were found to be more stable than the hydrocarbon flame under the excitation perturbation. However, the large oscillation in the schlieren images indicated that the hot gases were still pushed by acoustic flow and created a wavy-shaped flame surface.

Chapter 6

Nonlinear Coupling of Flame Dynamics and Acoustic Excitation

The nonlinear coupling phenomenon of flame dynamics and acoustic excitation, and the flow characteristics of propane/air flames at the acoustic anti-node region of a standing wave (385 Hz) are the focal points of this chapter. Three different equivalence ratios (Ø) of propane/air premixed flames and a propane diffusion flame under different acoustic excitation intensities were measured by a chemiluminescence emission measurement system and a phase-locked PIV system. Detailed results are performed below.

6.1 Introduction

The results from the previous chapter have shown that the diffusion flame dynamics are significantly affected by the standing wave in a tube, due to the large velocity oscillations of acoustic field in the anti-node region. Kartheekeyan et al.

[111] and Kim et al. [112] have demonstrated that external forcing induced flame periodic oscillations may further create undesirable nonlinear oscillations which will affect the initial flow velocity and mixing rate in the premixed flame case. Experimental work has shown that flames will exhibit nonlinear responses under various acoustic and combustion conditions. In nonlinear systems, the flame oscillation wave and acoustic excitation wave may induce the other frequency components besides the excitation frequency. For instance, the sub-harmonic flame response is found in pulsed premixed methane/air flames in Bourehla and Baillot's research [113], and Williams et al. [114] showed the existence of sub-harmonic flame oscillation components of $f/2$, $f/3$, $2f/3$, $f/4$, and $f/5$ in a laser-based investigation on the structures of a acoustically excited flame.

Recently, Huang et al. [115] have identified the nonlinear coupling between the buoyancy driven flame instability and acoustic excitation using high speed colour imaging and innovative colour digital image processing techniques on an acoustically excited and baffle stabilised diffusion flame burner. In the present study, a chemiluminescence emission measurement system (PMT) was adopted to systematically examine the oscillating frequency of propane-air flames under different intensities of acoustic excitation, especially on the nonlinear coupling of the flame dynamics and acoustic excitation. Detailed flame flow velocity fields and vorticity were measured and calculated by a PIV system to further understand the flame/acoustic coupling behaviour.

The flow parameters in the experiment are shown in Table 6.1. The propane fuel flow rate was set at 55 ml/min. Base on this fuel flow rate, three different equivalence ratios ($Ø = {}^{f}/_{f_s}$) of premixed flames were set as main test parameters.

Table 6.1: Propane/air flow parameters in the experiment.

Equivalence ratio (Ø)	Air mass flow rate (kg/s)	Fuel mass flow rate (kg/s)	Air flow rate (ml/min)	Fuel flow rate (ml/min)	Velocity (m/s)
1.5	1.82×10^{-5}	1.75×10^{-6}	910	55	1.28
3	9.10×10^{-6}	1.75×10^{-6}	455	55	0.67
5	5.46×10^{-6}	1.75×10^{-6}	273	55	0.43

6.2 Observation of the Visible Flame

Figure 6.1 shows the visible flame images at different equivalence ratios under the excitation frequency of 385 Hz and at a voltage amplitude of 13.7 V (2 V in the case of Ø = 1.5). The strongly oscillating diffusion flame case is also shown in Fig. 6.1(a). It can be seen that the premixed flame under the same acoustic excitation is more stable than the diffusion flame. Moreover, the flame pattern is more stable when the air-fuel mixing ratio increases. At the equivalence ratio of 5, the reddish flame colour is only visible at the flame tip. The flame oscillation behaviour is similar to that of the diffusion flame, but it is much weaker. At Ø = 1.5, which is the flammability limit of the present nozzle, the flame oscillation is the weakest of all

the test cases. The flame cone angle almost remains the same under acoustic forcing. However, the flame can be extinguished suddenly after a slight increase of amplitude. The observations demonstrate that the premixed flame behaviour is quite different from that of a diffusion flame under acoustic perturbation. A diffusion flame can become a lifted flame, a partially premixed flame and a partially extinct flame type during each flame oscillation cycle.

In the premixed flame case, the flame pattern is generally stable and only a slight oscillation can be observed when it is under external excitation. For instance for Ø = 3, Fig. 6.1(c) shows that the flame bottom is attached to the nozzle in the 2nd image and then the flame is partially lifted. After that, the visible blue flame pattern is observed below the nozzle exit. It can be explained by the fact that if the acoustic flow is going downward (see the PIV results in Fig. 6.3) then the flame is pushed by the acoustic wave. In contrast, the flame slightly lifts-off once the acoustic flow is turned upwards. The study also found that this kind of flame behaviour is not observable at Ø = 1.5. As shown in Table 6.1, the initial mean nozzle exit velocity at Ø = 1.5 is higher than the other cases, at a value of 1.28 m/s. This is much higher than the largest downward acoustic flow velocity which is around 0.6 m/s. It can be seen that in the extreme case the fuel jet can still resist the downward acoustic wave. Therefore the flame is stable at each phase angle of the excitation cycle. However, the flame is close to the lower flammability limit at Ø = 1.5, and so the mixture may be further diluted by the acoustic perturbation, and then blows out eventually after slightly increase the excitation intensity.

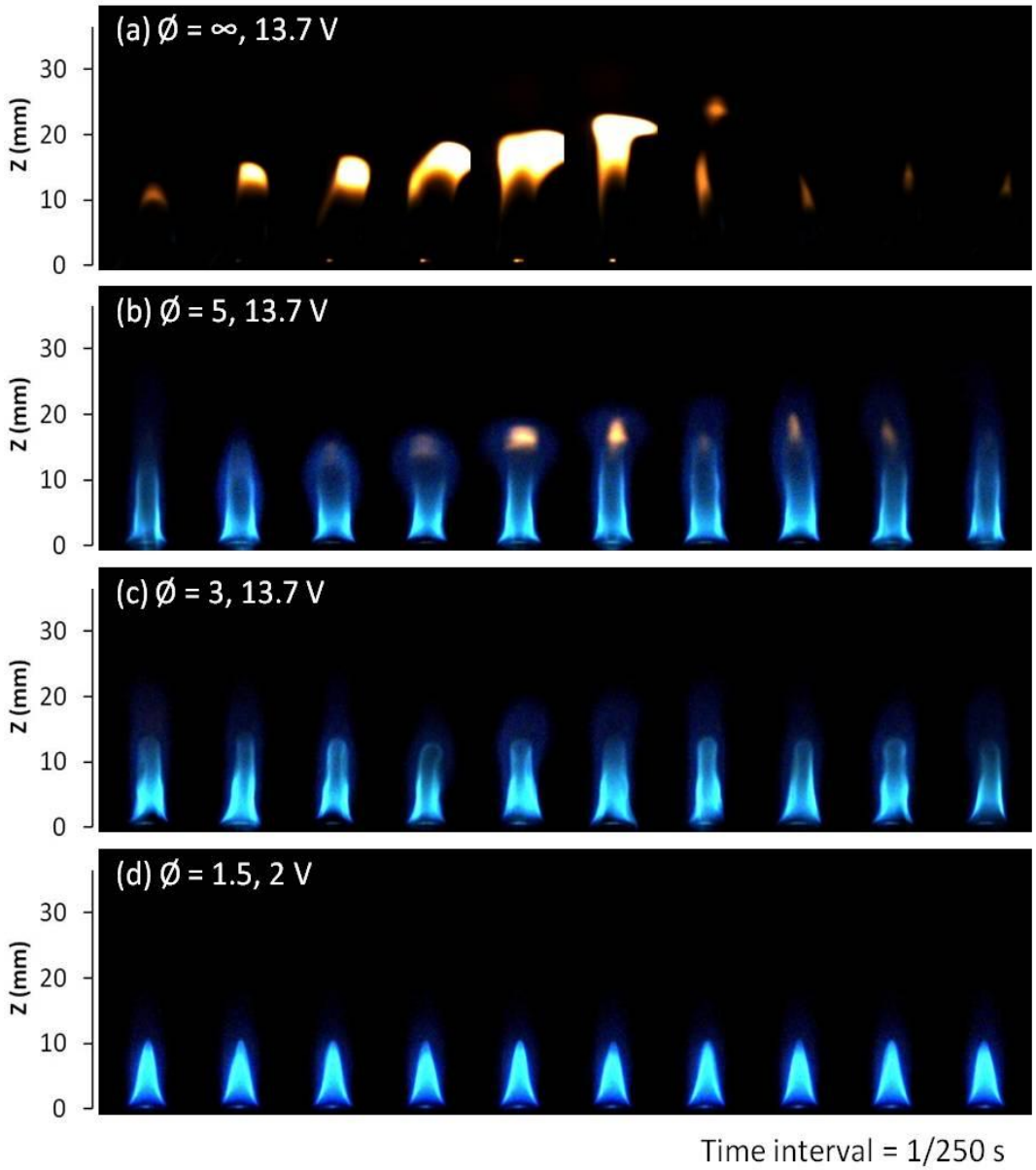

Figure 6.1: Propane-air flame images at different equivalence ratios and at the excitation frequency of 385 Hz.

6.3 Frequency Analysis of the Flame Oscillation Behaviour

Figure 6.2 illustrates the power spectrum of CH^* chemiluminescence signals of the premixed flames under acoustic excitation. The frequency components are very

different at the various equivalence ratios and external excitation intensities. For the case of premixed flame, at a voltage amplitude of 0.3 V, the only visible peak is the forcing frequency. For the diffusion flame (Ø = ∞), both the flame flickering frequency (f_f = 15 Hz) and the forcing frequency (f_e = 385 Hz) are observable. Moreover, the harmonic frequencies of the natural flame frequency are observed at 0.3 V. Zoomed into the excitation frequency peak region, two small peaks are found, which exhibit a relationship of $f_e \pm f_f$ in the case of Ø = ∞. At the voltage amplitude of 13.7 V and 2 V, the excitation frequency is found, accompanied by two sets of fore and aft peaks. Data indicate that these complementary peaks exhibit a relationship of $f_e \pm f_f$ and $f_e \pm f_e/5$, and two clear peaks are also visible at the natural flickering frequency (f_f) and the sub-harmonic frequency of the excitation frequency, which is $f_e/5$. Unlike the obvious flame flickering in the diffusion flame, the natural flame flickering frequency in the premixed flame case is hard to detect, and the external perturbation intensity is strong enough to overshadow the low frequency buoyancy induced flame flicker. Therefore, the sub-harmonic frequency ($f_e/5$) is observed as the main complementary frequency peaks, instead of the flame flickering frequency. For instance, the complementary peaks are shown in a relationship of $f_e \pm f_e/5$ in the premixed flame at 2 V.

The above mentioned frequency components can be explained by nonlinear theory and they can be attributed to the nonlinear response modes. For instance, the harmonic frequencies of the natural flame frequency in the diffusion flame are correlated to the nonlinear response which is shown in below:

$$y_f(t) = Y_f sin\,(n\omega t + \varphi_f) \tag{6-1}$$

The fore and aft complementary frequency peaks at higher forcing intensities have been reported recently by Huang et al. [115] in a different test rig and using high speed colour imaging and processing. They have also been observed in the nonlinear response of quasi-periodic fluid motion [116]. Fenstermacher et al. [117] examined the turbulent transition of radial fluid velocity under cylindrical rotational excitations using Laser-Doppler Velocimetry along with Fourier-Transformation (FT). The results showed the existence of a subtractive frequency coupling component similar to that of the f_e - f_f and f_e - f_e/5 modes. The nonlinear coupling between the $x_e(t) = X_e sin(\omega_e t)$ and $x_f(t) = X_f sin(\omega_f t)$ or $x_{e/5}(t) = X_{e/5} sin(\omega_{e/5} t)$ wave signals may result in the creation of a $k\sin(\omega_e t)\sin(\omega_f t)$ or $k\sin(\omega_e t)\sin(\omega_{e/5} t)$ frequency component, and then it can be broken down into the equations shown below:

$$k(cos([\omega_e - \omega_f]t) - cos([\omega_e + \omega_f]t))/2 \tag{6-2}$$

or

$$k(cos([\omega_e - \omega_{e/5}]t) - cos([\omega_e + \omega_{e/5}]t))/2 \tag{6-3}$$

This may explain the observed nonlinear coupling relationship of $f_e \pm f_f$ and $f_e \pm f_e$/5.

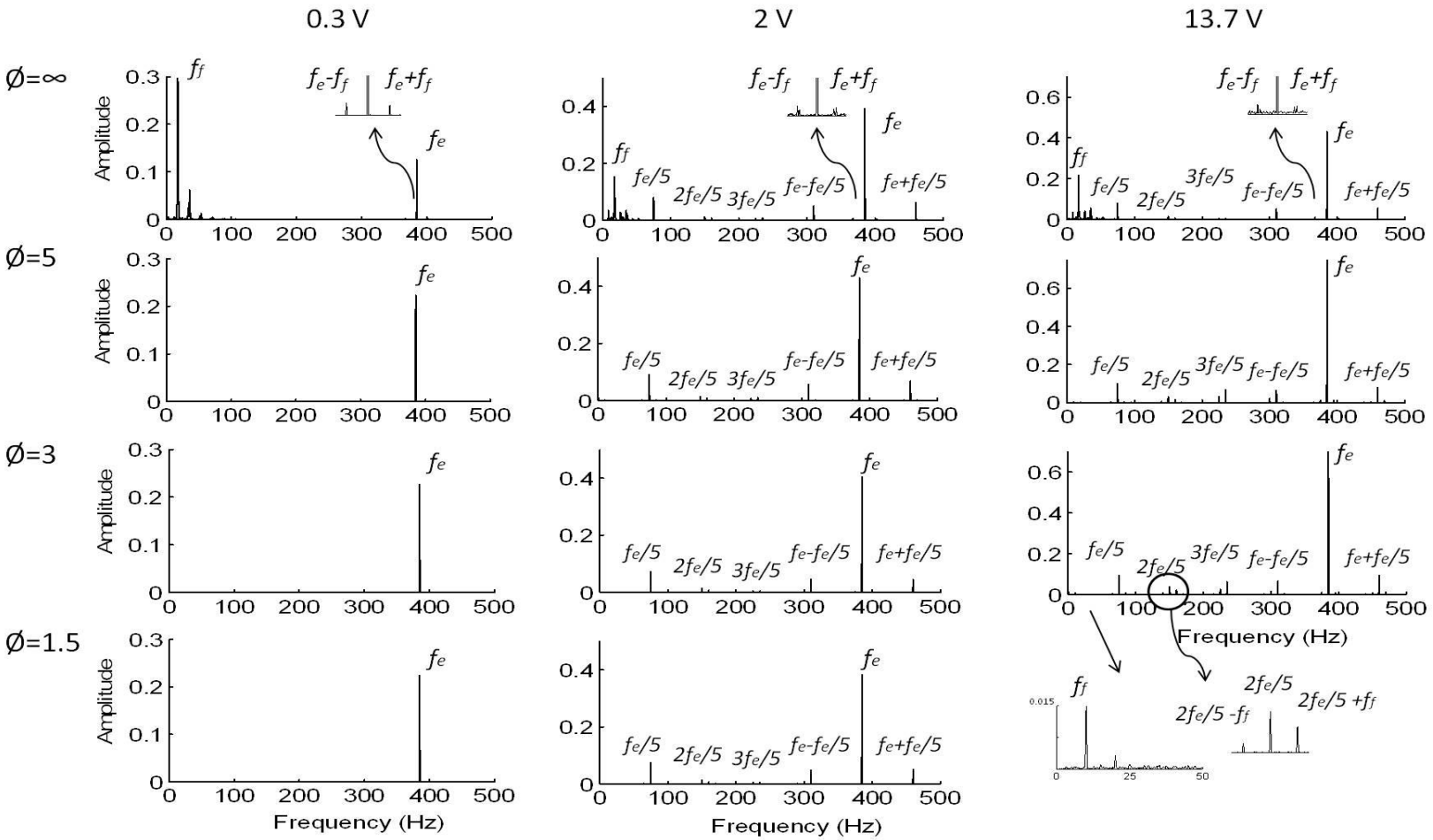

Figure 6.2: Power spectra of CH^* chemiluminescence signals for various equivalence ratios of premixed flames at different excitation intensities.

By studying the forcing intensity effect, it has been found that there is no observable harmonic coupling at 0.3 V. After further increasing the voltage amplitude to 2 V, the frequency component is similar at each premixed flame case and the external forcing has no obvious effect on the premixed flame at different equivalence ratios. However, the sub-harmonic frequencies, which are $2f_e/5$ and $3f_e/5$, become visible in both the diffusion and premixed flame cases. Further increasing the voltage amplitude to 13.7 V, the trend of the frequency components is similar to those at 2 V, yet the amplitude of the sub-harmonic response increases. Moreover, a tiny peak is found around 10 Hz at Ø = 3 and 5. A set of fore and aft peaks are also observed to accompany each sub-harmonic frequency. The power spectrum of the premixed flame without excitation indicates that the natural flickering of the premixed flame is around 10 Hz. It can be seen that the lower intensity of the acoustic excitation may overshadow the flicker frequency; however, it may be induced again at higher forcing intensities.

6.4 PIV Examination of Flow Fields

Figure 6.3 shows the velocity vectors and the vorticity contour maps of the flow field of the premixed flames at different equivalence ratios. The trends of the velocity fields of the premixed flame cases are similar to the diffusion flame at the phase angles of 72° and 144°, where the acoustic wave induces an upward flow motion, further accelerating the flame buoyancy effect for each case. The flame flow velocity was then increased to the maximum at these phase angles. At the

phase angle of 0°, the acoustic perturbation was low. The strong upward flow motion was observed above the nozzle for the premixed flame cases and no obvious downward velocity vectors can be seen in X-axis. The displacement of acoustic flow motion only affected the diffusion flame. This is because the fuel jet of the diffusion flame needs surrounding air as an oxidant to sustain the chemical reaction. In this case, the low initial velocity of the fuel jet and ambient air were both affected by the acoustic excitation. The obvious flame flow pattern disturbance can be seen at the phase angle of 0°. At the phase angle of 288°, the largest downward acoustic flow can be observed. The velocity field at this phase angle is very different in each flame case. For the diffusion flame, the upward flame flow and downward acoustic flow create a chaotic flow pattern, whereas, for the premixed flame, the upward velocity vectors can be observed in the centre of each figure, and with increasing air-fuel mixture rate, the flow motion becomes stronger. In the case of Ø = 5, a cone-shaped low velocity field is observed at Z = 20 mm, where the flame front is pushed by the strong downward acoustic field. To compare the data with Fig. 6.1(b), the mushroom-shaped flame tip in the 3^{rd}, 4^{th} and 5^{th} image was matched with PIV velocity data. At Ø = 3, due to the higher air flow rate increasing the initial fuel velocity and resisting the downward acoustic flow, the upward flame flow pattern in the X-axis is stronger than for Ø = 5 at the phase angles of 216° and 288°. It can be seen that the combination of initial mixture flow velocity and the buoyancy effect of flame can resist the acoustic effect.

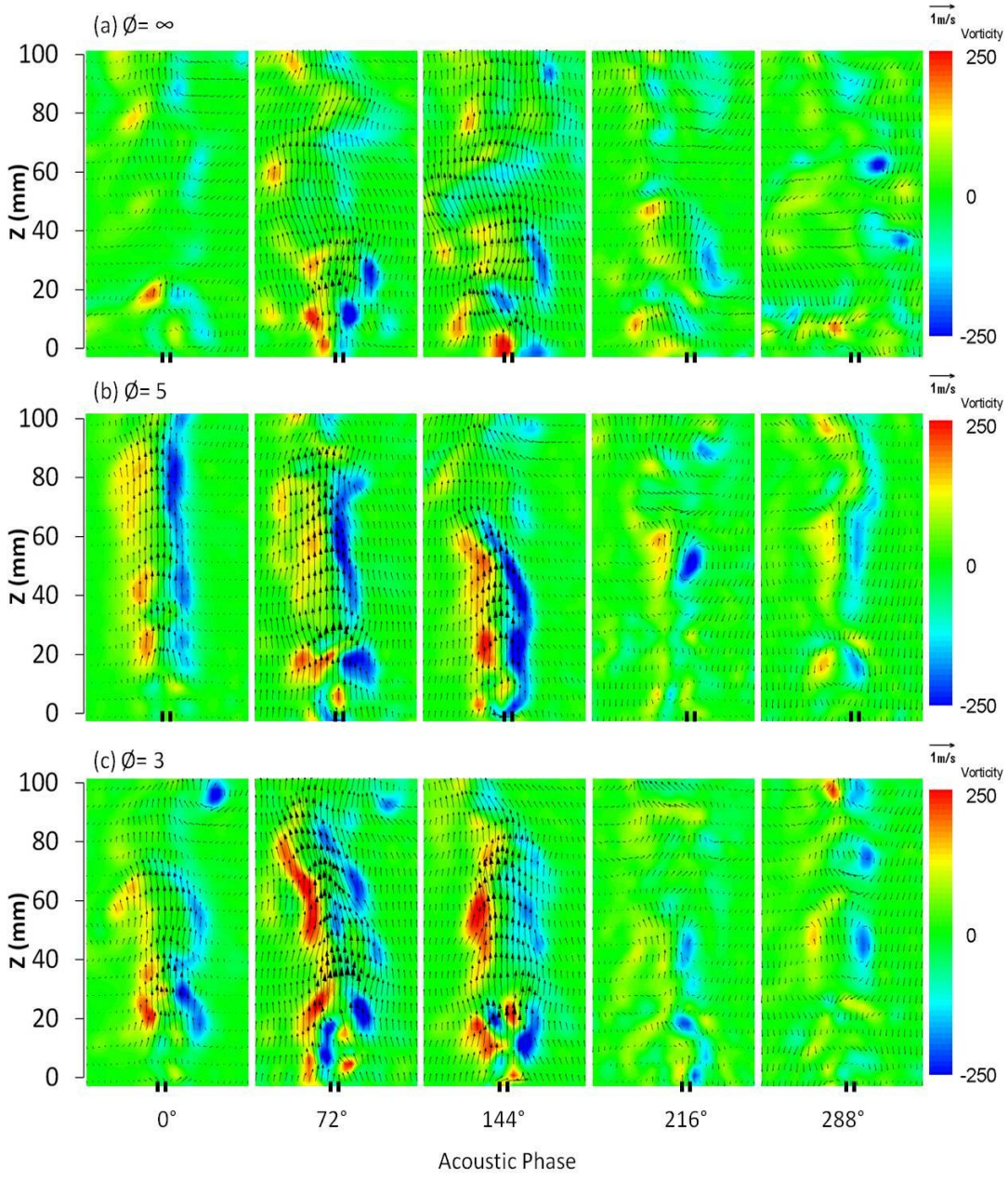

Figure 6.3: Velocity vectors and the vorticity contour maps of the instantaneous propane-air flame flow at the excitation frequency of 385 Hz in view field 3 (see Fig. 3.2).

The vorticity contour maps in Fig. 6.3 illustrate that the angled velocity acceleration zones matched well with the angled vorticity contour. In the diffusion flame, many disordered positive and negative vorticities are spread across the image at each

phase angle. The upward hot gas is broken up by the up-and-down flow motion of the acoustic wave. These local opposite direction flows then form many little vortices due to the effect of Kelvin-Helmholtz instability. In the case of the premixed flame, the distribution of strong vorticity is observed on both sides of the X-axis. The positive vorticity is shown on the left hand side whereas the right hand side is negative. Particularly, vorticity patterns are observed at the phase angles of 0°, 72° and 144°. This is because the higher initial fuel velocity is combined with strong upward hot gases and then further accelerated by upward acoustic flow. Such combination creates a fast flow which is higher than the largest upward acoustic flow. Therefore, these two flows create relative opposite velocity gradients and form the strong vorticity. At the phase angle of 216° and 288°, the flame flow is pushed by the downward acoustic flow and results in lower upward flame flow, hence the vorticity is weaker.

6.5 Summary

An experimental investigation has been carried out to study the nonlinear coupling characteristics of propane/air flames with acoustic standing waves using chemiluminescence emission and phase-locked PIV measurements. A variety of coupling modes of the excitation source with combustion instability oscillations, and its own harmonics and sub-harmonics were observed. The frequency analysis has shown that flame/acoustic coupling behaviour results in a complex nonlinear coupling effect. The coupling behaviour is weak at the lowest excitation intensity (0.3 V). At voltage amplitude of 2 V, the results show that the excitation frequency

is only coupled with the sub-harmonic frequency (f_e/5) for the premixed flame. However, for the diffusion flame, more complex frequency components, which exhibit relationships of $f_e \pm f_f$ and $f_e \pm f_e$/5, were observed. At voltage amplitude of 13.7 V, the sub-harmonic frequencies ($2f_e$/5 and $3f_e$/5) and premixed flame buoyancy oscillations were enhanced. These frequencies were then found to couple with each other and create complex nonlinear frequency couplings. PIV measurements provided detailed flow velocity vector fields in order to enhance the understanding. The acoustic fields induced by acoustic standing waves in a tube at different phase angles and its effect on the flames at different equivalence ratios were measured and analysed.

Chapter 7

Excitation Frequency Effects on the Flame Dynamics

Flame flow characterisations under acoustic standing wave have been discussed in the previous chapters. The flame behaviour affected by the different excitation frequencies is the focus point of this chapter. The main test frequencies include the infrasound (f < 20 Hz) and the non-resonant excitation frequencies, which are between the first and the second resonant frequency of the present test chamber. Detailed results are introduced below.

7.1 Introduction

Chapter 6 discussed that the flame dynamics are significantly affected by the standing wave in a tube due to the different velocity variations in the acoustic velocity node and anti-node areas. However, Humin [96] used the same length and similar area of a cylindrical tube to examine the flame stabilisation. Results showed

that the flame behaviour was stable at excitation frequencies of 140 Hz and 170 Hz. At these frequencies and the nozzle position, the flame behaviour should be unstable because the long wavelength induces large velocity displacements in the velocity anti-node areas. In order to understand a wider range of acoustic excitation frequency effects on flame dynamics, the behaviour of flame dynamics at non-resonant frequencies, which are between 80 Hz and 210 Hz, in the same test rig were investigated. Note that the first and second resonant frequencies of the test rig are at 65 Hz and 220 Hz respectively. Also, frequencies below 20 Hz (infrasound) are also adopted to examine their effect on the flame behaviour. The flame position was set at nozzle position B in all excitation frequencies and the voltage amplitude of acoustic signal was fixed at 33 V.

7.2 Infrasound Effects on the Flame Dynamics

Preliminary tests show that the acoustic flow field is distorted at lower forcing frequencies. The visible flame images and PIV results also show turbulent structures at lower excitation frequencies. However, the power spectrum of CH^* chemiluminescence signals in Fig. 7.1 indicate that the dominant frequency is the same as the external excitation frequency at 9 Hz, 11 Hz and 20 Hz. At frequencies of 5 Hz and 7 Hz, the peak of the excitation frequency can also be easily observed from the power spectrum.

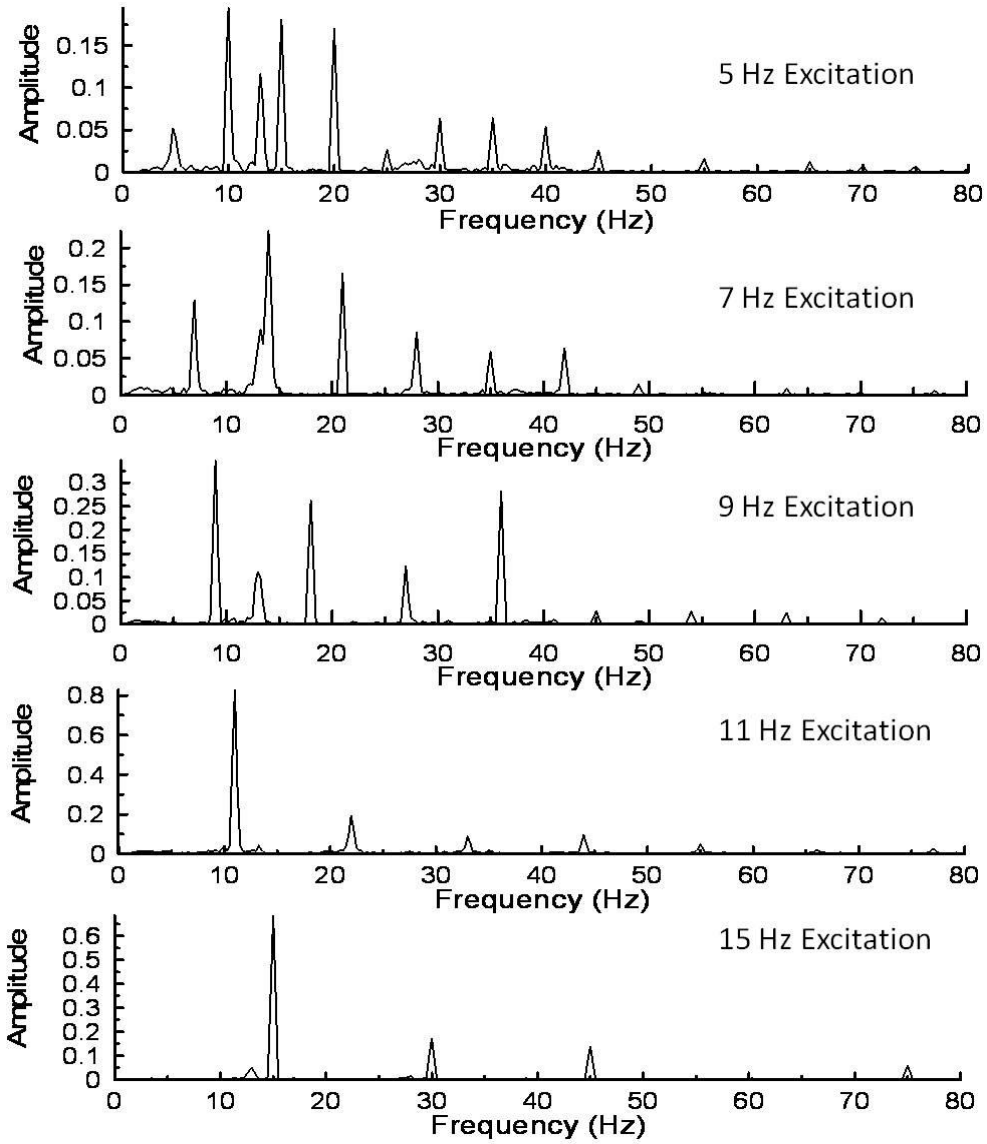

Figure 7.1: Power spectra of CH^* chemiluminescence signals with various excitation frequencies.

Figure 7.2(a) demonstrates the schlieren images at an excitation frequency of 10 Hz with the flame at nozzle position B in the tube. The oscillation of the unburnt fuel jet can be observed near the nozzle exit. The variation of the height of the unburnt fuel jet is shown in Fig. 7.2(b), which indicates that the variation of the unburnt fuel jet is repeatable and follows the excitation frequency. The flame flicking frequency

varying in different area of flame can also be seen from abovementioned results. The harmonic and sub harmonic frequencies can be seen in each excitation case. This is consistent with the results in section 7.2 and further proves that the flame/acoustic coupling effect can be happened in low excitation frequencies.

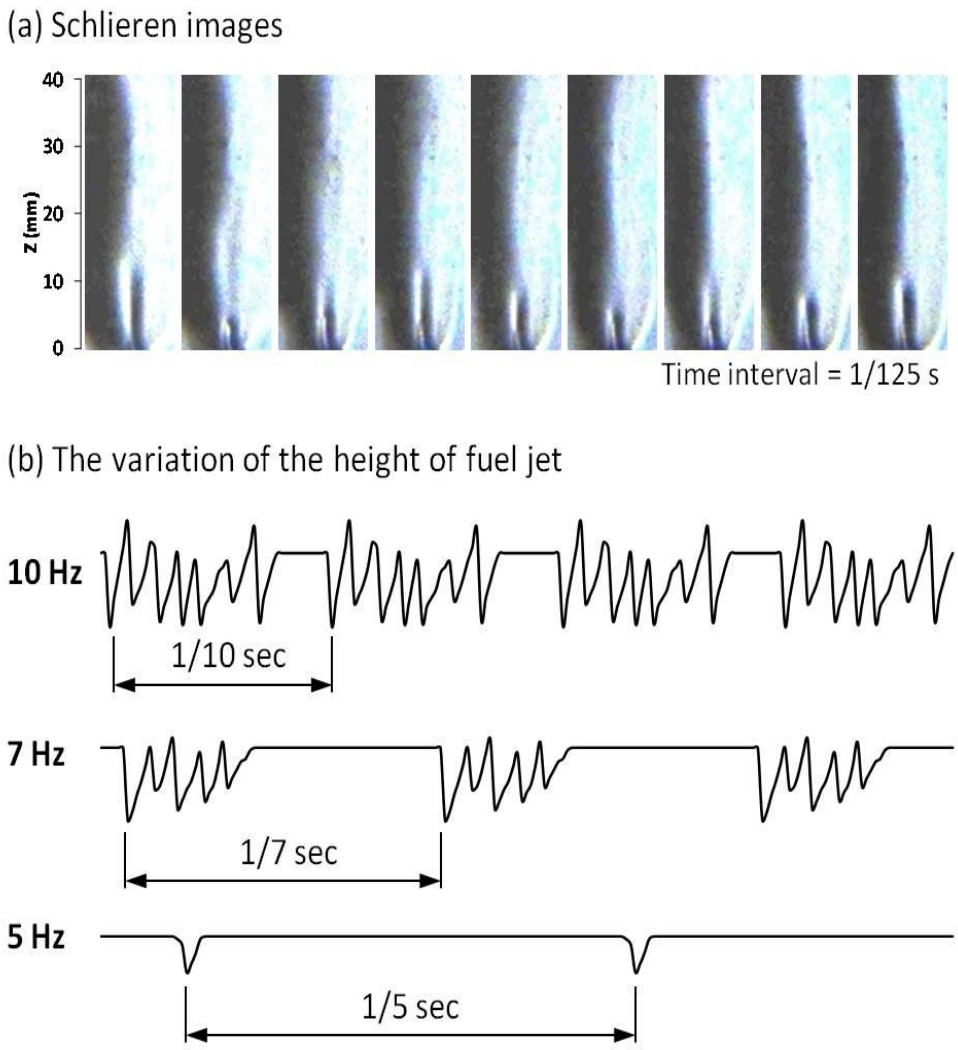

Figure 7.2: (a) Schlieren images at an excitation frequency of 10 Hz with the flame positioned at Z = 600 mm and (b) The variation of the height of the fuel jet.

7.3 Non-Resonant Frequency Effects on the Flame Dynamics

The external excitation effect on a diffusion flame at frequencies between 80 Hz and 210 Hz in the tube was investigated in this study. The visible flame images in Fig. 7.3 show the variation of the flame pattern at acoustic excitation frequencies from 90 Hz to 210 Hz. The case without excitation, which is shown in Fig. 7.3(a), is presented as a reference. It can be seen that the flame height and shape are the same over the 10 image sequence. After triggering the excitation signal, the flame pattern is found to be highly sensitive to the excitation frequency. Results show that the flame is difficult to establish at a frequency of 80 Hz. At frequencies between 90 Hz and 110 Hz the flame is lifted and the bottom of the flame is blue in colour instead of the typical reddish diffusion flame. Afterwards, strong flame flickering is observed at frequencies between 120 Hz and 190 Hz. Interestingly, a very stable flames is observed at an excitation frequency of 200 Hz and then the flame starts to flicker again after a further increase in the excitation frequency as shown in Fig. 7.3b-(i).

Based on the above observation, three test cases at excitation frequencies of 90 Hz, 150 Hz and 200 Hz were chosen for further analysis because they are quite representative of the observed flame dynamics. At 90 Hz acoustic excitation, the flame radiation and spatial distributions showed unstable and lifted, and only the reddish colour flame as clearly visible. At an excitation frequency of 150 Hz, a wavy-shaped flame was observed. The flame necking occurred at the tip and the lower half of the flame was bluish in colour. Further increase of forcing frequency to 200

Hz, the flame became stable again. The flame height and shape remained almost the same as that without excitation.

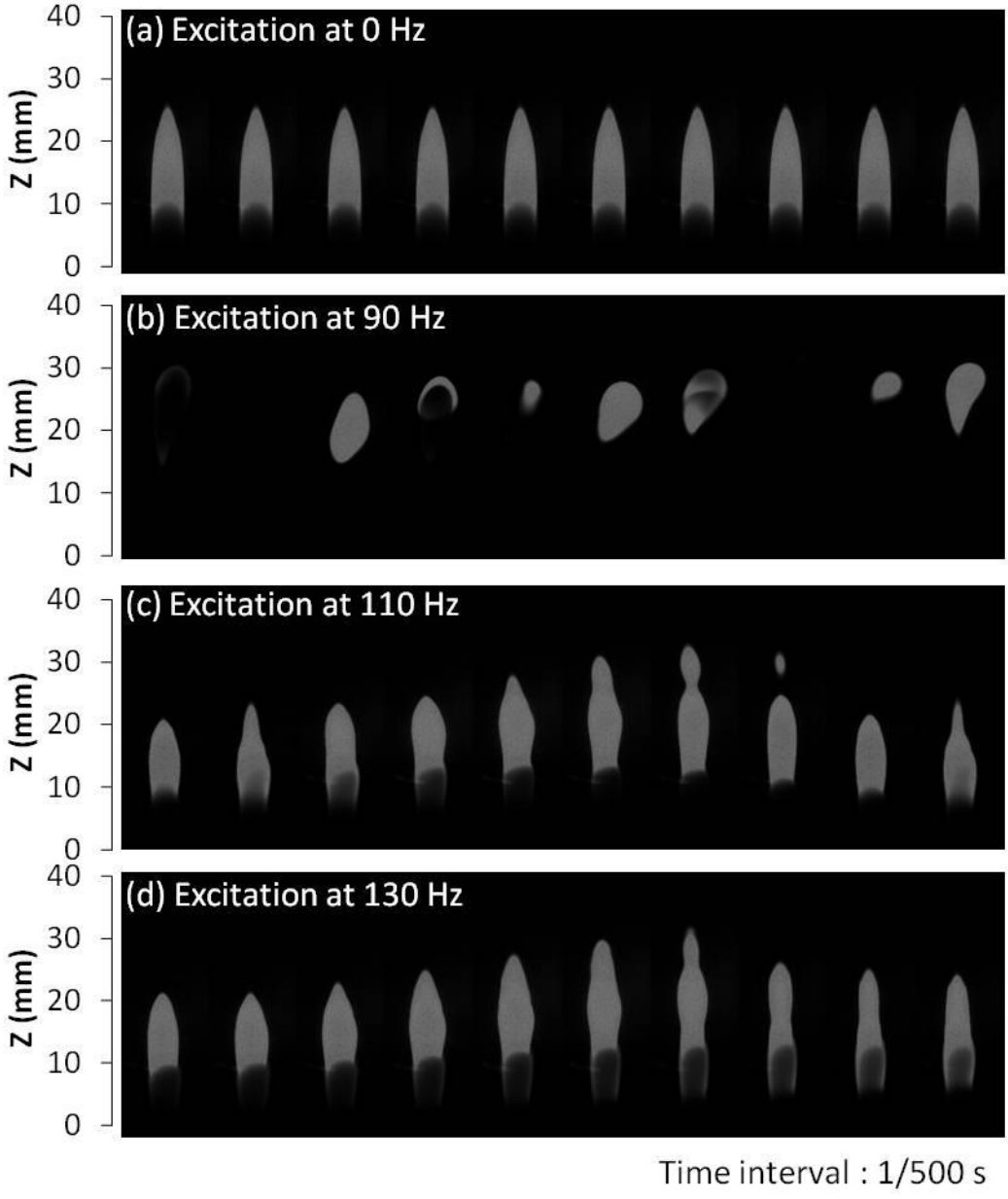

Figure 7.3a: Flame images at acoustic excitation frequencies of 0 Hz, 90 Hz, 110 Hz and 130 Hz.

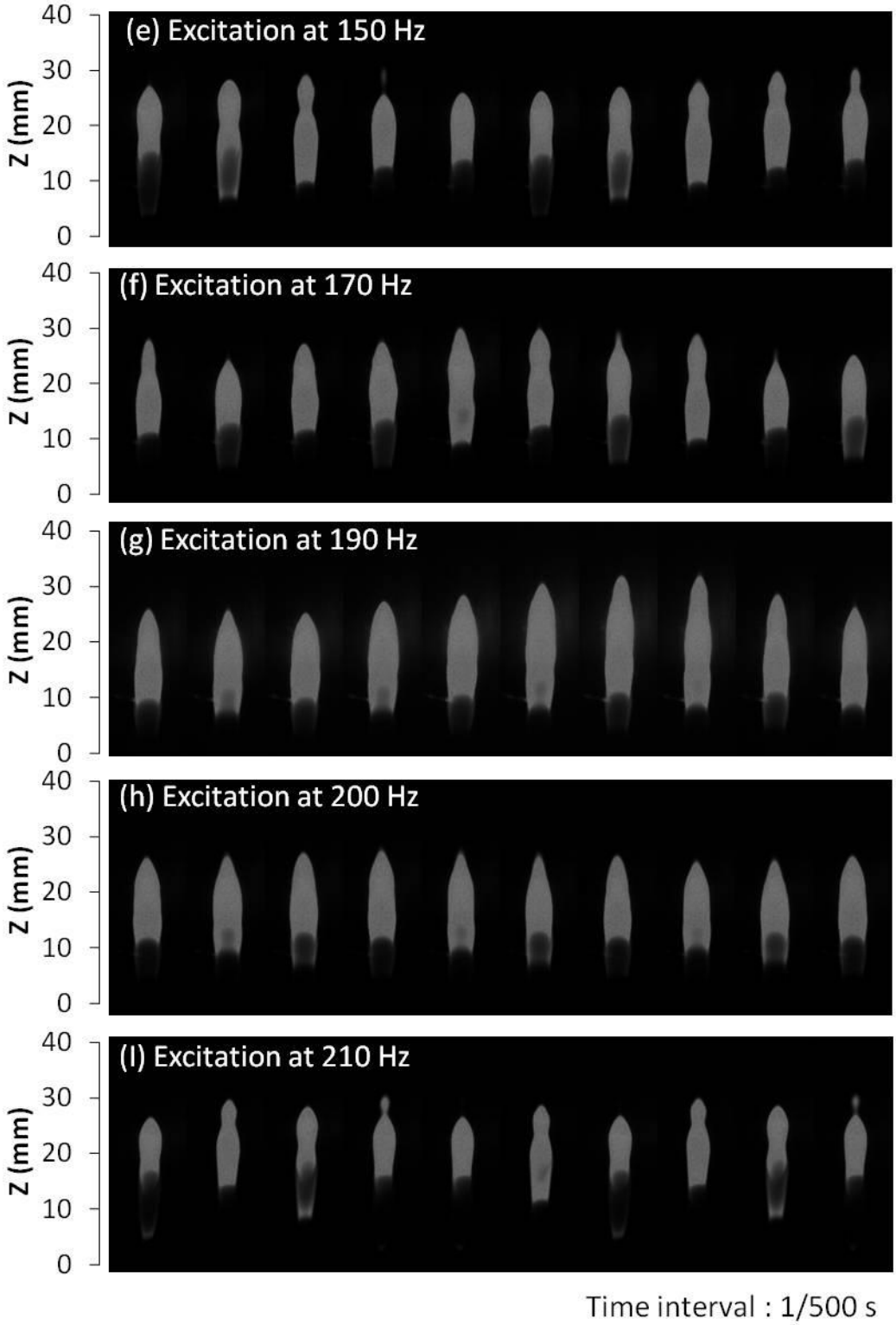

Figure 7.3b: Flame images at acoustic excitation frequencies of 150 Hz, 170 Hz, 190 Hz, 200 Hz and 210 Hz.

The schlieren images of diffusion flames at the three selected acoustic excitation frequencies shown in Fig. 7.4 provide a better visual interpretation on the varying effect of different forcing frequencies. The combustion reacting region and the mixing zones of the hot gases can be observed due to the variation of flow density. A stable and laminar hot gas flow pattern is observed in the case without excitation. Similar to the observation of Fig. 7.3a-(b), the most obvious acoustic effect occurs at 90 Hz, the hot gases are strongly disturbed by the external excitation. At 150 Hz, the hot gas flow is dominated by oscillation vortex structures induced by the cyclic alteration of the burnt gas layer thickness and enhanced local circulation of the surrounding tube atmosphere. By further increasing the excitation frequency to 200 Hz, the pattern of hot gases becomes stable. It can be seen that the hot gases in the lower half of image are very similar to that without excitation.

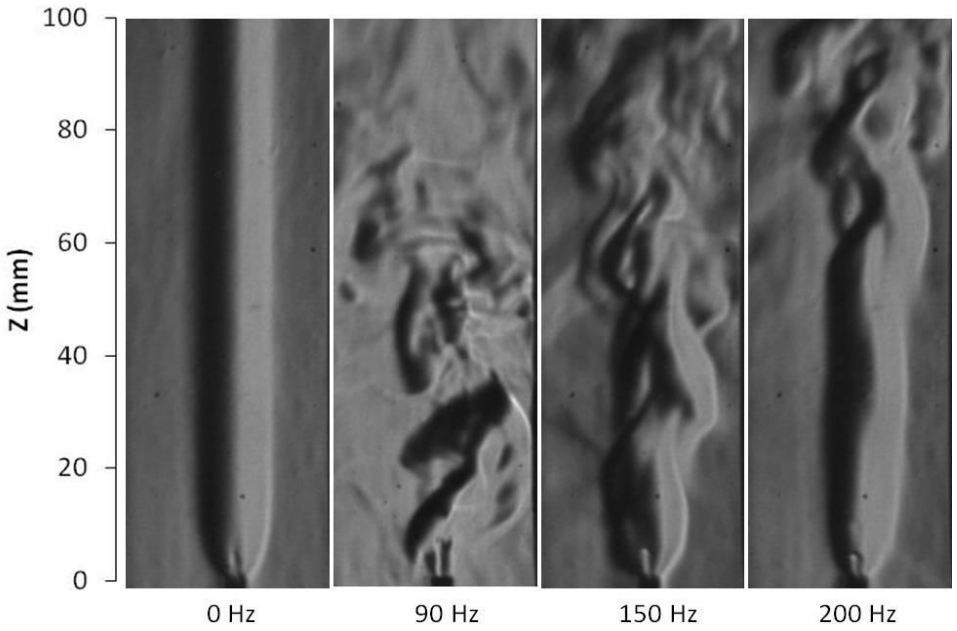

Figure 7.4: Instantaneous schlieren images at excitation frequencies of 0 Hz, 90 Hz, 150 Hz and 200 Hz.

7.3.1 Observation of the Unburnt Fuel Jet

Figure 7.5 shows the zoomed-in schlieren images above the nozzle exit at the three excitation frequencies. The oscillation of the unburnt fuel jet that comes out of the nozzle exit can be observed in each case. At the excitation frequency of 90 Hz, the fuel jet is strongly affected by the acoustic forcing. The unburnt fuel jet cannot even be observed in the first image. After that, the fuel jet flowed strongly and rapidly. The height of the fuel tip reached almost 20 mm above the nozzle exit. Moreover, hot gases detached from nozzle were observed. This phenomenon is consistent with the direct flame images in Fig. 7.3a-(b), where it can be seen that the visible flame zone is a few millimetres above the nozzle exit. At 150 Hz and 200 Hz, the motion of fuel jet showed oscillatory, but it seemed moderate. The height of the unburnt fuel tip was less than 10 mm in each cycle and also the fuel supply was continuous in each excitation cycle. Therefore, the flame is more stable than the case at 90 Hz.

The variation of the height of the unburnt fuel jet is shown in Fig. 7.6. In the case without excitation, the height of the unburnt fuel jet remained the same (around 7.4 mm) in each cycle. After triggering the loudspeaker, the fuel jet was significantly affected by the external excitation. The variation of the unburnt fuel jet was repeatable and followed the external sine-wave signal. Moreover, the fluctuation of the fuel jet became weaker as the excitation frequency increased. At the excitation frequency of 200 Hz, the height of the unburnt fuel jet is only one-third of that at the frequency of 90 Hz.

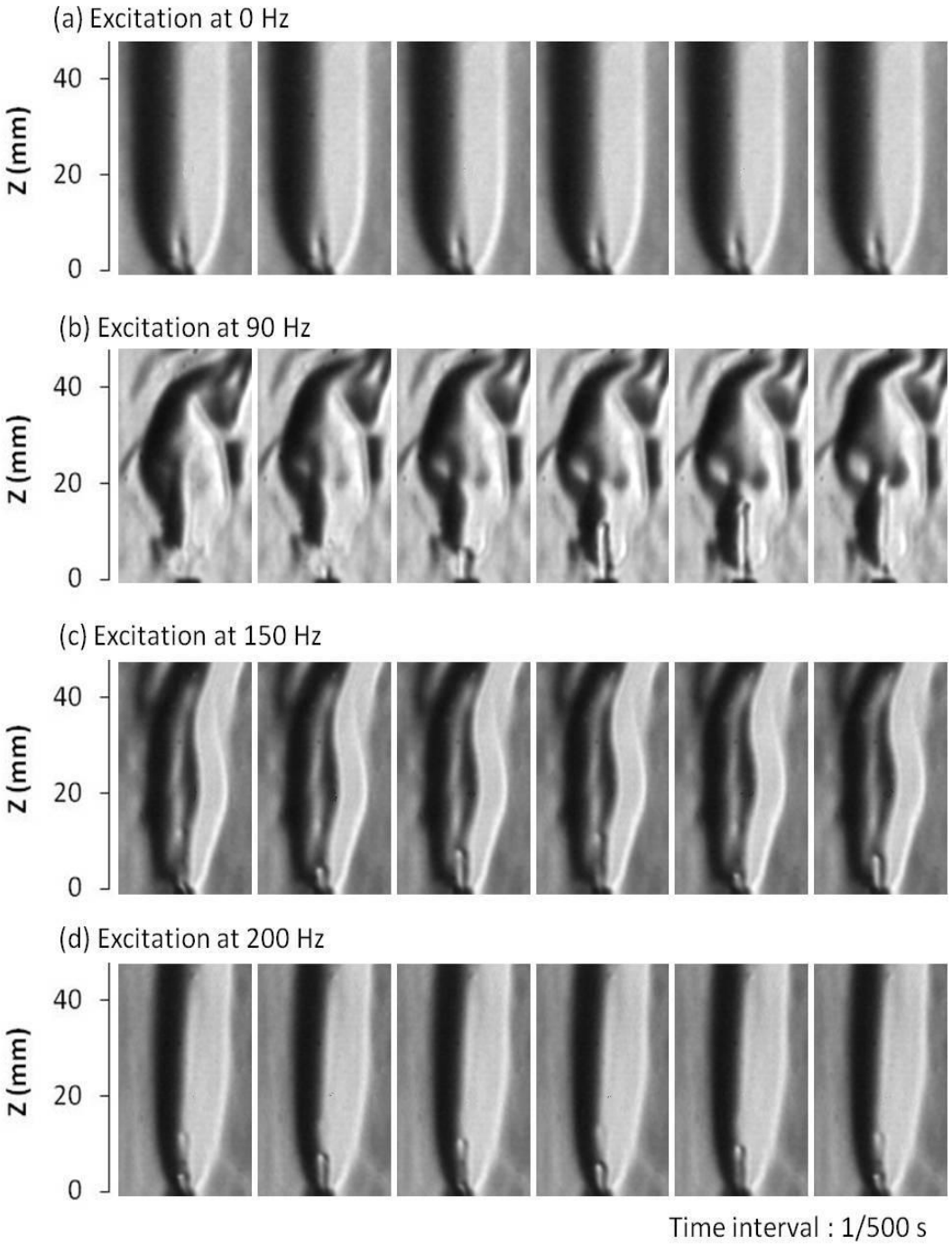

Figure 7.5: The variation of unburnt fuel jet under excitation frequencies of 0 Hz, 90 Hz, 150 Hz and 200 Hz.

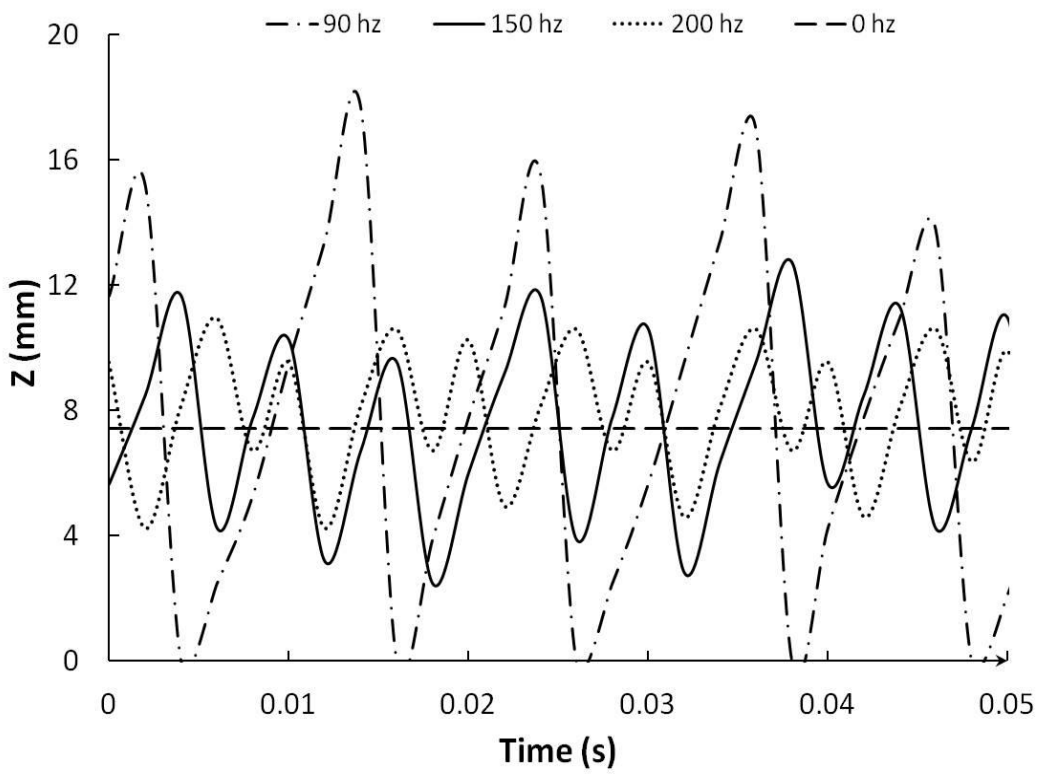

Figure 7.6: The variation of the height of unburnt fuel jet.

Figure 7.7 illustrates the variation in height of the unburnt fuel jet and the comparison with the direct flame images for one excitation cycle for 90 Hz. It is not possible to see the unburnt fuel jet at the first image. This can be explained by the fact that the downward acoustic flow occurred at this moment. The fuel was pushed back into the fuel pipe by the strong reverse acoustic flow. Meanwhile, the air was delivered into the nozzle and provided premixing before the fuel jet exited out again. Then the flame became blue due to the relatively lean combustion condition. After that, the continuous fuel supply increased the equivalence ratio and the flame became non-premixed reaction again. Therefore the flame pattern became stronger and a more yellowish diffusion flame was observed. At the end of

each excitation cycle, the fuel jet is gradually diluted by the combustion reaction. Hence the flame became weaker and bluer due to the lack of fuel supply. The result is consistent with the studies of Demare and Lakshminarasimhan [43, 46]. They mentioned that the reverse flow, which was created by the acoustic wave, provides premixing before the fuel jet is expelled again and so enhances the combustion efficiency. But, in their experiment only the fuel was excited acoustically.

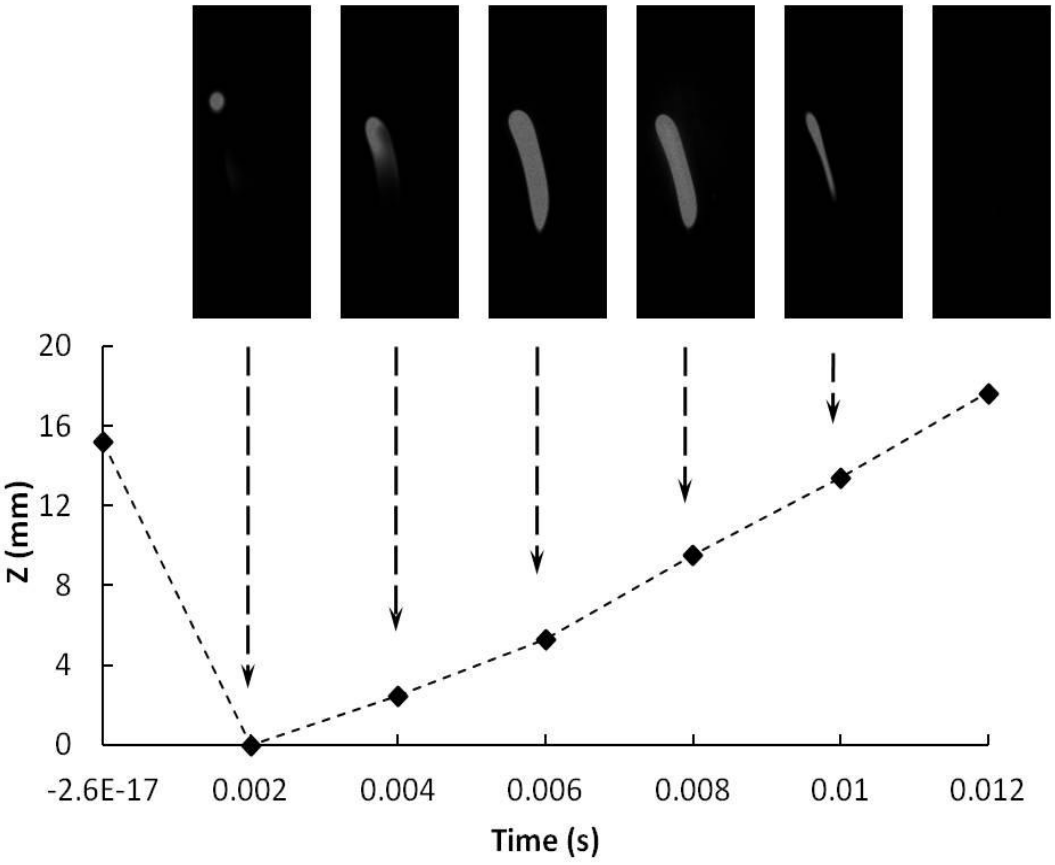

Figure 7.7: Flame images at different heights of the unburnt fuel jet at one excitation cycle of 90 Hz.

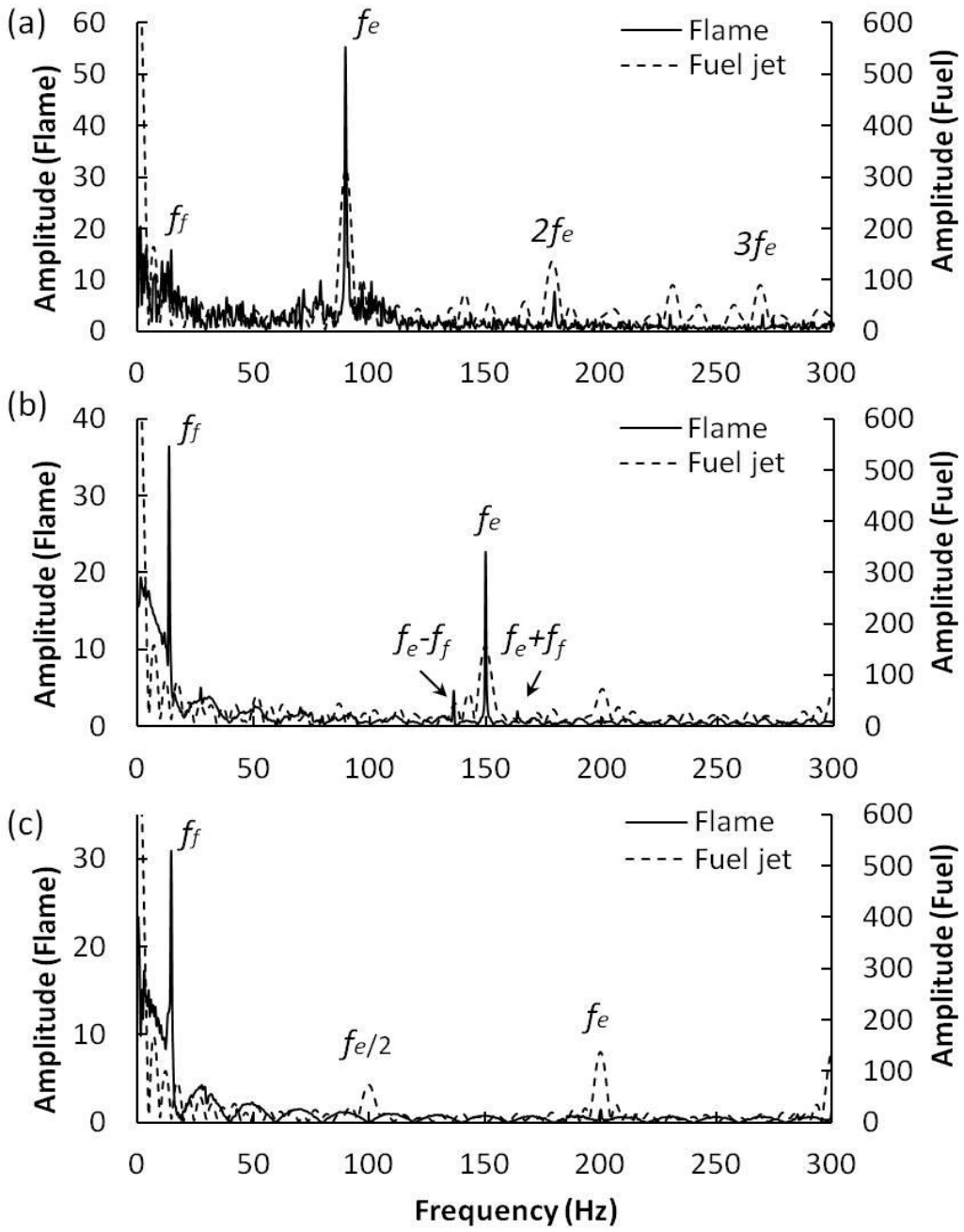

Figure 7.8: Frequency analysis of flame and fuel jet oscillation, (a) Excitation at 90 Hz, (b) Excitation at 150 Hz and (c) Excitation at 200 Hz.

Figure 7.8 shows the frequency analysis of the oscillation of the visible flame (solid line) and fuel jet (dash line). For the case of visible flame, the peak frequency not only is the same as the excitation frequency (f_e) but also has the strongest power

spectrum density at the excitation frequency of 90 Hz. Also, harmonic doubling of external excitation is observed at $2f_e$ = 180 Hz and $3f_e$ = 270 Hz. At the excitation frequency of 150 Hz, both the excitation frequency (150 Hz) and the flame natural flickering frequency (≈14 Hz) peaks are observable. Zoomed into the excitation frequency peak region, two small peaks are found, which exhibit a relationship of $f_e \pm f_f$. At the excitation frequency of 200 Hz, the dominant frequency peak is the natural flickering frequency, but a small peak of the acoustic excitation frequency is still observed and also the sub harmonic frequency of the acoustic excitation frequency (f_e/2) is visible at 100 Hz. Comparing the three excitation frequencies, the amplitude of the external excitation frequency decreased significantly when the frequency was increased from 90 Hz to 200 Hz. In contrast, the amplitude of the natural flickering gets stronger. The results demonstrate the nonlinear flame/acoustic coupling. For the case of the unburnt fuel jet, the figures show that the oscillating frequency follows the excitation frequency and the amplitude gets weaker from 90 Hz to 200 Hz. The result corresponds to the oscillation of the flame behaviour shown in Fig. 7.3.

7.3.2 PIV Examination of Flame Flow Fields

The acoustic flow fields generated by the acoustic excitation can be examined by PIV measurements. Figure 7.9 shows the phase-locked velocity vectors and vorticity contour maps of the velocity fields at the three acoustic excitation frequencies. In the X-axis of each contour map, the flow velocity is higher because of the existence

of the jet flame. Moreover, the upward flow motion is further accelerated by the buoyancy effect of the flame. The maximum flow velocity is observed at the phase angle of 90°. At the phase angle of 180° and 270°, the flow patterns at the three excitation frequencies are very different. The flow motion was observed to turn downward at the frequency of 90 Hz. The buoyancy effect of the flame was suppressed by the strong downward acoustic flow at the phase angle of 270°. However, at the frequency of 150 Hz, the downward acoustic flow only slightly affects the flame flow motion. Meanwhile, acoustic excitation has almost no effect on the flow field at the frequency of 200 Hz. Only a few downward velocity vectors can be observed, hence the strong upward flame flow velocity is clearly seen above the fuel nozzle over the four presented phase angles. The results illustrate that the intensity of acoustic flow velocity is different for each excitation frequency. Therefore, the flame behaviour is very different in each case.

The vorticity contours in Fig.7.9 illustrate that its intensity correlates well with the flame shape. At frequency of 90 Hz, many disordered positive and negative vorticities are observable at each phase angle. The upward hot gas is broken up by the up-and-down flow motion of acoustic flow field. These local opposite direction flows then form many little vortices due to the effect of Kelvin-Helmholtz instability. At 150 Hz, the disordered positive and negative vorticities distribution becomes regular. After increase the frequency to 200 Hz, the distribution of strong vorticity is observed on both sides of the X-axis at each phase angle. The positive vorticity is

shown on the left hand side and the right hand side is negative. This is because the external excitation effect on the flame is small at this frequency. The stable and strong upward flame jet creates large velocity gradient with ambient flow and form the strong vorticity.

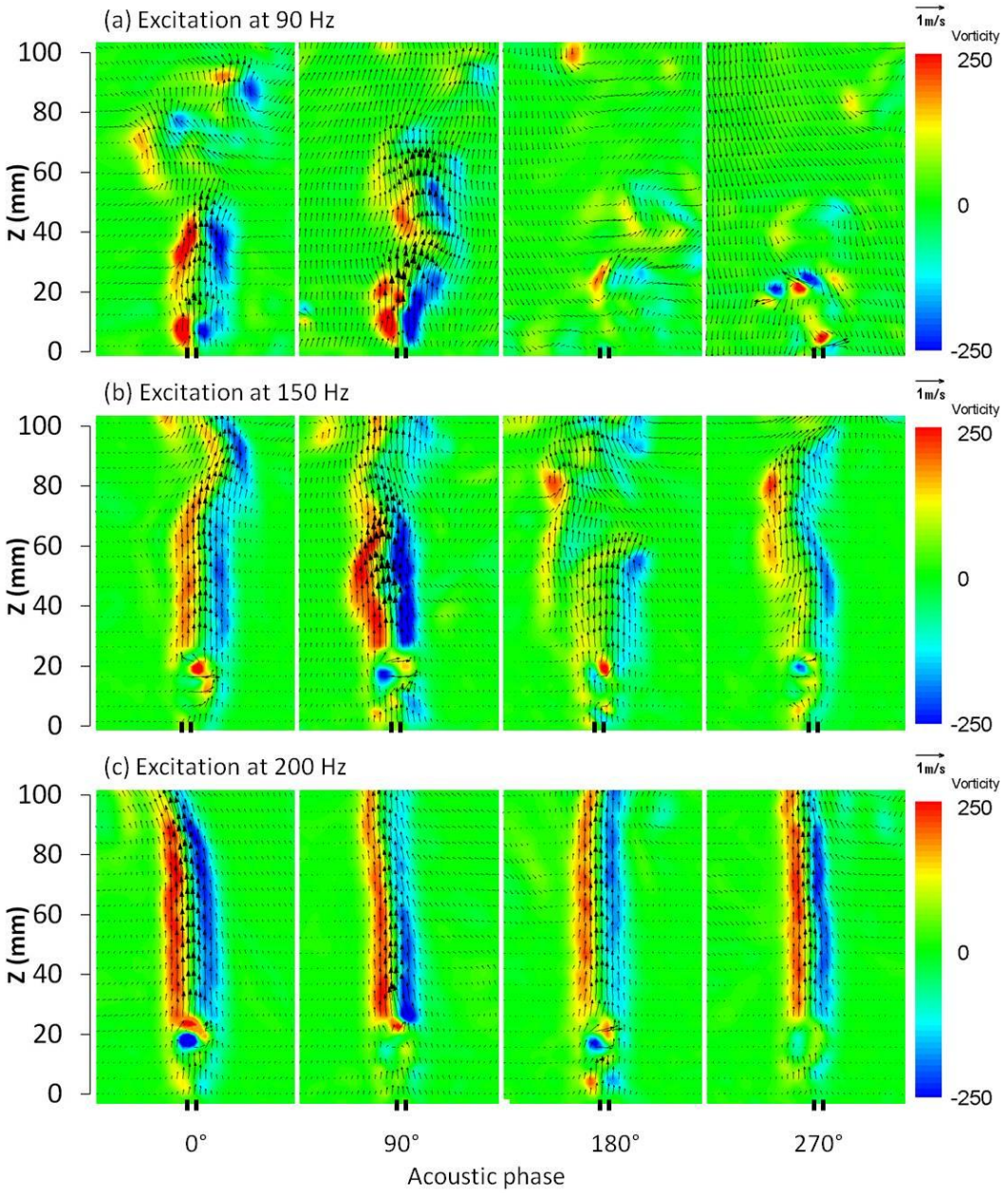

Figure 7.9: Phase-locked vorticity contours and velocity vectors of instantaneous diffusion flame flow at acoustic excitation frequencies of 90 Hz, 150 Hz and 200 Hz.

Figure 7.10 shows the overall turbulence intensity contour and velocity vectors of the diffusion flame jets. The results are calculated from 120 ensemble averaged PIV images. In the case without excitation, the turbulence intensity is low. It can be seen that the flame is very stable and only generated some turbulence in the centreline region. After trigger the excitation signal, it is observed that both the flame behaviour and surrounding air are affected by acoustic excitation. Above the nozzle exit, due to the variation of acoustic flow velocity, combined with the buoyancy effect, particularly stronger turbulence intensity was observed over the three excitation frequencies. The turbulence intensity is higher at the excitation frequency of 90 Hz than that at 150 Hz and 200 Hz. The highly variation of flame increases the turbulence intensity at the shear layer of the flame jet. It can also be seen that the velocity fluctuation created by the acoustic excitation is stronger at 90 Hz. In the case of 150 Hz and 200 Hz, strong turbulence intensity is observed above the flame tip due to the flame flickering behaviour that is created at this excitation frequency. Yet the turbulence intensity is lower both in the surrounding area and above the flame at the frequency of 200 Hz. It can be seen that the external forcing only slightly affects the flow behaviour at 200 Hz. The velocity vectors also show that the flow velocity can be reached to 1.34 m/s at 200 Hz. The vaule only 9% lower than the case that without excitation, but it is 2.3 times higher than that at 90 Hz. This can be explained by the fact that the upward flame hot gas flow is slightly affected by the external forcing at 200 Hz. However, at 90 Hz the strong up-and-down flow motion significantly reduce the averaged flow velocity. Note that the seeding density is too low to calculate the result in the bottom area of flame.

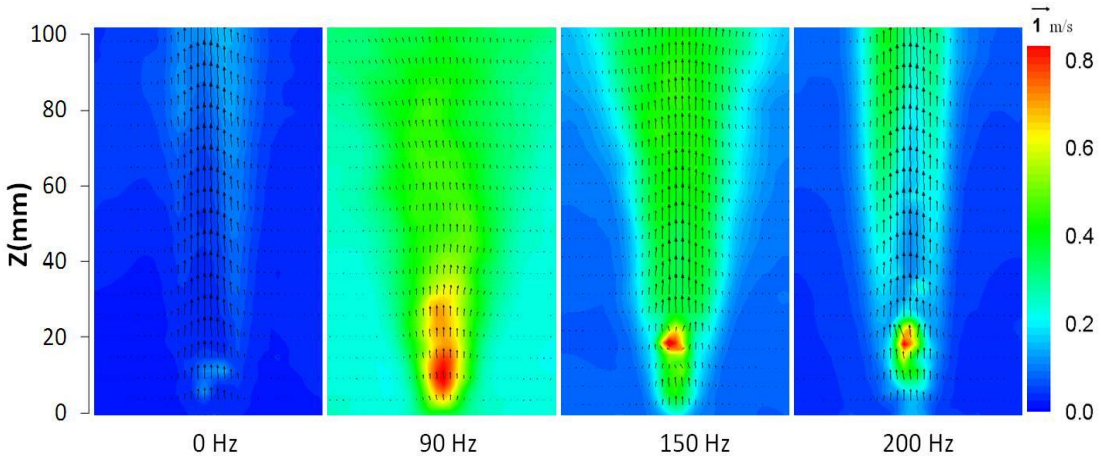

Figure 7.10: Turbulence intensities of the diffusion flame flow at acoustic excitation frequencies of 0 Hz, 90 Hz, 150 Hz and 200 Hz. The result was calculated from 120 sequential PIV images. Note that the seeding density is too low to calculate the result in the flame area.

7.3.3 Theoretical Analysis of the Acoustic Field in the Tube

Theoretical acoustic model of the tube has been discussed in the chapter 4. According to the formulas, the acoustic velocity field in the tube at excitation frequencies of 90 Hz, 150 Hz and 200 Hz were calculated and shown in Fig. 7.11. The output of voltage amplitude of acoustic signal was set at 33 V in all three cases. At Z = 1.1m, the results showed that the velocity at 90 Hz was much stronger than that the other excitation frequencies. Then, the velocity intensity was reduced to the lowest at 150 Hz and then slightly increased again at 200 Hz. The velocity value at 90 Hz is 2.54 times and 1.83 times higher than that at 150 Hz and 200 Hz respectively. It can be seen that the same voltage amplitude of acoustic signal can produce different level of acoustic intensity in different frequencies and also can be explained the reason why the flame flow field showed the most unstable at 90 Hz.

For the excitation frequencies of 150 Hz and 200 Hz, the velocity intensity at 150 Hz is smaller than that at 200 Hz. Yet the flame behaviour at 200 Hz is more stable than that at 150 Hz. This is because of the pyramidal structure changes the characterisation of acoustic wave. The velocity node is formed at these frequencies. At the excitation frequency of 200 Hz, the velocity node region is almost the same as nozzle position B. The relative small velocity oscillation resulted stable flame behaviour. The results further proved that the importance of flame positions and frequencies in the research area of thermoacoustic instability.

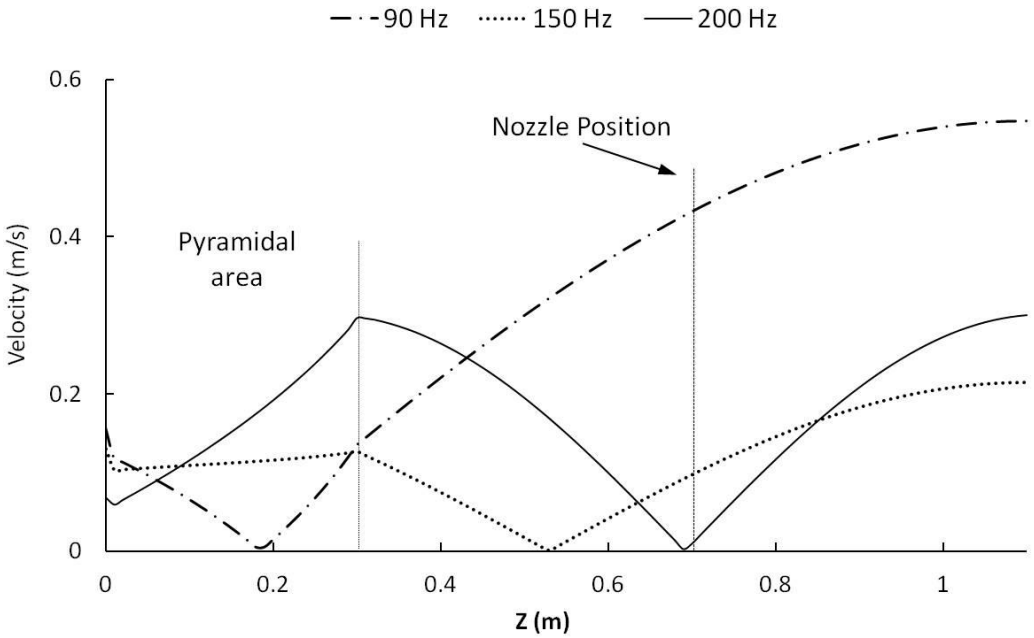

Figure 7.11: The theoretical prediction of acoustic velocity field of the tube at excitation frequency of 90 Hz, 150 Hz and 200 Hz.

7.4 Summary

Excitation frequency effects on the flame behaviour were studied in this chapter. At frequencies below 20 Hz (infrasound), the visible flame pattern seemed turbulent, but the oscillation of the fuel jet was found to follow the excitation frequency. At non-resonant frequencies, results indicated that the flame dynamics were affected by the forcing frequency. The flame patterns and luminosity of the acoustically excited diffusion flames were very different in each excitation case. It was observed that the lower excitation frequency of 90 Hz has the strongest effect on the flame dynamics. Both the fuel jet flow and ambient air motion were strongly affected. At the excitation frequency of 150 Hz, the external excitation effect on the surrounding area was low and the buoyancy-driven flickering starts to dominate the flame oscillation behaviour. Under the higher acoustic excitation of 200 Hz, only the fuel jet was slightly affected by external forcing. The frequency analysis also showed that flame/acoustic interaction results in a nonlinear coupling effect between the buoyancy driven instability and the acoustic disturbance. The theoretical acoustic model showed that the strongest velocity oscillation exist at 90 Hz and has the weakest velocity intensity at 150 Hz. At 200 Hz, the node region was the same as measure position. These acoustic characterisations matched well with the abovementioned experimental observations.

Chapter 8

Conclusions and Future Work

8.1 Conclusions

A phase-locked PIV system combined with a high speed schlieren visualisation system and a chemiluminescence emission measurement system were applied to investigate the flame flow characteristics in an acoustically excited tube. The major contributions of the present experimental investigation are summarised in the following paragraphs.

1. The experimental system, using PIV diagnostics, a schlieren visualisation system and the chemiluminescence emission measurement system for the examination of flame-acoustic interactions, was designed and built together with a signal synchronisation system, which enables the phase-locked observation, was developed successfully. A square tube was designed to facilitate the PIV and schlieren measurement in order to avoid the reflection from the curved surface. The theoretical acoustic model has been developed

to analyse the acoustic response for the present square tube and acoustical system. A good agreement between experimental measurements and theoretical predictions were proved by measure the pressure fields of acoustic wave. The first four measured harmonic frequencies match well with theoretical prediction. The measured acoustic pressure node and anti-node region was also the same as theoretical prediction. However, due to the neglect of pressure drop loss in the upper end of the tube, the theoretical predict pressure data was 23 % to 43.3 % higher than that the experimental measurements. The accuracy of synchronisation system was checked by a simple experiment. A phase-locked PIV results showed that the acoustic velocity difference was less than 2.8% at specific phase angle over 1,000 excitation cycles. Regarding the preparation works for the PIV, the seeding method and PIV data analysis were discussed. Due to the difficulty of deliver seeding particles from tiny fuel pipe and the low acoustic wave energy, inject the seeding into an enclosed system was chosen in this experiment. The classical Reynolds decomposition method was applied to decide the number of PIV sample to calculate the turbulent flow behaviour. Result shows that a good convergence data was reached at around 120 images.

2. According to the theoretical predict frequency response of the tube, third harmonic frequency was chosen as main test frequency. Under this excitation frequency, the velocity distributions of acoustic standing wave

flow along the tube were measured. The cold jet flow and flame behaviour inside a standing wave tube has also characterised. The results indicate that the acoustic node and anti-node regions significantly affected the flow motion in the tube. Both the cold fuel jet flow and the flame pattern were affected strongly when measured at the different phase angles and at different positions in the tube. In the velocity node region, the fuel jet flow is more or less stable. However, in the velocity anti-node region, the flow fluctuation reaches a maximum and strong reverse fuel flow was observed at a phase angle of around 216°, where the jet characteristics were completely blurred by acoustic wave. In comparison with the flame case, the flow fluctuation was observed clearly in the velocity anti-node region where the flame flickering becomes stronger due to strong acoustic flow field. In the velocity node regions, the flame height and shape were maintained at almost the same values as those without excitation. It can be seen that under the acoustic excitation, the flame behaviour was affected by both the variation of the ambient air motion and the acoustically induced fluctuation of the jet fuel flow. Particularly, strong correlation between local flame and vorticity generation was observed. The flame and acoustic wave interactions generate stronger vortices than the cases of cold flow but these vortices do not necessarily produce stronger vorticity. The study indicates that both the spatial variation and phase angle of a strongly oscillating acoustic field have to be considered in the investigation of flame and acoustic wave coupling. For the case of the hydrogen flame, the flame oscillation behaviour was

observed to be weaker than that of a hydrocarbon flame under the same excitation perturbation. However, the mushroom-shaped hot gas pattern is shown in the schlieren images and this indicates that acoustic wave still has a large influence on the flame, but the high velocity of initial fuel jet and high burning velocity are able to resist the downward acoustic flow in the jet region. Hence, the flame is only observed to be slightly shorter and thinner, with a wavy-shaped surface, under external forcing. The PIV results demonstrate that the largest downward acoustic flow is not strong enough to reverse the upward flame flow. Therefore no downward flame flow was detected at any excitation phase angle.

3. The nonlinear coupling of flame dynamics and acoustic excitation in an acoustically excited standing wave tube was systematically investigated using a chemiluminescence emission measurement system. The frequency analysis of the flame oscillation indicated that flame/acoustic coupling behaviour could result in nonlinear flame dynamics. In the acoustic velocity anti-node region, both the flame natural flickering and excitation frequency dominated the flame behaviour for a diffusion flame at 0.3 V. In the case of the premixed flame, excitation forcing was the only factor to affect the flame dynamics and no coupling behaviour was detected at such a low intensity. After raising the voltage amplitude to 2 V, the excitation frequency (f_e) was accompanied by the nonlinear fore and aft frequency peaks. In the premixed flame, such complementary frequency peaks are shown in a

relationship of $f_e \pm f_e/5$. In the case of the diffusion flame, the study found that the excitation frequency could be coupled with both the sub-harmonic frequency of the excitation frequency ($f_e/5$) and the natural flame oscillating frequency (f_f). At the higher excitation intensity, the natural frequency and sub-harmonic frequencies ($2f_e/5$ and $3f_e/5$) could be enhanced. Then these sub-harmonic frequencies may couple with the flame natural oscillating frequency again and create complex nonlinear frequency components. The study also demonstrated that the complex flame response is consistent with the nonlinear theory and the observed frequency peaks are not random but are the nonlinear coupling modes of the excitation source and the flame instability oscillation. For a practical combustion device such as a gas turbine combustor, it is worth making the effort to study the various frequency peaks and identify their inter links. A phase-locked PIV system was applied to investigate the flow characteristics of a propane-air flame. The results showed that acoustic excitation effect on the flame dynamics gets weaker with increasing air-fuel flow rate, due to the combination of the initial flow velocity and the buoyancy effect of the flame aiding the resistance of the acoustic perturbation. Therefore, the chaotic flow pattern is only found in the diffusion flame. In this case, the initial fuel velocity is low and the flame hot gas flow basically follows the oscillation of the acoustic flow field. The vorticity contour maps were found to match well with velocity data, due to the acoustic flow and hot gas flow create opposite velocity and formed strong vorticity. It is hoped that this study will stimulate further

investigations into the complex nonlinear couplings of flame and acoustics using different methodologies and diagnostic techniques.

4. The behaviour of diffusion flames in a variety of excitation frequency was examined. The infrasound effect on the air motion and flame pattern was irregular. The flame oscillating frequency still followed the excitation frequency because of the excitation effect on the fuel jet. For excitation frequencies of 90 Hz, 150 Hz and 200 Hz, which are between first and second resonant frequencies (65 Hz and 220 Hz respectively), the strongest acoustic effect was observed at 90 Hz. Both the fuel jet flow and ambient air motion were significantly affected by the external excitation in this test case. Flow characterisation has shown that many disordered positive and negative vorticities are observable at each phase angle and the flow motion was even reversed at both near the nozzle exit and the surrounding area at the phase angles of 180° and 270°. At the excitation frequency of 150 Hz, the external excitation effect on the surrounding area was low and only weak reverse flow was observed at the phase angle of 270°. On the other hand, the buoyancy-driven flickering starts to dominate the flame oscillation behaviour at this frequency. At the excitation frequency of 200 Hz, the flame became stable at each phase angle. There is no obvious evidence to show that the ambient air was affected by the acoustic excitation. The only effect is the slight oscillation of the fuel jet flow created by the external excitation. The frequency analysis of flame oscillation indicates that flame/acoustic

coupling behaviour could result in nonlinear effect on the flame dynamics. At 90 Hz, the excitation frequency and its harmonic frequencies dominated the flame dynamics. At 150 Hz, the excitation frequency and flame natural flickering and their coupling phenomenon affected the flame behaviour. At 200 Hz, the excitation effect on the flame became small and the dominate frequency was changed to flame natural flickering. The results show that acoustic excitation effect on the flame dynamics in a tube is a strong function of the non-resonant frequencies. The theoretical acoustic model shows that the strongest velocity fields were observed at 90 Hz and the weakest influence was observed at 150 Hz. At 200 Hz, the velocity node region is the same as the flame position. Therefore, the most unstable flame behaviour was observed at 90 Hz. In contrast, the flame is stable as that without excitation at 200 Hz.

To sum up, this investigation has shown that the acoustic characterisation and its excitation frequencies influence on the air motion and fuel jet flow significantly. The coupling between them further induces unstable flame behaviour. These findings enhance the understanding of the correlation between acoustic excitation and flame dynamics. Also, theoretical acoustic predictions match well with experimental measurements both in resonant and non-resonant excitation cases. The results of their influence on the flame proved that the flame stabilisation in the simple combustion chamber is possible to be predicted using theoretical acoustic model.

8.2 Future Work

From the findings and experience gained in this experimental investigation, the recommendations for future works are listed below:

- A simple straight square tube with pyramidal structure in the low half of the tube was adopted to simulate a combustion chamber in the present study. The visualised acoustic flow field and its effect on the flame dynamic were examined clearly. However, in practical applications, the complex geometry of combustion chamber creates many acoustic reflections during operation processes. These reflections could induce more uncertain thermoacoustic instability phenomena. Therefore, to build a variant boundary of test tubes in order to diagnose the geometry effect on the acoustic reflections and flame behaviour is recommended for future research.

- The change of chamber pressure and its effect on the flame was not considered in the present study. However, the operating pressure is high and may be changeable in the practical application, and therefore the study of flame-acoustic interactions under variant pressures is recommended.

- The appearance of harmonic frequencies in the test tube was found to be very sensitive to the tube location in the laboratory and also to the different laboratory itself (two different laboratories were used for the experimentation). The harmonic frequency effect on the flame and the oscillating behaviour of flame were also slightly different. Designing a

systematic experiment to investigate the room space, ambient temperature, humidity and the initial fuel gas temperature effect on the flame/acoustic interaction would be another interesting topic in the research field of thermoacoustic instabilities.

- According to the frequency analysis of the flames, the excitation frequency, natural flickering frequency, harmonic and sub-harmonic frequency could all exist in one excited flame case. It could be seen that different parts of flame exhibited different oscillating frequencies. Measuring the frequency for each part of flame could help in further understanding the external forcing effect on the flame structure.

- The highest laser pulse rate of the present PIV system was only 7.25 Hz. This low pulse rate limited the possibility to observe the detailed time resolved flame flow behaviour under the higher excitation frequency. Therefore, it is recommended to use a high speed PIV system in order to obtain a better understanding of the flame and acoustic wave interaction.

- The seeding method adopted in this study was to inject seeding particles into an enclosed environment. As a result, the flow dynamics near the fuel nozzle are difficult to measure. Also, the lack of seeding density control and the short experimental operation timing limited the application of the PIV system. Therefore, improving the seeding system, and using a better seeding generator for this application are highly recommended.

- The PIV experiment was successfully applied to observe the flame behaviour under an acoustic excitation in a laboratory scale burner. However, it would be worth designing a suitable PIV experimental system to diagnose the flame/acoustic interaction in a practical combustion chamber.

References

[1] D. Price, *Energy and human evolution,* Population and Environment, 16 (1995) 301-319.

[2] *Key World Energy Statistics 2010*. 2010, International Energy Agency: Paris, France.

[3] D. P. Mishra, *Fundamentals Of Combustion* PHI, New Delhi, 2008.

[4] K. R. McManus, T. Poinsot and S. M. Candel, *A review of active control of combustion instabilities,* Prog. Energy Combust. Sci., 19 (1993) 1-29.

[5] S. Rea, S. James, C. Goy and M. J. F. Colechin, *On-line combustion monitoring on dry low NOÏ‡ industrial gas turbines,* Meas. Sci. Technol., 14 (2003) 1123-1130.

[6] A. J. L. V. Chris G. James, *Dynamic Pressure Monitoring in Gas Turbines*. 2002, Dymac and KEMA: San Diego.

[7] K. T. Feldman Jr, *Review of the literature on Rijke thermoacoustic phenomena,* J. Sound Vibrat., 7 (1968) 83-89.

[8] A. H. Lefebvre, *Pollution control in continuous combustion engines,* Symposium (International) on Combustion, 15 (1975) 1169-1180.

[9] T. P. K.R. McManus, S.M. Candel, *A review of active control of combustion instabilities,* Prog. Energy Combust. Sci., 19 (1993) 1-29.

[10] Christian Oliver Paschereit, Ephraim Gutmark, and Wolfgang Weisenstein, *Control of thermoacoustic instabilities and emissions in an industrial-type gas-turbine combustor* Symp. (Int.) Combust., 27 (1998) 1817-1824

[11] A. M. Annaswamy and A. F. Ghoniem, *Active control of combustion instability: Theory and practice,* IEEE Control Systems Magazine, 22 (2002) 37-54.

[12] W. S. Song, S. Lee and D. S. Shin, *Prediction of thermoacoustic instability in Rijke tube using CFD-CAA numerical method,* Journal of Mechanical Science and Technology, 25 675-682.

[13] K. W. R. Gary L. Borman, *Combustion Engineering*, McGraw-Hill, Singapore, 1998.

[14] U. M. J. Warnatz, Robert W. Dibble, R. W. Dibble, *Combustion: physical and chemical fundamentals, modeling and simulation, Experiments, Pollutant Formation*, Springer, Berlin, 2006.

[15] A. J. Ihde, *The development of modern chemistry*, General publishing company, Toronto, 1984.

[16] T. Echekki and J. H. Chen, *Unsteady strain rate and curvature effects in turbulent premixed methane-air flames,* Combust. Flame, 106 (1996) 184-202.

[17] H. C. Hottel and W. R. Hawthorne, *Diffusion in laminar flame jets,* Symposium on Combustion and Flame, and Explosion Phenomena, 3 (1949) 254-266.

[18] D. A. Scholefield and J. E. Garside, *The structure and stability of diffusion flames,* Symposium on Combustion and Flame, and Explosion Phenomena, 3 (1949) 102-110.

[19] G. Kelsall and C. Troger, *Prediction and control of combustion instabilities in industrial gas turbines,* Appl. Therm. Eng., 24 (2004) 1571-1582.

[20] N. Docquier and S. b. Candel, *Combustion control and sensors: a review,* Prog. Energy Combust. Sci., 28 (2002) 107-150.

[21] N. Noiray, D. Durox, T. Schuller and S. Candel, *Dynamic phase converter for passive control of combustion instabilities,* Proc. Combust. Inst., 32 (2009) 3163-3170.

[22] N. T. Davis and G. S. Samuelsen, *Optimization of gas turbine combustor performance throughout the duty cycle,* Symp. (Int.) Combust., 26 (1996) 2819-2825.

[23] B.-S. Hong, A. Ray and V. Yang, *Wide-range robust control of combustion instability,* Combust. Flame, 128 (2002) 242-258.

[24] W. C. Strahle, *Combustion noise,* Prog. Energy Combust. Sci., 4 (1978) 157-176.

[25] I. E. J. H. Whitelaw, *Control of combustion oscillations,* Combust. Sci. Technol., 175 (2003) 157 - 184

[26] M. R. Bothien, J. P. Moeck and C. Oliver Paschereit, *Active control of the acoustic boundary conditions of combustion test rigs,* J. Sound Vibrat., 318 (2008) 678-701.

[27] F. E. C. Culick, *A Note on Rayleigh's Criterion,* Combust. Sci. Technol., 56 (1987) 7.

[28] T. Y. Toong, S. Richard F, S. John M and A. Griffin Y, *Mechanisms of combustion instability,* Symp. (Int.) Combust., 10 (1965) 1301-1313.

[29] P. G. Drazin and W. H. Reid, *Hydrodynamic Stability*, second, Cambridge university press, Cambridge, 2004.

[30] A. Lingens, K. Neemann, J. Meyer and M. Schreiber, *Instability of diffusion flames,* Symp. (Int.) Combust., 26 (1996) 1053-1061.

[31] G. Papadopoulos, R. Bryant and W. Pitts, *Flow characterization of flickering methane/air diffusion flames using particle image velocimetry,* Experiments in Fluids, 33 (2002) 472-481.

[32] B. M. Cetegen and Y. Dong, *Experiments on the instability modes of buoyant diffusion flames and effects of ambient atmosphere on the instabilities,* Exp. Fluids, 28 (2000) 546-558.

[33] G. W. Swift, *Thermo acoustic engines and refrigerators,* PhT, 48 (1995) 22-28.

[34] R. L. Raun, M. W. Beckstead, J. C. Finlinson and K. P. Brooks, *A review of Rijke tubes, Rijke burners and related devices,* Prog. Energy Combust. Sci., 19 (1993) 313-364.

[35] M. Q. McQuay, R. K. Dubey and J. A. Carvalho, *The effect of acoustic mode on time-resolved temperature measurements in a Rijke-tube pulse combustor,* Fuel, 79 (2000) 1645-1655.

[36] P. Chatterjee, U. Vandsburger, W. R. Saunders, V. K. Khanna and W. T. Baumann, *On the spectral characteristics of a self-excited Rijke tube combustor--numerical simulation and experimental measurements,* J. Sound Vibrat., 283 (2005) 573-588.

[37] T. Papadopoulos, M. Pritchard, C. Green and Y. Zhang, *Flame Patterns of Acoustic Wave and Flame Interaction in a Cylindrical Tube,* J. Visualization, 4 (2001) 179-184.

[38] S. Farhat, D. Kleiner and Y. Zhang, *Jet diffusion flame characteristics in a loudspeaker-induced standing wave,* Combust. Flame, 142 (2005) 317-323.

[39] S. A. Farhat, W. B. Ng and Y. Zhang, *Chemiluminescent emission measurement of a diffusion flame jet in a loudspeaker induced standing wave,* Fuel, 84 (2005) 1760-1767.

[40] A. O. Ehi-Uujamhan, *Chemiluminescence Studies and Flame Dynamics of Simulated Biogas*, in *School of Mechanical, Aerospace and Civil Engineering*. 2008, University of Manchester: Manchester.

[41] Y.-C. Chao and J. Ming-Shan, *Behavior of the lifted jet flame under acoustic excitation,* Symp. (Int.) Combust., 24 (1992) 333-340.

[42] F. Baillot and D. Demare, *Physical mechanisms of a lifted nonpremixed flame stabilized in an acoustic field,* Combust. Sci. Technol., 174 (2002) 73-98.

[43] D. Demare and F. Baillot, *Acoustic enhancement of combustion in lifted nonpremixed jet flames,* Combust. Flame, 139 (2004) 312-328.

[44] M. Kim, Y. Choi, J. Oh and Y. Yoon, *Flame-vortex interaction and mixing behaviors of turbulent non-premixed jet flames under acoustic forcing,* Combust. Flame, 156 (2009) 2252-2263.

[45] S. B. Dworkin, B. C. Connelly, A. M. Schaffer, B. A. V. Bennett, M. B. Long, M. D. Smooke, M. P. Puccio, B. McAndrews and J. H. Miller, *Computational and experimental study of a forced, time-dependent, methane-air coflow diffusion flame,* Proc. Combust. Inst., 31 (2007) 971-978.

[46] K. Lakshminarasimhan, M. D. Ryan, N. T. Clemens and O. A. Ezekoye, *Mixing characteristics in strongly forced non-premixed methane jet flames,* Proc. Combust. Inst., 31 (2007) 1617-1624.

[47] T. K. Kim, J. Park and H. D. Shin, *Mixing mechanism near the nozzle exit in a tone excited non-premixed jet flame,* Combust. Sci. Technol., 89 (1993) 83-100.

[48] Y. C. Chao, T. Yuan and C. S. Tseng, *Effects of flame lifting and acoustic excitation on the reduction of NOx emissions,* Combust. Sci. Technol., 113-114 (1996) 49-65.

[49] M. Saito, M. Sato and A. Nishimura, *Soot suppression by acoustic oscillated combustion,* Fuel, 77 (1998) 973-978.

[50] J. A. Lovett and S. R. Turns, *Structure of pulsed turbulent nonpremixed jet flames,* Combust. Sci. Technol., 94 (1993) 193-217.

[51] P. Chatterjee, U. Vandsburger, W. R. Saunders, V. K. Khanna and W. T. Baumann, *On the spectral characteristics of a self-excited Rijke tube combustor numerical simulation and experimental measurements,* J. Sound Vibrat., 283 (2005) 573-588.

[52] D. Durox, T. Schuller, N. Noiray and S. Candel, *Experimental analysis of nonlinear flame transfer functions for different flame geometries,* Proc. Combust. Inst., 32 (2009) 1391-1398.

[53] G. A. Richards, D. L. Straub and E. H. Robey, *Passive Control of Combustion Dynamics in Stationary Gas Turbines,* J. Propul. Power, 19 (2003) 795-810.

[54] B. F. Murat K. Aktas, *Numerical simulation of acoustic streaming generated by finite-amplitude resonant oscillations in an enclosure,* J. Acoust. Soc. Am., 116 (2004) 2822-2831.

[55] L. Menguy and J. Gilbert, *Non-linear acoustic streaming accompanying a plane stationary wave in a guide,* Acu, 86 (2000) 249-259.

[56] V. G. Hélène Bailliet, Richard Raspet, and Robert A. Hiller, *Acoustic streaming in closed thermoacoustic devices* J. Acoust. Soc. Am., 110 (2001) 1808-1821.

[57] S. J. Lighthill, *Acoustic streaming,* J. Sound Vibrat., 61 (1978) 391-418.

[58] P. P. Michael Nelkon, *Advanced level physics*, 7th, Heinemann Educational Books, London, 1995, pp. 569.

[59] G. Huelsz and F. LÃ pez-Alquicira, *Hot-wire anemometry in acoustic waves,* Exp. Fluids, 30 (2001) 283-285.

[60] M. W. Thompson and A. A. Atchley, *Simultaneous measurement of acoustic and streaming velocities in a standing wave using laser Doppler anemometry,* J. Acoust. Soc. Am., 117 (2005) 1828-1838.

[61] B. Gazengel and S. Poggi, *Measurement of acoustic particle velocities in enclosed sound field: Assessment of two Laser Doppler Velocimetry measuring systems,* ApAc, 66 (2005) 15-44.

[62] M. Campbell, J. A. Cosgrove, C. A. Greated, S. Jack and D. Rockliff, *Review of LDA and PIV applied to the measurement of sound and acoustic streaming,* Optics & Laser Technology, 32 (2000) 629-639.

[63] M. Nabavi, K. Siddiqui and J. Dargahi, *Measurement of the acoustic velocity field of nonlinear standing waves using the synchronized PIV technique,* Exp. Therm Fluid Sci., 33 (2008) 123-131.

[64] K. Siddiqui and M. Nabavi, *Measurement of the acoustic velocity characteristics in a standing-wave tube using out of phase PIV,* Flow Meas. Instrum., 19 (2008) 364-369.

[65] M. Nabavi, K. Siddiqui and J. Dargahi, *Analysis of regular and irregular acoustic streaming patterns in a rectangular enclosure,* WaMot, 46 (2009) 312-322.

[66] H. H. Bruun, *Hot-wire anemometry: principles and signal analysis*, Oxford University Press, New York, 1995.

[67] Markus Raffel, Christian E. Willert, Steve T. Wereley and J. Kompenhans, *Particle Image Velocimetry - A Practical Guide*, Second Edition, Springer Berlin Heidelberg New York, 2007.

[68] R. J. Adrian, *Twenty years of particle image velocimetry,* Exp. Fluids, 39 (2005) 159-169.

[69] P. Buchhave, *Particle image velocimetry--status and trends,* Experimental Thermal and Fluid Science, 5 (1992) 586-604.

[70] D. Dabiri, *Digital particle image thermometry/velocimetry: A review,* Experiments in Fluids, 46 (2009) 191-241.

[71] I. Grant, *Particle image velocimetry: A review,* Proceedings of the Institution of Mechanical Engineers, Part C: Journal of Mechanical Engineering Science, 211 (1997) 55-76.

[72] J. Westerweel, *Digital Particle Image velocimetry - theory and application*, Third edition, Delft University Press, 1993.

[73] F. M. White, *Fluid Mechanics*, Sixth, McGraw-Hill, New York, 2008.

[74] A. Melling, *Tracer particles and seeding for particle image velocimetry,* Meas. Sci. Technol., 8 (1997) 1406-1416.

[75] J. L. L. W. H. Snyder, *Some measurements of particle velocity autocorrelation functions in a turbulent flow,* J. Fluid Mech., 48 (1971) 41-71.

[76] M. Nabavi, M. H. Kamran Siddiqui and J. Dargahi, *Simultaneous measurement of acoustic and streaming velocities using synchronized PIV technique,* Meas. Sci. Technol., 18 (2007) 1811-1817.

[77] A. Melling. *Seeding gas flows for laser anemometry,* in *AGARD Conference Proceedings*, 1986.

[78] R. Mei, *Velocity fidelity of flow tracer particles,* Experiments in Fluids, 22 (1996) 1-13.

[79] C. J. Kahler, B. Sammler and J. Kompenhans, *Generation and Control of Particle size distributions for Optical Velocity Measurement Techniques in Fluid Mechanics,* DLR-Mitteilung, (2001) 1193-1200.

[80] L. Feng Chen and H. Koichi, *Chapter 3 Particle Image Velocimetry Techniques and its Applications in Multiphase Systems*, in *Advances in Chemical Engineering*, Academic Press 2009. p. 87-147.

[81] C. E. Willert and M. Gharib, *Digital particle image velocimetry,* Exp. Fluids, 10 (1991) 181-193.

[82] R. Theunissen, F. Scarano and M. L. Riethmuller, *An adaptive sampling and windowing interrogation method in PIV,* Meas. Sci. Technol., 18 (2007) 275-287.

[83] J. Nogueira, A. Lecuona and P. A. RodrÃguez, *Local field correction PIV, implemented by means of simple algorithms, and multigrid versions,* Meas. Sci. Technol., 12 (2001) 1911-1921.

[84] J. Nogueira, A. Lecuona and P. A. Rodriguez, *Local field correction PIV: On the increase of accuracy of digital PIV systems,* Exp. Fluids, 27 (1999) 107-116.

[85] K. A. Watson, K. M. Lyons, J. M. Donbar and C. D. Carter, *Scalar and velocity field measurements in a lifted CH4-air diffusion flame,* Combust. Flame, 117 (1999) 257-271.

[86] T. Otsuka and P. Wolanski, *Particle image velocimetry (PIV) analysis of flame structure,* Journal of Loss Prevention in the Process Industries, 14 (2001) 503-507.

[87] N. Yilmaz, R. E. Lucero, A. B. Donaldson and W. Gill, *Flow characterization of diffusion flame oscillations using particle image velocimetry,* Exp. Fluids, 46 (2009) 737-746.

[88] N. Pasquier, B. Lecordier, M. Trinité and A. Cessou, *An experimental investigation of flame propagation through a turbulent stratified mixture,* Proc. Combust. Inst., 31 (2007) 1567-1574.

[89] Y. L. Shoshin and L. P. H. d. Goey, *Experimental study of lean flammability limits of methane/hydrogen/air mixtures in tubes of different diameters,* Exp. Therm Fluid Sci., (2010).

[90] J. Rienitz, *Schlieren experiment 300 years ago,* Natur, 254 (1975) 293-295.

[91] G. S. Settles, *Schlieren and shadowgraph techniques: visualizing phenomena in transparent media*, 2nd printing, Springer, New York, 2006.

[92] T. P. Davies, *Schlieren photography--short bibliography and review,* Optics & Laser Technology, 13 (1981) 37-42.

[93] Q. Wang, *Advanced Optical and 3D Reconstruction Diagnostics for Combustion and Fluids Research*, in *MecEn*. 2012, University of Sheffield: Sheffield.

[94] Available from: http://en.wikipedia.org/wiki/Photomultiplier_tube, 2012.

[95] A. G. Gaydon, *The spectroscopy of flames*, 2nd, Chapman and Hall Ltd., 1974.

[96] H. Guo, *Flame and Acoustic Waves Interactions and Flame Control*, in *School of Mechanical, Aerospace and Civil Engineering*. 2010, University of Manchester: Manchester.

[97] P. L. Rijke, *Notice of a new method of causing a vibration of the air contained in a tube open at both ends* Phil. Mag, 17 (1859) 419-422

[98] K. T. Christensen, *The influence of peak-locking errors on turbulence statistics computed from PIV ensembles,* Exp. Fluids, 36 (2004) 484-497.

[99] D. Marx, X. Mao and A. J. Jaworski, *Acoustic coupling between the loudspeaker and the resonator in a standing-wave thermoacoustic device,* ApAc, 67 (2006) 402-419.

[100] G. W. Swift, *Thermoacoustic engines* J. Acoust. Soc. Am., 84 (1988) 1145-1180

[101] L. E. Kinsler, A. R. Frey, A. B. Coppens and J. V. Sanders, *Fundamentals of acoustics* Fourth edition, John Wiley & Sons, 2000.

[102] H. Bailliet, P. Lotton, M. Bruneau and V. Gusev, *Coupling between electrodynamic loudspeakers and thermoacoustic cavities,* Acu, 86 (2000) 363-373.

[103] A. K. Gupta, L. Lourenco, M. Linck and S. Archer, *New Particle-Image-Velocimetry Method to Measure Flowfields in Luminous Spray Flames,* J. Propul. Power, 20 (2004) 369-372.

[104] Y. Shoshin, G. Gorecki, J. Jarosinski and T. Fodemski, *Experimental study of limit lean methane/air flame in a standard flammability tube using particle image velocimetry method,* Combust. Flame, 157 (2010) 884-892.

[105] R. W. Schefer and P. J. Goix, *Mechanism of flame stabilization in turbulent, lifted-jet flames,* Combust. Flame, 112 (1998) 559-574.

[106] J. Ji and J. P. Gore, *Flow structure in lean premixed swirling combustion,* Proc. Combust. Inst., 29 (2002) 861-867.

[107] L. Muniz and M. G. Mungal, *Instantaneous flame-stabilization velocities in lifted-jet diffusion flames,* Combust. Flame, 111 (1997) 16-31.

[108] X. C. Zhou and J. P. Gore, *Experimental estimation of thermal expansion and vorticity distribution in a buoyant diffusion flame,* Symp. (Int.) Combust., 27 (1998) 2767-2773.

[109] X. Mao and A. J. Jaworski, *Application of particle image velocimetry measurement techniques to study turbulence characteristics of oscillatory flows around parallel-plate structures in thermoacoustic devices,* Meas. Sci. Technol., 21 (2010).

[110] M. Hino, M. Kashiwayanagi, A. Nakayama and T. Hara, *Experiments on the turbulence statistics and the structure of a reciprocating oscillatory flow,* J. Fluid Mech., 131 (1983) 363-399.

[111] S. Kartheekeyan and S. R. Chakravarthy, *An experimental investigation of an acoustically excited laminar premixed flame,* Combust. Flame, 146 (2006) 513-529.

[112] K. T. Kim, J. G. Lee, B. D. Quay and D. A. Santavicca, *Response of partially premixed flames to acoustic velocity and equivalence ratio perturbations,* Combust. Flame, 157 1731-1744.

[113] A. Bourehla and F. Baillot, *Appearance and Stability of a Laminar Conical Premixed Flame Subjected to an Acoustic Perturbation,* Combust. Flame, 114 (1998) 303-318.

[114] T. C. Williams, C. R. Shaddix, R. W. Schefer and P. Desgroux, *The response of buoyant laminar diffusion flames to low-frequency forcing,* Combust. Flame, 151 (2007) 676-684.

[115] H. W. Huang, Q. Wang, H. J. Tang, M. Zhu and Y. Zhang, *Characterisation of external acoustic excitation on diffusion flames using digital colour image processing,* Fuel, (2011).

[116] J. M. T. Thompson and H. B. Stewart, *Nonlinear Dynamics and Chaos*, Second Edition, John Wiley & Sons, Ltd., Chichester, England, 2002, p. 191.

[117] P. R. Fenstermacher, H. L. Swinney and J. P. Gollub, *Dynamical instabilities and the transition to chaotic taylor vortex flow,* J. Fluid Mech., 94 (1979) 103-128.

Appendix: MATLAB Code for the Analysis of the Acoustical System

```
clear all;
close all;
precision = 'double';

% General constants

p0 = 101325;                % (pa) ambient pressure
T0 = 273.15 + 20;           % (K) ambient temperature
R = 287.096;                % (J/kg.K) gas constant
cp = 1004.836;              % (J/kg.K) isobaric specific heat
gamma = 1.4;                % specific heat ratio
rho0 = p0/(R*T0);           % (kg/m^3) density of air at P0 & T0
c0 = sqrt(gamma*R*T0);      % (m/s) sound speed
nu = 1.85*10^(-5)/rho0;     % (m^2/s) kinematic viscosity of air
kappa = 0.026/(rho0*cp);    % (m^2/s) thermal diffusity of air

% Characteristics of the loudspeaker

S = 0.0218;                 % (m^2) Cross-sectional area of loudspeaker
Re = 4;                     % (Ω) Electrical resistance of the coil
Le = 0;                     % Electrical inductance of the coil
Bl = 10.61;                 % (T.m)Bl product
m = 0.0367;                 % (kg) Moving mass
s = 5660;                   % (N/m) Suspension stiffness
h = 6;                      % (Ns/m) Suspension damping

% Characteristics of the resonator

y0 = 0;                     % speaker membrane position
y1 = 0.3;                   % large end of the pyramidal structure
ya = 0.7;                   % small end of the pyramidal structure
y2 = 1.1;                   % ordinate of the apex of the pyramidal structure
rA = 0.057;                 % half wide of part A
rB = 0.1016;                % half wide of part B
SBy0 = 0.0438;              % cross-sectional area of part B
SBy1 = 0.013;               % cross-sectional area of part A
SA = SBy1;                  % cross-sectional area of part A
```

```
% Parameters

f = 550;                    % frequency
omega = 2*pi.*f;
Ve = 5;                     % Input voltage

% Caculations

deltanu = sqrt(2*nu./omega);              % viscous penetration depth
deltakappa = sqrt(2*kappa./omega);     % thermal penetration depth

kB = omega./c0;

fnuA = (1-i).*deltanu/rA;
fkappaA = (1-i).*deltakappa/rA;
kA = omega./c0.*sqrt((1+(gamma-1).*fkappaA)./(1-fnuA));

RA = -exp(-2*i.*kA*y2);

y1p = y1-ya;
ZSB1 = rho0*c0/SBy1;
ZSA = omega.*rho0./(SA.*kA.*(1-fnuA));
Z1 = ZSA.*(exp(-i.*kA*y1)+RA.*exp(i.*kA*y1));
Z2 = Z1./(exp(-i.*kA*y1)-RA.*exp(i.*kA*y1));
RB = (Z1.*(1-i./(kB*y1p))-ZSB1);
RB = RB./(Z1.*(1+i./(kB*y1p))+ZSB1).*exp(-2*i.*kB*y1p);
y0p = y0-ya;
ZSB0 = rho0*c0/SBy0;

Zac = ZSB1.*(exp(-i.*kB*y0)+RB.*exp(i.*kB*y0));
Zac = Zac./(exp(-i.*kB*y0)-RB.*exp(i.*kB*y0));
Ze = Re+i.*omega*Le;
Zmec = h+i.*(m.*omega-s./omega);
U0 = S*Bl*Ve./(Ze.*(Zmec+S*S.*Zac)+Bl*Bl);

B = ZSB0*y0p*U0;
Be = (1-(i./(kB*y0p))).*exp(-i.*kB*y0p);
Bf = RB.*(1+(i./(kB*y0p))).*exp(i.*kB*y0p);
B = B./(Be-Bf);
A = B/y1p.*(exp(-i*kB*y1p)+RB.*exp(i.*kB*y1p));
A = A./(exp(-i.*kA*y1)+RA.*exp(i.*kA*y1));

y = 0:0.01:y2;
[ysz1,ysz] = size(y); clear ysz1
p(1:ysz)=0; u(1:ysz)=0;
```

```
for ii = 1:ysz
   if  (y(ii)>= y1)
      yi = y(ii);
      p(ii)=A*(exp(-i*kA*yi)+RA*exp(i*kA*yi));
      u(ii)=kA*(1-fnuA)/omega/rho0*A*(exp(-i*kA*yi)-RA*exp(i*kA*yi));
   elseif (y(ii)>=y0) && (y(ii)<y1)
       yi = y(ii)-ya;
       p(ii)=B/yi*(exp(-i*kB*yi)+RB*exp(i*kB*yi));
       u(ii)=B/(yi*rho0*c0);
       u(ii)=u(ii)*((1-i/kB/yi)*exp(-i*kB*yi)-(1+i/kB/yi)*RB*exp(i*kB*yi));
% Part C
   end
end

%=====================================================================
yp=0:0.001:0.04;
[ypsz1,ypsz]=size(yp); clear ypsz1;
yp1(1:ypsz)=y1; yp2(1:ypsz)=y2;

fig1 = figure(1);
set(fig1, 'units','centimeters');
set(fig1, 'position', [1. 3. 17. 12.]);
set(gca, 'fontsize', 16);
hold on;
plot(yp1,yp,'k:');plot(yp2,yp,'k:');
plot(y, abs(u)/c0, 'k');
plot(y, abs(p)/p0, 'k');
xlabel('Z [m]');
ylabel('abs(u)/c0 and abs(p)/p0');
axis([0 1.1 0 0.001])

%=====================================================================
clear all
```